SCHOOL OF COMPUTER SCIENCE

Whisker-Inspired Sensors for Unstructured Environments

Teresa A. Kent

CMU-RI-TR-24-80

Submitted as part of the requirements for the thesis proposal for the degree of

Doctor of Philosophy

The Robotics Institute

Carnegie Mellon University

Pittsburgh, PA, USA

Thesis Committee:

Sarah Bergbreiter (advisor)

Mitra Hartmann

Zeynep Temel

Victoria Webster Wood

01/09/2025

Abstract

Robots lack the perception abilities of animals, which is one reason they can not achieve complex control in outdoor unstructured environments with the same ease as animals. This thesis focuses on increasing the perception ability of the bio-inspired whisker sensor, an underdeveloped sensor for robotic perception in contact mapping on terrestrial robots and airflow during a drone flight. Prior work into engineered whisker-inspired sensors demonstrates that the whisker's high compliance, sensing in low visibility, and 3D perception abilities are assets for robotic sensing. Here, we enhance the benefits of prior whisker-inspired sensors by developing sensors and algorithms that are robust to three confounding signals we consider as likely to occur in unstructured environments: 1. objects with compliance 2. simultaneous signals (e.g., wind when trying to sense contact) 3. wind during flight. Through our development of the sensors and algorithms, we found key insights that could be applied to future engineered whisker sensors.

The most popular contact mapping algorithm assumes contact does not occur on compliant surfaces, surfaces that are prevalent in real-world environments. We demonstrate that a sensor that compares the output of this contact point estimation algorithm with a second contact point estimation algorithm can quantify the divergence between the two estimates. This divergence metric indicates the likelihood that the no-compliance assumption has failed. The metric provides insights into the whisker sensor's environment and allows a robot platform to rely on precision estimates until there are indications of algorithm failure (Chapter 2).

In a sensor called WhiskSight, we demonstrated how global stimuli (airflow, body

motion) affect an array of whiskers uniformly while local stimuli (contact) affect each whisker in an array differently. This distinction allowed an algorithm to distinguish the source of whisker response between contact, airflow, and body motion occurring simultaneously, eliminating prior requirements for the whisker sensor to know the stimuli it measured (Chapter 3).

The WhiskSight sensor provided the key insight into our work on flow sensors for quadrotors: comparing signals from an array of whisker sensors could be more informative than averaging single sensors. In the two flow arrays we created we used different methods to create whiskers with asymmetric sensitivity to flow based on flow heading. When we compared the signals of all the whiskers in the array, the signals illuminated causal flow measured on a quadrotor. In Chapter 4, the whisker sensors' cross section was asymmetric, and varying the orientation of the whisker led to different response strengths, improving flow heading prediction accuracy by 19%.

In Chapter 5 and 6, the asymmetry was generated using a densely packed whisker array. This array made it possible to distinguish two simultaneous flow headings, which is important as quadrotors experience both motion-inducedd drag and wind. With a 2 x 2 array of densley packed whiskers we could predict the heading of a second flow source with a Root Mean Square Error of 5.3°.

Acknowledgments

I would first like to thank my advisor, Prof. Sarah Bergbreiter, for making me a better researcher and communicator through her mentorship, support, and guidance. Thank you for all your help!

I would like to express my gratitude to my thesis committee, Prof. Mitra Hartmann, Prof. Zeyenp Temel, and Prof. Victoria Webster-Wood. Thank you for your interest, enthusiasm and guidance on my work.

I would have not reached this milestone without the willingness of my collaborators and coauthors to share their insights and knowledge. I especially want to thank the SeNSE Lab and all the members of the Neural-Inspired Sparse Sensing and Control for Agile Flight Multi University Research Initiative.

I would like to thank my current and former lab mates at the Microrobotics Lab for all of their helpful discussion and feedback, and for being amazing people who helped me enjoy coming to work each day.

My love of research was sparked by the UMD Gemstone Honors Program, where I worked with Dr. Bao Yang on Team Piezo. The mentorship of Dr. Eric Marvicka, Dr. Carmel Majidi, and the members of the Soft Machines Lab furthered that love.

I am incredibly grateful for my friends: Abhi, Roshni and Kiyn you have made Pittsburgh my home through your love and adventures; Robin, Sofia, Nathaniel, Ana-Alicia, Belton and Adam your support has meant everything.

I am sincerely grateful to my parents, who encouraged my crazy experiments from a young age. Their constant support, advice, and encouragement allowed me to reach this milestone.

Lastly, words cannot sufficiently express my gratitude to my sister, who has gone above and beyond to support my PhD, enduring endless phone calls, allowing me to talk about my research at length, and always supporting me. I love you dearly.

Funding

This work was supported by NSF grant BCS-1921251 and MURI award number FA9550-19-1-0386

Contents

List of Figures

List of Tables

Chapter 1

Introduction

1.1 Motivation

Arrays of hair-based sensors (i.e., whiskers and specialized insect hairs) are essential for biological perception [1]. The fascinating thing about these hair sensors is the nuanced understanding of the environment that the hair bending gives the creature despite there being no mechanoreceptors anywhere but at the base of the hair. Contact whiskers provide essential signals for navigation, foraging, and hunting in low light; water flow whiskers allow seals to distinguish prey movement from general water flow in low light [2]; and specialized insect hairs generate signals in response to wind, knowledge essential for flight stability and flight agility [3] (Section 1.2). Engineered hair-based sensors (termed whiskers in this work) can also facilitate tasks that robots are still struggling to achieve. However, the development of bio-inspired whisker sensors is challenging for the same reason they are biologically inspiring: sensing complex environmental signals by only using signals at the base of the whisker is difficult.

Despite the difficulty of designing biologically inspired whisker sensors, many examples of engineered whisker sensors have outstanding abilities (Section 1.3). Whiskers for contact and airflow have shown surface reconstruction and wind flow measurement during hovering, respectively. However, engineered whisker sensors still fall short of the full benefit of whisker sensing, which is precise sensing in un-

structured environments with noisy signals and various stimuli. This noise does not cause biological creatures the same interpretation issues that it would cause engineered sensors; for example, rats can sense airflow and contact with whiskers, which implies they can distinguish between the two stimuli sources. In this thesis, I consider the gaps between biological and engineered whisker sensing abilities and develop sensors and signal interpretation algorithms to fill the gaps. The mechanical differences between biological and engineered sensors provided insights that inspired the novel sensor development, ultimately increasing the complexity of the signals engineered whisker sensors can interpret correctly (Section 1.4).

1.2 Biological Hair Sensing

1.2.1 Whisker Sensors

The whisker (vibrissa) is a special type of mammalia hair categorized by being thicker, stiffer, embedded deeper in the hair follicle, and having a follicle with more nerve endings than the average hair [1]. This combination of features increases the whisker follicle's sensitivity to forces caused by whisker bending during contact/ flow. This increased sensitivity is important because whiskers, like all other hairs, have no tactile receptors along their length. Instead, the mechanoreceptors are in the whisker's follicle at its base; it is believed the rat estimates the whisker's bend response to stimuli from its mechanoreceptors' response [4].

Contact Whiskers:

Researchers have shown that a receptor response unique to each bend would imply that mammals know the precise contact location along their whisker [4]. A collection of these 3D contact locations allows mammals to create advanced mappings of their surroundings. The number and motion of whiskers also improve the speed of mapping. An array of between 9 [5] and over 275 whiskers [6], of varying length and stiffness, are on each side of the mammal's face. The heterogeneity of the whiskers

in the array is hypothesized to be important. The motion of the whiskers, called sweeping, involves the whiskers traveling closer and farther from the nose in search of contact.

Flow Whiskers:

Vibirssae also exist as flow sensors. The most effective flow-sensing whiskers occur in pinniped mammals, whose whiskers are longer and have ten times more mechanoreceptors at their base than in terrestrial mammals [7]. This combination makes their whiskers even more sensitive, allowing them to detect small changes in aquatic flow caused by nearby prey swimming [2].

1.2.2 Hair Flow Sensors

Bat Hairs

Bats also have a set of ultra-sensitive hairs to detect flow. The morphology of these hairs is distinct from whiskers, and therefore, they are not defined as whiskers. Even still, they are similar to the whisker in their improved sensing transmission over body hair [3]. These sensors are predicted to be critical to advanced maneuvers and flight stability. Researchers substantiated this in a study comparing the flight of a bat with and without these ultra-sensitive hairs (University of Maryland Institutional Animal Care and Use Committee approved). In this study, the bats flew faster and performed wider bank turns without the sensitive hairs on their wings. The authors hypothesized that the hairs were flow sensors and the bat was underestimating its speed without the hairs. They also predicted the hairs provided information about stability, which is why the bats made larger banking turns without the hairs.

1.2.3 Multi Stimuli Sensing

The descriptions of contact and flow sensing represent the primary application of the hairs for different mammals but not the only ability. Rats can sense airflow even in sight-deprived environments [8], and pinnipeds (walruses, seals) will use their

whiskers for contact during feeding [9]. By contrast, some species' whiskers have evolved to dampen certain stimuli. For example harbor seals have wavy whiskers which dampen the stimuli caused by vortex induced vibration caused by the seal's swimming in order to focus on external flow [10, 11]. Despite all we know, there are many open questions regarding the full scope of whiskers' abilities.

1.3 Robotic Whiskers

Like their biological counterparts, robotic whisker sensors must have all sensing at or below their base. This makes the engineered sensor less intuitive to develop but has advantages for robots as there is less likelihood of damaging electronics or the environment. Robotic whiskers have been shown in surface mapping, airflow, texture identification [12, 13] and wake following [14, 15] but this summary will focus on robotic whiskers for contact mapping and airflow as this is related to the work in this thesis.

1.3.1 Contact Whiskers

Surface mapping performed by robots can benefit from having whiskers because the strengths of whisker sensing are also the weaknesses of standard robotic surface mapping techniques. Whiskers work in all lighting and are best at close range, opposite vision abilities. Whiskers also bend during contact, preventing forceful contact, which other tactile exploration methods risk, improving safety for both the robot and the environment. Finally, since there are no electronics along the length, the body of the whisker can be made with materials like PLA, making it inexpensive to create an array of whiskers.

Initial tactile whisker sensors demonstrated mapping through binary contact/ no contact signals [16]. However, identifying the 3D coordinates of contact along a whisker increased the specificity and speed of environmental mapping [17]. For this advantage, researchers have developed at least nine different algorithms and

even more sensors to identify the radial contact point on a whisker [18, 19]. If the contact point is accurate to 10% of the whisker length, the algorithm/ sensor is considered successful. Each algorithm requires different sensing at the base (e.g., timing information about the contact [20–23], whisker strain [19, 24, 25], whisker forces [26, 27], whisker moments [28–31]) and has different limiting conditions. The most common constraint (seven out of nine algorithms) is the whisker bend at contact must be small, typically less than 10° - 14°. Another common constraint is that the object the whisker is contacting should not be displaced due to contact (six out of the nine). The applications of these methods have been numerous; sensors have demonstrated classification abilities with only a few contacts [30], and other sensors have demonstrated advanced shape reconstruction through repeated contacts [20, 25, 29, 31, 32]. Often, these applications employ arrays of whiskers to improve the speed and detail of mappings even further.

1.3.2 Airflow Whiskers

Engineered airflow-sensing whiskers deflect under the drag force. The cause of the airflow can be relative, such as when a whisker is on a moving drone, or global, such as actual wind. While other sensors on a drone can estimate drone velocity and wind, dedicated flow sensors have a much smaller list of stimuli that will generate a flow signal than more general sensors like IMUs. Whisker sensors are preferred over pitot tubes for their ability to quantify the airflow in multiple directions.

There have been two major types of airflow sensors considered for UAVs. 1. Micro hairs for flow sensing: Research into arrays of hair flow sensors manufactured using micro-electromechanical manufacturing techniques has been ongoing for many years [33, 34]. Most of the work to characterize these arrays has been performed on a benchtop and in simulation. The micro hairs are more bio-mimetic, but because of the complexity of adding electronics at that scale, they are often 1D sensors. For that reason, most papers developing such sensors gear their applications towards the leading edge of a fixed-wing aircraft where direction of flow in one direction will

indicate flow attachment or flow separateion/stall.

2. Macro Scale Whiskers: Within the last five years, larger flow sensors have demonstrated the promise of whisker sensors on a drone to detect the magnitude and direction of flow on a drone. For example, researchers demonstrated how such a flow sensor could recreate the drone's flight path using sensed velocity information [35]. In a different application, two research labs have published papers on adding flow information to a drone's control algorithm; one to identify the source of flow [36], the second to maintain hover stability [37]. No published sensor has shown the ability to measure both sources of flow simultaneously.

1.4 Thesis Contribution

In this thesis, I explore methods to increase the perception ability of the bio-inspired whisker sensor for robotic perception in contact mapping and airflow sensing. I place a particular emphasis on maintaining engineered whisker sensors' perception abilities in environments that have noisy and varied stimuli that could affect the whiskers. Throughout the work, I consider contact whiskers (Chapter 2), multi-stimuli whiskers (Chapter 3), and airflow whiskers (Chapters 4, 5 and 6)

1.4.1 Contact Whiskers

Identifying the 3D contact location on a whisker is important for efficient scene mappings. In Chapter 2, I demonstrate the advantage of estimating this contact location using two algorithms instead of one. The leading algorithm for contact localization assumes that a contact surface is rigid and the whisker never slips. Huet et al. [26] proposed an algorithm that does not require those assumptions, but applications of the algorithm are often less accurate as the algorithm requires highly precise signals for contact localization (Figure 1.1). To overcome these flaws, I designed a novel sensor capable of collecting the necessary inputs for both algorithms. Additionally, I put forth a metric to indicate when the assumptions of the first algorithm have

failed. The combined sensor and metric allow our sensor to perform precise and accurate mappings without assumptions about rigidity or slip.

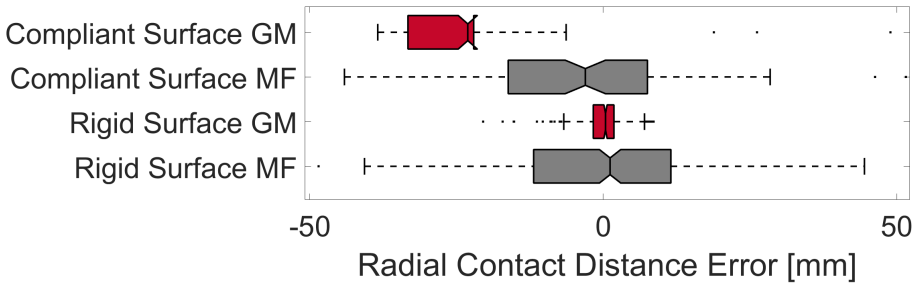

Figure 1.1: Radial contact distance estimation estimates the location along the whisker length where contact has occurred. Two algorithms (GM and MF) are compared on both compliant and rigid surfaces. The GM algorithm is precise but fails on compliant surfaces while the GM algorithm is less precise but more accurate on compliant surfaces. For more information, see chapter 2.

1.4.2 Multi Stimuli Whiskers

In unstructured environments, whiskers will be exposed to multiple stimuli which cause whisker bending. In Chapter 3, I demonstrate a novel sensor and algorithm to classify three stimuli that affect the whisker: contact, airflow, and body motion (inertia). Classifying the stimuli is made possible by replacing a single whisker with an array of whiskers. Every whisker base in the array is monitored by a single camera (Figure 1.2). The single sensor (camera) minimizes computational and mechanical complexity. These benefits make it trivial to sync the signals of each whisker as they respond to the three stimuli. In this configuration, the whiskers have characteristic responses to each stimulus. In particular, the entire array responds to airflow and inertial stimuli, while contact only influences some of the whiskers' responses. Before this publication [38], whisker sensors had focused on quantifying pre-known stimuli.

1.4.3 Airflow Sensing

Whisker-inspired sensors on drones are relatively recent. While the basic sensor structure of a drag body with sensing at the base is present in engineered whisker-inspired sensors, the sensors are considerably distinct from their biological counter-

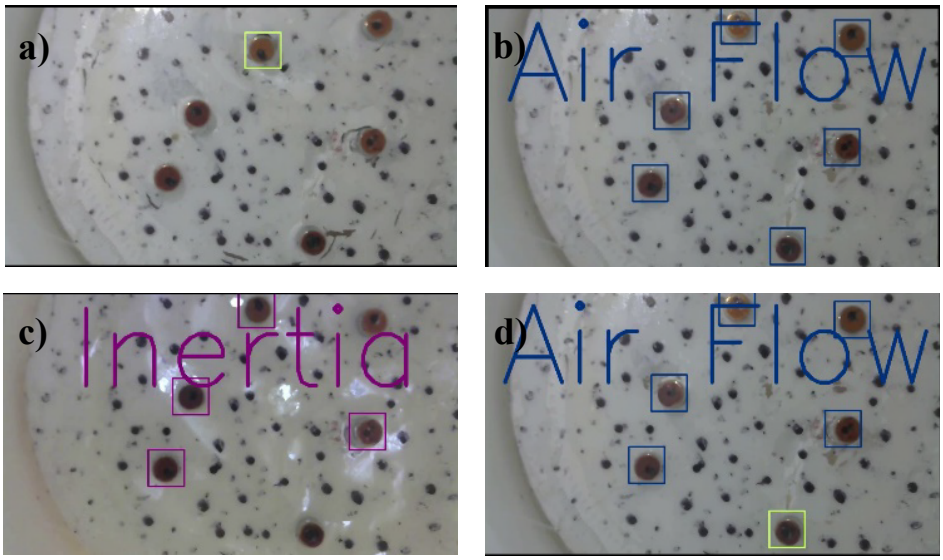

Figure 1.2: Here is the view from a camera looking up at the base of an array of six whiskers. An algorithm tracks the motion of the whisker bases in the camera frame and makes predictions about the stimuli occurring on each whisker. For more information, see chapter 3.

parts. One way engineered sensors are distinct is their symmetry. The 2D sensing symmetry is one of the things that make whisker-inspired sensors advantageous for drones. In Chapter 4, I demonstrate how small amounts of asymmetry can help improve the accuracy of flow sensing. I do this using an asymmetric whisker cross section (Fig. 1.3) so that the strength of the flow response varies based on the flow heading. This asymmetry is only helpful when there are two or more whiskers. The variations in the strength response between two whiskers at different orientations illuminate the causal flow heading. Using the strength comparison of two offset whiskers, we increased the accuracy of our flow heading prediction by 19%.

The idea of asymmetry to improve flow heading prediction has more benefits than just improving the detection of flow heading; in Chapter 5, I demonstrate that a whisker array with an asymmetric response can elucidate two simultaneous flows incident on the whisker. A flow sensor on most drones will experience at least two flow sources, the self-generated flow (drone's motion) and the environment-generated flow (wind). Defining the magnitude and velocity of the two flow sources also requires an array of whiskers. However, the array alone is insufficient because when the stimuli sources are the same (airflow), the sensed signals have no characteristic

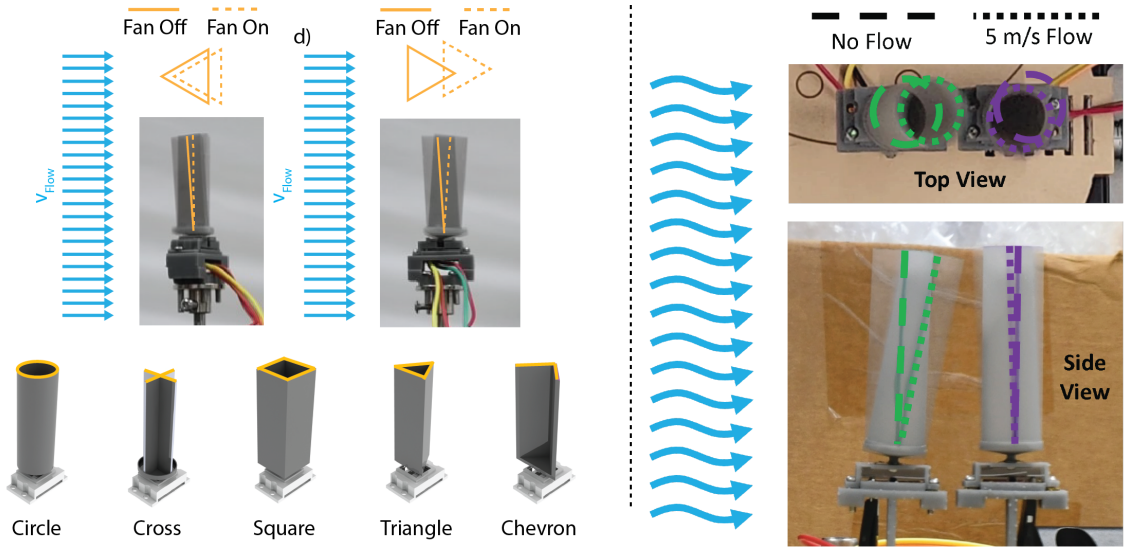

Figure 1.3: The design of a whisker sensing array can create whiskers which will have a asymmetric stregth response to flow based on flow heading. In this work we do this two ways. On the left using an ansymmetric whisker shape and on the right using a densley packed array of whiskers to block flow to downstream whiskers. When designed well, arrays of asymmetric whiskers can improve flow heading detection (Chapter 4) and allow for the distinction of two flow sources (Chapters 5 and 6).

differences. To differentiate the two signals, I use another whisker array for which the signal response depends on the flow heading. In this array, the whiskers are densely packed to prevent flow from reaching all whiskers equally (Fig. 1.3). We call this phenomenon flow shadowing. When the flow shadowing phenomenon occurs in a grid array, we can detect flow from two sources at once, the first array of whisker-inspired sensors with this ability.

Chapter 2

Gauging Whisker Contact Accuracy

Paper:

Kent, T. A., Emnett, H., Babaei, M., Hartmann, M. J., & Bergbreiter, S. (2023). Identifying Contact Distance Uncertainty in Whisker Sensing with Tapered, Flexible Whiskers IEEE International Conference on Robotics and Automation (ICRA)

My Contributions:

The sensor was designed and manufactured by me. I also ran all of the experimental tests and wrote all of the code. I wrote the initial draft of the paper and made the initial figures.

Author Contributions:

TK designed the sensor, developed the code/algorithms, ran the experiments, created the figures, and drafted the paper. HE modeled the flexible whiskers for the design optimization. MB and TK together developed the equations and code for the F_z component of the springs. HE and TK together discussed the final demonstrations for the whisker sensor. MH and SB guided the research. All authors edited the manuscripts and figures.

Abstract

Whisker-based tactile sensors have the potential to perform fast and accurate 3D mappings of the environment, complementing vision-based methods under conditions of glare, reflection, proximity, and occlusion. However, current algorithms for mapping with whiskers make assumptions about the conditions of contact, and these assumptions are not always valid and can cause significant sensing errors. Here we introduce a new whisker sensing system with a tapered, flexible whisker. The system provides inputs to two separate algorithms for estimating radial contact distance on a whisker. Using a Gradient-Moment (GM) algorithm, we correctly detect contact distance in most cases (within 4% of the whisker length). We introduce the Z-Dissimilarity score as a new metric that quantifies uncertainty in the radial contact distance estimate using both the GM algorithm and a Moment-Force (MF) algorithm that exploits the tapered whisker design. Combining the two algorithms ultimately results in contact distance estimates more robust than either algorithm alone.

2.1 Introduction

Many rodents navigate dark spaces using rhythmic protraction and retraction of their whiskers, a behavior called "whisking." The ability to navigate and develop a three-dimensional (3D) map even in darkness [16, 17, 32] has inspired engineered whisker arrays that can do the same. The most effective whisker arrays can identify the contact point along the whisker's length to create 3D scene maps [17]. In application, such arrays have mapped the fine details of a 3D face model [31], classified objects [30], defined shapes [20, 25, 29] and performed SLAM in a 3D scene [32].

In three dimensions, a contact point on a whisker is most easily defined by three components: radial contact distance (r), the direction of bending (or rotation in the case of a rigid whisker), and the magnitude of bending (Figure 2.1) [26]. Estimating radial contact distance is of particular importance to whisker mapping and at least

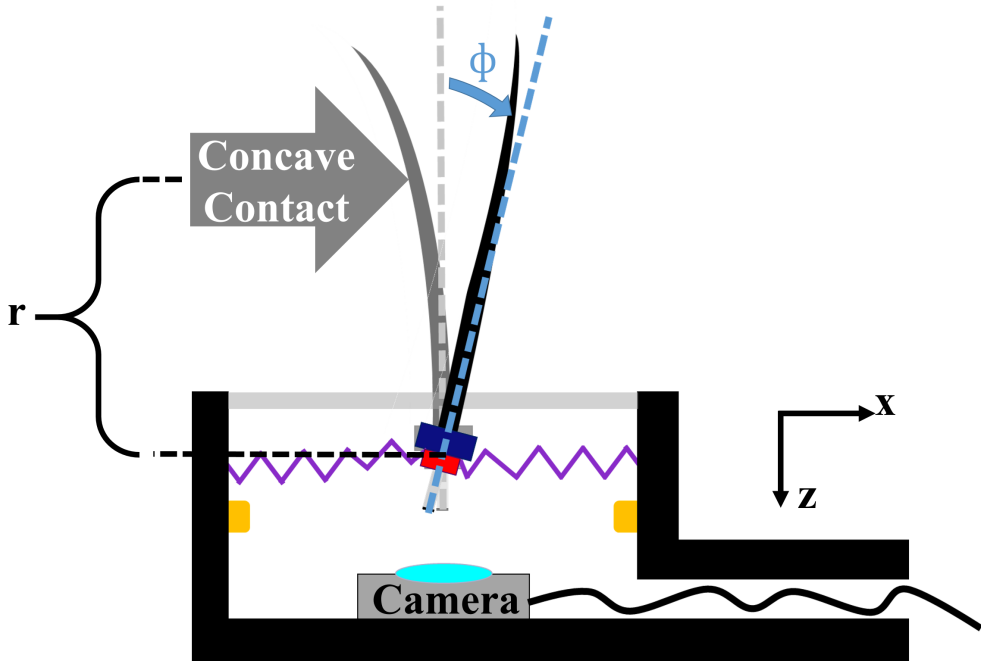

Figure 2.1: A 3D contact point on the whisker is defined by three components: **Radial Contact Distance** (r), defined in this paper as the distance in the z-direction from the point of rotation, **Direction of Bending** and **Magnitude of Bending** (rotation in the case of a rigid whisker). The algorithms discussed in this paper use three primary inputs to estimate r: 1. Δx, The distance the whisker has traveled in the x-direction since first contact occurred, 2. ϕ, angular rotation around the base of the whisker, and 3. δ_z, downward motion of the whisker base caused by bending of a flexible whisker.

nine separate algorithms have been described in the literature to localize contact to within 10% of whisker length accurately [18, 19]. However, all of these algorithms make assumptions about contact, ultimately limiting their application. For example, seven of the nine methods are only accurate under small-angle conditions, typically less than 10°-14°. Six of the nine methods obtain only a single contact point per whisk, and five of the nine require the user to know how the base of the whisker is moving (e.g., by using a motor encoder). These limitations increase the probability of undetected sensing failures. Many of the approaches also implicitly place strong constraints on allowed whisker motions, making mapping more challenging. In the present work, we demonstrate how using multiple algorithms together improves radial contact distance estimation.

The first algorithm is similar to two rotation-based algorithms: the Gradient-

Moment (GM) algorithm [28, 31] and the sweeping method [39]. These algorithms use motion (either translation, rotation, or both) of the whisker base (e.g., a linear displacement, Δx) along with a measurement of the whisker bending, ϕ, to estimate the radial contact distance, r (Figure 2.1). However, because this method depends on signal rates of change, it fails if the contact is made on a surface that deforms or moves (e.g., a leaf or a marble) as well as when the whisker translates parallel to a flat surface such as a wall [27]. In this second case, the whisker bending (ϕ) will stabilize at a fixed value in slipping contact with the wall despite the robot's continued translation (Δx), leading to a continually increasing estimate for r.

A second method for radial contact point determination does not rely on knowledge of whisker motion. This method uses only mechanical signals at the whisker base (i.e., forces and moments), and can therefore provide accurate measurements even in the failure cases described above [18, 26]. We call this approach the "Moment-Force" (MF) algorithm because it relies on these two mechanical variables [26]. Unlike the GM method, in which the whiskers can be rigid and/or cylindrical, the MF approach requires a flexible whisker with taper [26]. As the whisker bends against an object, the whisker's taper ensures that changes in the mechanical signals at the whisker base uniquely represent each 3D contact point. In previous work, some of the present authors used a whisker sensor with four strain gauges at the base to demonstrate success of the MF approach [40]. However, this previous work faced challenges with both the sensing system hardware (e.g., measurement drift and strain gauge attachment) as well as lower precision contact estimations.

In the present work, we describe a novel whisker sensor design with a flexible, tapered whisker that collects inputs for both the GM and MF algorithms. Inspired by previous camera-based whisker sensors [38, 41], we designed a whisker base that simplifies estimates of mN axial force and rotational moments as monitored by a camera. For this study, we focus only on the magnitude of the bending moment to estimate radial contact distance, and not the direction of bending. Bending direction will ultimately be required to create 3D maps. Using this sensing system, we

make two contributions to the whisker-sensor literature. First, we quantify tradeoffs between the two algorithms (GM and MF) for estimated radial contact distance accuracy and precision during rigid contact, compliant contact, and sliping contact. Second, we introduce a new metric for whisker sensing, the "Z-Dissimilarity score," which quantifies uncertainty in the radial contact distance estimate. This uncertainty estimate is based on the two separate estimates for r from the two separate algorithms. By combining the novel sensor with the two-algorithm approach, we generate accurate radial contact distance estimates with a confidence metric that can be used to identify GM-method failure cases.

2.2 Radial Contact Estimation Methods

In the first applications of whisker arrays for robotics, arrays of whiskers moved through 3D space to create mappings using contact detection whiskers [16]. In contact detection whiskers, the signal is binary, contact or non-contact, and a point on the whisker is chosen as the contact estimate [17]. This contact point estimate is normally either at the tip or the middle of the whisker. Some of the more sophisticated versions of these sensors can also detect the whisker rotation at contact [32]. Since the true contact location could occur anywhere along the whisker, the 3D mapping improves as locations of contact and non-contact accumulate. This methodology has been used to predict object shapes [41], classify objects [32], map 3D spaces [42] and avoid obstacles [43].

The applications of these methods demonstrated the benefit of whiskers for mapping spaces. Still the 3D mappings improve by knowing where on the whisker contact occurred [44]. Both intuitive and bio-realistic, this fact has inspired the development of whisker sensors capable of localizing the contact location along the whisker, the radial contact distance. The methods of radial contact estimation are categorized here into the following four groups: time-dependent estimation, strain-based estimation, gradient moment (GM) estimation, and two-moment, one-force (MF) estimation. Each of the four methods has constraints and assumptions.

In time-dependent whisker implementations, the algorithms assume that a whisker traveling at a fixed rate (either angular or linear velocity) will have a larger magnitude response to contact close to the whisker base than to contact further from the base. Implementing this algorithm requires a mechanism to sense magnitude of bend and for the robot to control the rate of the whisk. During implementation, when the system senses contact, it signals the robot to stop rotating the whisker. In the milliseconds of contact rotation between sensed contact and the stop signal, the bend magnitude signal will increase and can be used to estimate the point of contact [20–22, 30]. Similar methods measure the time it takes the whisker signal to drop back below a threshold [23, 45] during reverse rotation. In other temporal whisker sensors, the frequency of oscillation directly after contact correctly predicts the radial contact estimate [46, 47]. These time-based methods can determine one contact per whisker motion and the contact must be with a rigid surface.

On specific types of whiskers, contact between a whisker and its environment causes strain [25] proportional to the contact height. Researchers can measure the strain by placing a strain gauge at the base [19] or using a camera and fiber Bragg grating [24]. This method of radial contact distance has been published with the highest accuracy of any robotic whiskers thus far (between 1 and 2 mm on a 100 mm long whisker). The trade-off for this high accuracy is that the whisker is limited to small rotations from the contact (ideally under 0.5 °).

The most common technique for robotic whisking, estimates the radial contact from the gradient measurements of the moments at a whisker's base. This method posits that there is an inversely proportional relationship between the contact height and the amount of bend caused by a deflection of xmm or y°. The gradient moment is measured as the rate of rotation or the rate of increase in the moment at the base using hall effect sensors [28], force/torque sensors [27, 29] or pressure sensors [30]. As the whisker deflects during contact with an object, the rate of change of the moments at the base of the whisker relative to the translation/rotation of the whisker are used to estimate the radial contact distance. Whisker sensors and whisker sensing arrays

using this method have been able to map 3D scenes [28] and recreate 3D objects [31]. Combining this method with the aforementioned time-based methods, the radial contact accuracy in these robotic whiskers is up to 9.8 mm [48] and 13.6 mm [45]. One advantage of these sensors for unstructured environments is that radial contact is better estimated with larger whisker deflections. Some constraints on this method are that the whisker can not slip along the object, and the object it is making contact with must be rigid relative to the whisker. Both of these constraints are to maintain the proportionality between the robot/whisker motion, the height of contact, and the whisker bend.

The final method uses the raw values of two moments and one force (M_b, M_d, F_z) sensed at the base of a whisker to estimate the radial contact distance. In this method, simulated by [26] and realized by [40], the three variables create a unique mapping with the radial contact distance along a tapered whisker. This mapping has been realized within 6 mm of the contact location for 78% of contacts when whisker rotation was over 10°. The hypothesized benefit of this method is that radial contact is estimated without any other information besides the sensor values. The full benefits of these sensors have not been realized due to issues with the robustness of the engineered sensor caused by the strain gauge sensing modality.

2.3 Methods

2.3.1 Sensing System Manufacturing and Design

Sensing Hardware

Figure 2.2 shows a diagram of the whisker sensing system. Four 0.75 mm thick laser-cut acrylic serpentine springs suspend the whisker 25 mm above the camera (Logitech HD Webcam C310). 3D-printed tracking features are glued to the acrylic springs. A 3D-printed housing fixes the camera and springs in place. Six LEDs (Micro Litz Pure White) and a white cloth taped over the springs improve lighting consistency between frames. Two types of whiskers are used for experiments. The first is a

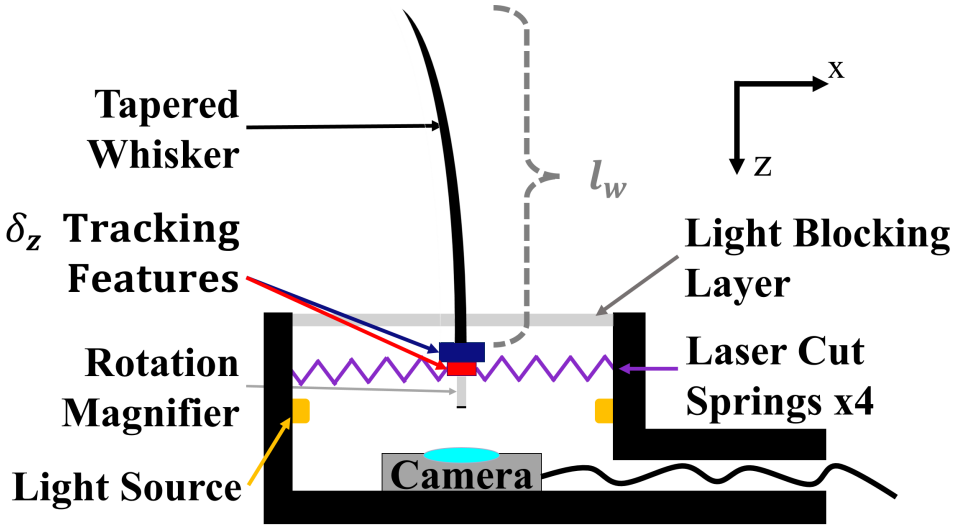

Figure 2.2: A diagram of the whisker sensor. A tapered, flexible whisker is suspended over a camera using a laser-cut spring suspension. Tracking squares and rotation magnifiers amplify motions at the whisker base in the camera image.

rigid, 1 mm-diameter carbon fiber rod. The second is a 150 mm long tapered, flexible whisker that was manufactured using the conforming fiber drawing process on a piece of filament as described in [49]. The tracking features in Figure 2.3 were chosen to simplify estimation of the whisker magnitude of rotation, ϕ, and axial deflection, δ_z, in camera images as seen in Figure 2.5. The δ_z tracking features include two components approximately equidistant from the spring's center of rotation: a C02 laser cut acrylic square-painted blue and an asiga 3D printed 100 µm cross painted red. To provide improved estimates of ϕ, the cross is printed with a 7.5 mm long rotation magnifier extending down toward the camera. The tip of the rotation magnifier is painted black. The acrylic square and the square that connects the four springs have a 2 mm diameter hole in their center where the whisker is slotted to ensure alignment. The CAD files for this sensor design can be found at [50].

Sensing Software

Motion of the whisker is captured by monitoring the tracking features with a camera, as shown in Figure 2.5. Each image frame is white balanced, and a Lucas-Kanade translation-only template-updating tracking algorithm is used to quantify movement of the δ_z tracking features [51]. To amplify red and blue contrast and convert the

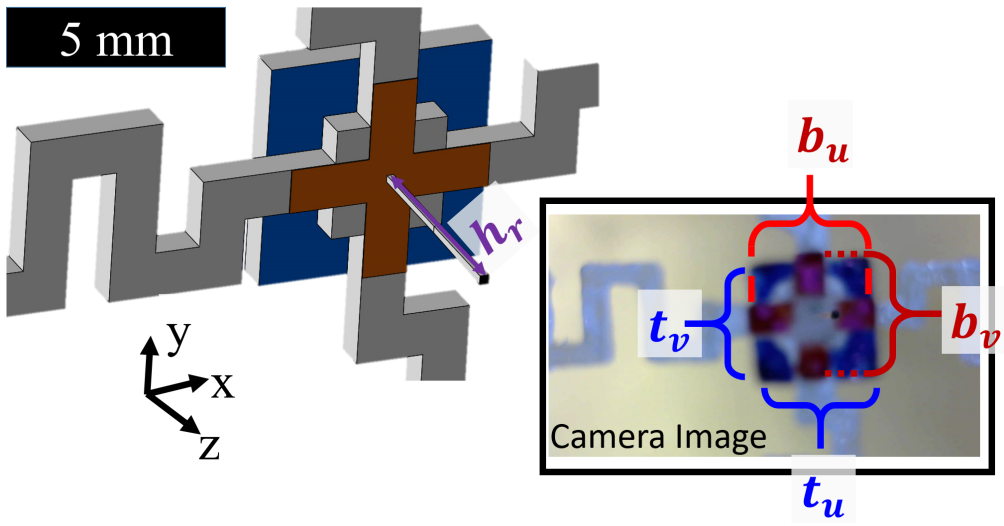

Figure 2.3: There are three features used for vision-based tracking: the top tracking square (blue), the laser cut spring (gray), and the 3D-printed (Asiga) red cross with a 7.5 mm rotation magnifying rod extending toward the camera. In the camera image the widths and thicknesses of the δ_z tracking features (b_u, b_v, t_v, t_u) are used to calculate δ_z

image into each channel, each pixel is assigned a new color (G) by comparing each pixel's red (R) and blue (B) components to the average color value of the pixel ($\overline{P}$).

$$G = \frac{(B - \overline{P}) - (R - \overline{P})}{\overline{P}} \tag{2.1}$$

The tracked points are the cross' outermost edges and the square's corners. A color-based segmentation algorithm tracks the tip of the rotation magnifier. Tracking code can be found at [50].

2.3.2 Calculating Deflections and Rotations

We solve for two signals from the camera image: the axial deflection, δ_z (Figure 2.5A) and rotation magnitude, ϕ (Figure 2.5B). As noted previously, the direction of the rotation, θ, can also be calculated from this image [38], but here θ is limited to 0° and 180° for the convex and concave cases respectively. When a positive z-deflection occurs, the system moves closer to the camera. This motion affects all tracked points equally (Figure 2.5C). It is therefore vital to remove the effect of δ_z before solving for ϕ rotation. δ_z can be calculated using the initial and current

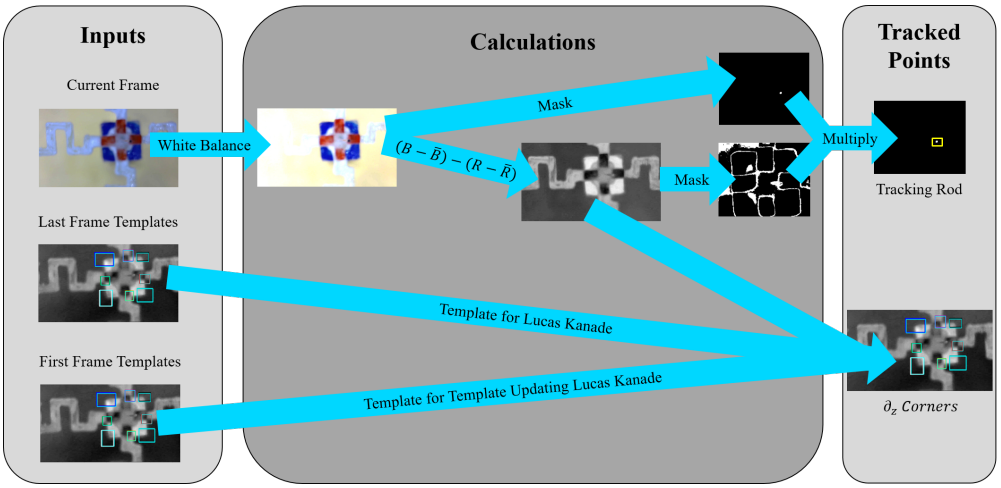

Figure 2.4: The tracking algorithm tracks 9 points. Tracking algorithms use the image from the last frame to update a point's new location. As the object moves, the tracking square can move off the desired point. To avoid drift, the frame can be updated by a template which is what the tracked point looked like in the original frame. Here we update the tracked point with the original frame every five frames. Eight of the tracked points are tracked using the Lukas Kanade tracking algorithm on white-balanced frames [51] The final tracked point, the rotation magnifier, moves too much between frames for tracking algorithms to track this point because the algorithm expects the object not to move much between frames. Instead, we use a segmentation algorithm. The segmentation algorithm identifies the largest spot that has pixel values close to zero and has similar values in the red and blue channel. The final tracked points can be seen in the right panel in the image.

values for the projected widths (b_u, b_v) and thicknesses (t_u, t_v) of the tracking features (Figure 2.3). In equation 2.2, only one of these variables is used, but any can be substituted. The subscript i represents the initial calibration frame and n represents the current frame. z_i is the initial distance between the camera and the tracked object (25 mm).

$$\delta_{zn} = z_i * (1 - \frac{b_{ui}}{b_{un}}) \tag{2.2}$$

Axial deflection also translates the rotation magnifier rod in the camera frame. Δc_u and Δc_v represent the rod tip's pixel translation in the horizontal and vertical directions.

$$\Delta c_u = \frac{(z_i - h_r) * c_{ui}}{(z_i - h_r) - \delta_z} - c_{ui} \tag{2.3}$$

$$\Delta c_v = \frac{(z_i - h_r) * c_{vi}}{(z_i - h_r) - \delta_z} - c_{vi} \tag{2.4}$$

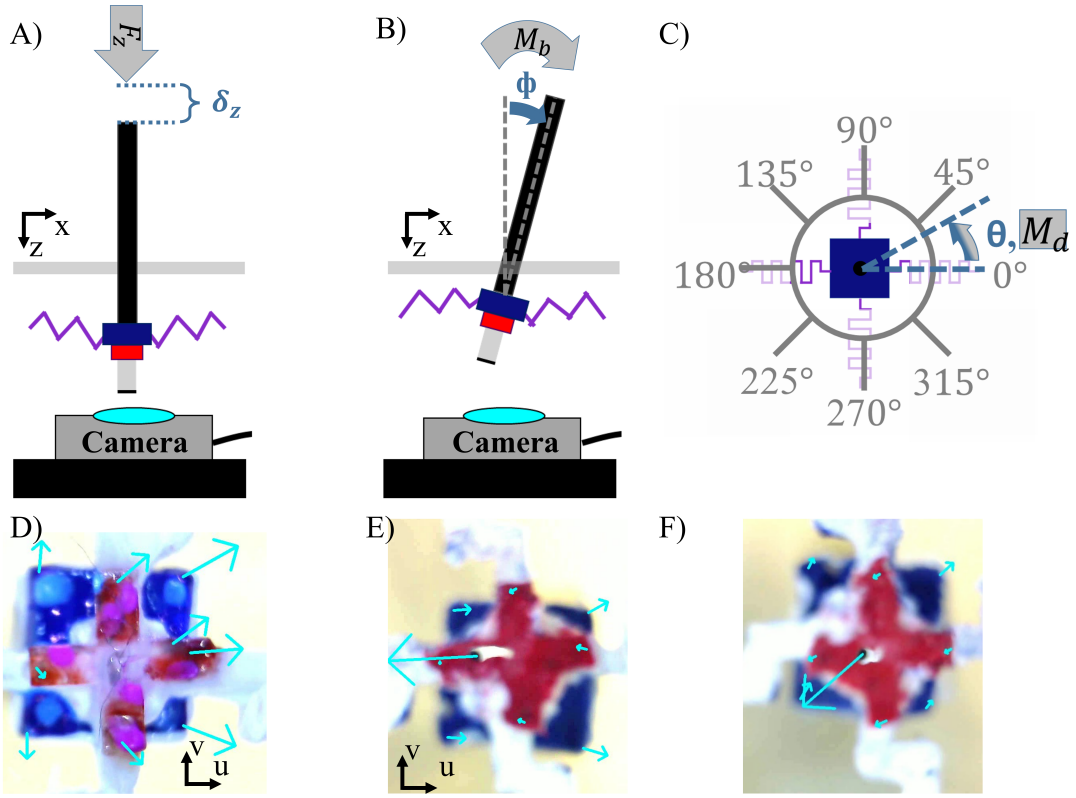

Figure 2.5: The global motions of the sensing system (A, B, C) affect the camera images (D, C, E). A downward deflection caused by an axial force, F_z, (A) brings the tracking squares and rod closer to the camera, causing the apparent areas of the square and the cross to increase (D). ϕ rotations, caused by a bending moment, M_b, (B) cause translations of the rotation magnifier (E). The direction of rotation, θ, is the same on the global coordinates and in the camera image. The cyan arrows are added during tracking and represent 10x the detected motion in pixels.

The ϕ rotation primarily affects the rotation magnifying rod (Figure 2.5D). The effects of δ_z translation (equations 2.3 and 2.4) are removed from the change in displacement of the rod in the camera frame (δ_u, δ_v) before solving for ϕ_n. θ measures the direction of ϕ. Variables used are provided in Table 2.1.

$$\mu = \frac{z_i - h_r}{u_{res}} \tan(u_{aov}) / \frac{z_i - h_r}{v_{res}} \tan(v_{aov}) \tag{2.5}$$

$$\theta_n = \arctan(\frac{\delta_{vn}}{\delta_{un}} * \mu) \tag{2.6}$$

$$\rho = \frac{1}{2}(\frac{z_i - h_r}{u_{res}} \tan(u_{aov}) + \frac{z_i - h_r}{v_{res}} \tan(v_{aov})) \tag{2.7}$$

$$\phi_n = \arctan(\rho \frac{\sqrt{\delta_{un}^2 + (\delta_{vn} * \mu)^2}}{h_r}) \tag{2.8}$$

2.3.3 Estimating moments and forces from ϕ and δ_z

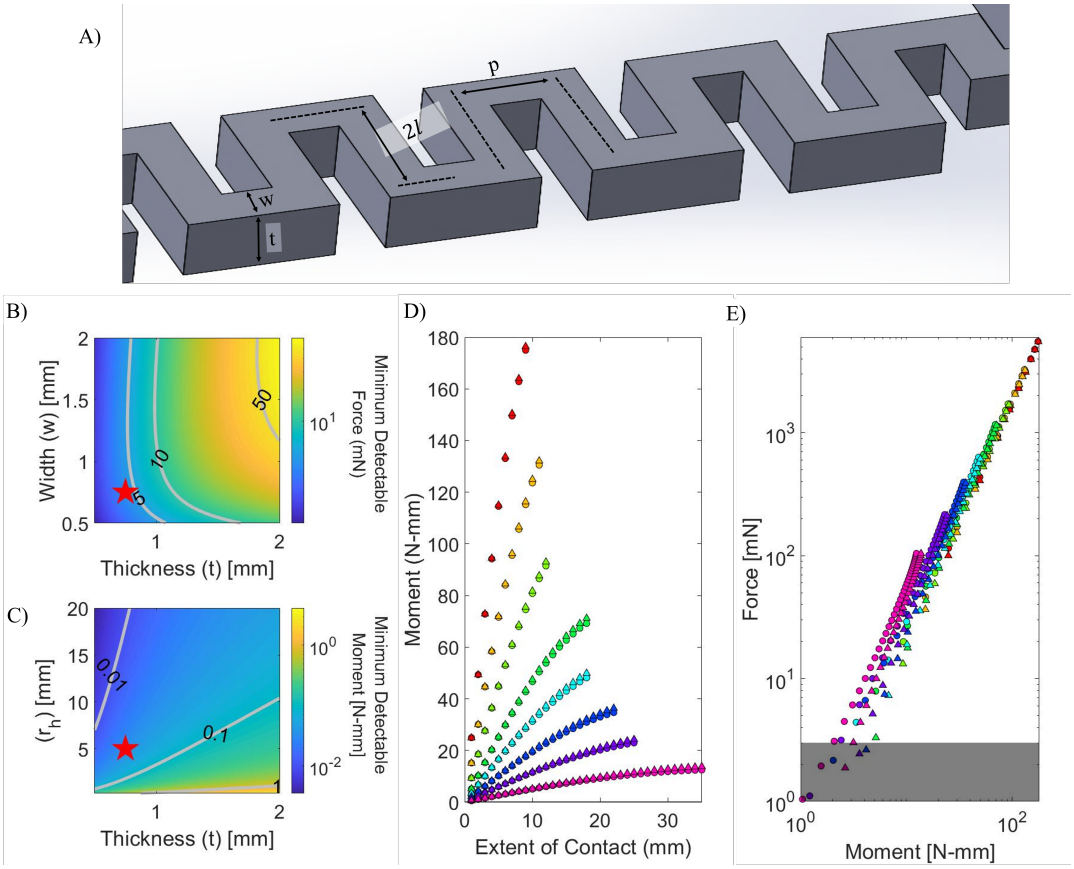

Figure 2.6: The tracking components (Fig. 2.3) are held in the center of the camera image by four serpentine springs (A). Varying the spring parameters such as the width (w), thickness (t), length (l) and pitch (p) affect the minimum detectable force (B) and moment (C) the system can detect. In B, C the red star marks the specifications chosen for the sensors used in this work. The expected forces and moments at the base of the whisker used in the experimental tests were predicted using the software from [26]. They are plotted as the input for the GM (D) and the MF (E) algorithms making up the x and y axis, and each new color on the plot represents contact at [22.5, 27.5, 33.4,42.5, 50. 60. 72.5,90] mm respectively, the same as the experimental work. The code for the modeling of the sensor can be found here [50].

Similar to previous work [52], our serpentine spring design can convert the rotations and deflections of the whisker base into forces and moments using the equations from [53]. In the MF method, the precision of estimated radial contact distance will depend strongly on the minimum detectable axial force [40] (Fig. 2.6 B). For example, for the whisker used on our sensor, the quasistatic simulations of Huet et al. [26] estimate a difference in F_z force of just 1.8 mN between contact points separated by only 1 cm after a 10° rotation (Fig. 2.6 E). Developing a sensor with such a small

detectable force is challenging. In order to make informed design decisions about the parameters in our final design (Table 2.1) we had to use not only the anticipated forces and moments from the quasistatic simulations of the whisker (Fig. 2.6 D, E), but also the springs' response to those forces and moments [53], and the equations for pixel density of the camera (equation 2.7). By combining the three sets of equations together we modeled how small changes to the spring parameters led to large changes in the minimum detectable moment and force (Fig. 2.6 B, C). Scripts to model these designs can be found at [50].

Predicting moments and forces from ϕ and δ_z is useful for design of the physical whisker sensing system, but it should be noted that the algorithms described below, calculated moments and forces were not used. As described in the results, the springs stayed in a linear regime. Therefore a linear relationship exists between bending moment and ϕ as well as between axial force and δ_z. These results were similar to those found in previous work in [40, 52].

Table 2.1: Design Parameters

Parameter	Variable	Value
spring pitch	p	2.6 mm
spring length	l	1.5 mm
spring width	w	0.75 mm
spring thickness	t	0.75 mm
number of spring turns	n	12
square magnifier width /thickness	t_w/t_t	5 mm
cross magnifier width /thickness	b_w/b_t	4 mm
rod height	h_r	7.5 mm
v/u corrector	μ	1.02
u resolution	u_{res}	1280 pixels
v resolution	v_{res}	720 pixels
u angle of view	u_{aov}	26.95 °
v angle of view	v_{aov}	16.26 °
springs offset from camera	z_i	25.0 mm

2.3.4 Algorithms to Estimate Radial Contact

The primary goal of this work is to combine the Gradient-Moment (GM) and Moment-Force (MF) algorithms so as to improve radial contact distance estimates, and to provide a metric that describes the estimates combined uncertainty.

Gradient-Moment (GM) Algorithm

The GM algorithm provides an estimate of radial contact distance (denoted as $\hat{r}_{GM}$ to distinguish it from the actual distance, r) based on the whisker rotation, ϕ, and the motion at the whisker base (in this case a linear translation, Δx).

$$\hat{r}_{GM} = \frac{C\frac{\Delta x}{\phi} l_w}{l_w + C\frac{\Delta x}{\phi}} \tag{2.9}$$

In equation 8, l_w is the length of the whisker (150 mm) and C is a constant related to the whisker stiffness. The value of C can be experimentally estimated by comparing ϕ and Δx. Given the system's small minimum detectable moment ($0.025\,\mathrm{N} - \mathrm{mm}$) we expect this method to provide relatively precise estimates of contact distance. Worth noting, in some previous work, $\dot{x}$ and $\dot{\phi}$ are used to solve for $\hat{r}$ instead [31].

Moment-Force (MF) Algorithm

This algorithm uses ϕ and δ_z, which are linearly proportional to the bending moment and the axial force, to estimate radial contact distance $\hat{r}_{MF}$. In this case, a simple analytical mapping between variables does not exist, therefore previous work has used look-up tables and classification methods to predict $\hat{r}_{MF}$ [26, 40]. In the present work, we use a k-nearest neighbor approach to estimate $\hat{r}_{MF}$.

$$d_k = \frac{\phi - \phi_k}{35} + \frac{\delta_z - \delta_{zk}}{1} \tag{2.10}$$

$$\hat{r}_{MF} = \frac{\sum_1^7 r/d_k}{\sum_1^7 1/d_k} \tag{2.11}$$

In equations 9 and 10, r represents the true label of one of the ($k = 7$) closest points to the new sensor value. Equation 2.10 calculates the distance between a point in the training set (ϕ_k, δ_{zk}) and the current sensed point (ϕ, δ_z). These values are then divided by a normalizing value of 35° and 1 mm, which represent the maximum expected values of ϕ and δ_z respectively. Given that the precision of this estimate relies on the minimum detectable force, we expect this method to yield lower precision estimates than the GM approach. However, the MF approach should remain accurate in cases where GM might fail (e.g., compliant or slipping contact).

Z-Dissimilarity Score

In statistics, Z-scores typically provide a measure of distance from the mean. We generated a Z-Dissimilarity score to provide a metric of uncertainty in the $\hat{r}_{GM}$ estimate. The score is calculated in two steps. First, we compute the (signed) difference between the values of r predicted by the two different estimation methods. This difference is then normalized by the expected standard deviation of $\hat{r}_{GM}$ at the relevant value of ϕ.

$$Z(r = \hat{r}_{GM}) = \frac{\hat{r}_{GM} - \hat{r}_{MF}}{\sigma_{r_{GM}}(\phi)} \tag{2.12}$$

A value of Z below 0.5 indicates an expected deviation while values over 1.0 indicate a probable error.

Shape Reconstruction

To demonstrate success of the present approach,we attempt to reconstruct 2D shapes using the estimated radial contact distance, $\hat{r}$, and linear translation of the whisker base, x. The estimated contact location in the x-direction is provided below. The sign depends on the direction of travel of the whisker.

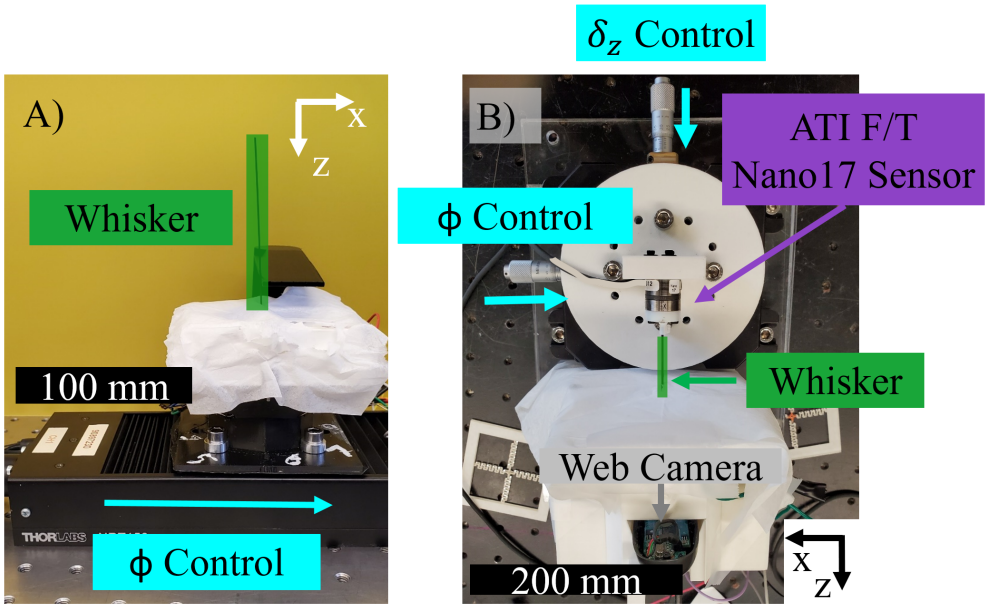

Figure 2.7: **Experimental Setup** A) A rigid (shown) and flexible whisker were translated relative to a 3D printed rigid surface by a motorized linear stage. B) Using a manual linear stage δ_z deflections could be applied with a precision of 0.05 mm, while a force-torque sensor measured the force applied to the spring system.

$$\hat{x} = x \pm \hat{r} \sin \phi \tag{2.13}$$

2.3.5 Experimental Setup

To calibrate the sensing system, a 1 mm diameter rigid whisker was glued to the spring suspension and attached to a ThorLabs NRT-150 motorized linear stage as seen in Figure 2.7A. Using the linear stage, the whisker base was moved in 1 mm increments along the x-axis to rotate the whisker between 0° to 18° to test the accuracy of ϕ calculations. Data were collected over two separate trials.

In a second test, we used a ThorLabs manual linear stage with an attached 6-axis force-torque sensor (ATI Nano17) to apply displacements to the tip of the rigid whisker (Figure 2.7B). ϕ and δ_z were calculated from camera images and were correlated with the the applied M_x and F_z as measured by the force-torque sensor. This setup allowed us to test both the accuracy of the δ_z calculations and confirm

that F_z and δ_z were linearly related.

In our third test, a tapered, flexible whisker was attached to a spring suspension system identical to that used in the first two tests. Contact was applied at varying radial contact distances using the motorized linear stage from Test 1. Contact was first applied with a rigid 3D printed surface at radial contact distances of [22.5, 27.5, 33.5, 42.5, 50, 60, 72.5, 90] mm. The linear stage controlled the position of the whisker base in the x-direction was stepped in 1 mm increments with 1 s pauses between steps. In separate tests, contact was applied using a highly-compliant object (a thin pipe cleaner) at radial contact distances of [35, 55, 90] mm. In our final test, we slid the same tapered, flexible whisker across cross-sections of a water bottle (circular) and a box (L-shaped).

All tests were run assuming a quasi-static whisker. All data were collected during pauses of the linear stages used for whisker motion or pauses in application of forces. We ensured at least one second between steps. Each data point in the results represents the median of calculated ϕ and δ_z during these pauses. Example video recordings of each test can be found in the supplemental video.

2.4 Results and Discussion

2.4.1 Accuracy of ϕ, δ_z, and F_z

A comparison between applied and predicted values of ϕ, δ_z, and F_z are presented in Figure 2.8. Root mean square error (RMSE) is calculated for each measurement. RMSE of ϕ is 0.31° without correcting for the axial deflection, and improves to 0.22° when δ_z is removed using Eqns. 2.3 and 2.4. These results are more precise than those obtained with the previous version of the sensor hardware [38]. RMSE of δ_z and F_z are 0.04 mm and 2 mN over a 0 mm to 1 mm δ_z deflection. The expected range for deflection is calculated from quasi-static simulations and spring models [26, 53]).

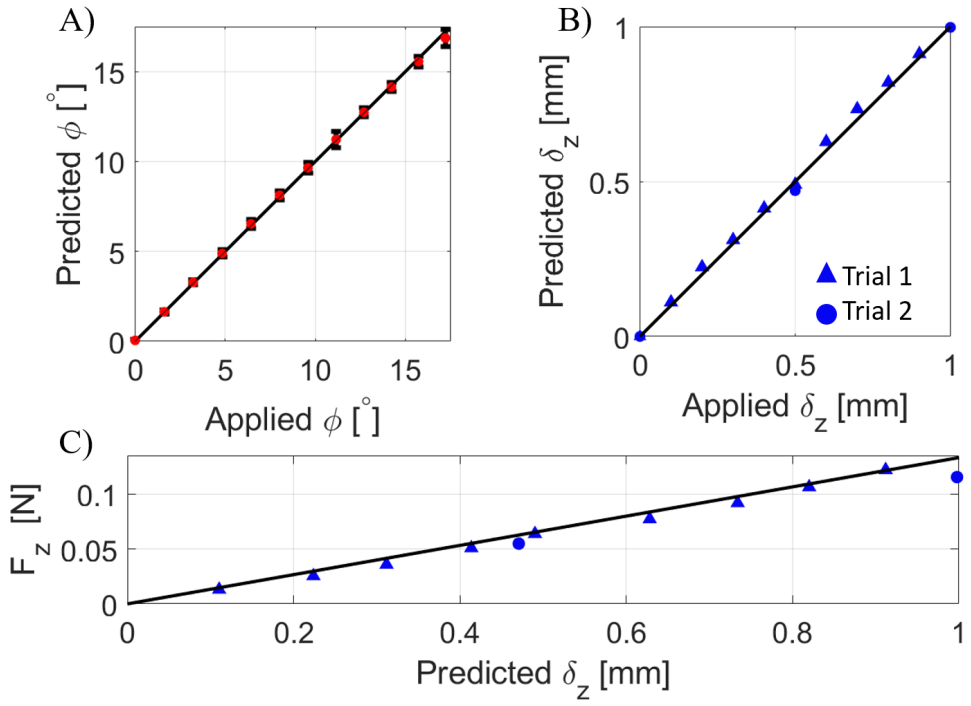

Figure 2.8: A) The accuracy of predicted ϕ is compared with applied ϕ over 18 trials. Error bars represent standard deviations. B) The accuracy of predicted δ_z is compared with applied δ_z over two trials. C) From the same test as B. The accuracy of predicted F_Z from the whisker sensor is compared with the value of F_z measured by the force-torque sensor. The black line represents the expected F_z for a δ_z deflection by the spring model. [53]

.

2.4.2 Radial Contact Distance with Rigid Contact

The Gradient-Moment (GM) algorithm provides an analytical estimate of $\hat{r}$ given the lateral distance traveled at the whisker base, Δx, and the estimated ϕ as calculated in Eqn. 2.9. Using the experimental data collected from the various contact heights shown in Figure 2.9A, the best fit for constant C in Eqn. 2.9 was found to be 132. Accuracy and precision of this method can be quantified by examining the error in radial contact distance, $r - \hat{r}_{GM}$. The mean (μ_{GM}) and standard deviation (σ_{GM}) of this error across all data in Figure 2.9A is presented in Table 2.2. The values in this table were obtained at varying ranges of ϕ; precision is often shown to improve as ϕ increases in previous applications of the MF and sweeping method algorithms [39, 40]. The GM algorithm represents an accurate measurement with high precision given the mean close to zero and a standard deviation of approximately 3 mm across

a range of ϕ values.

Because the MF algorithm uses a classification approach to estimate $\hat{r}_{MF}$, experimental data should show separation between data collected at different applied contact distances in (ϕ, δ_z) space. To avoid cluttering, Figure 2.9B shows only two applied contact distances, corresponding to 42 mm and 50 mm. These two distances show clear separation, especially at larger values of ϕ. Similar to the GM results, μ_{MF} and σ_{MF} are calculated for the error in radial contact distance estimates for the MF approach, $r - \hat{r}_{MF}$, and presented in Table 2.2. Both the accuracy and precision of $\hat{r}_{MF}$ improve as ϕ increases, but the MF algorithm is clearly outperformed by GM in this case of rigid contact.

Table 2.2: Distance error $r - \hat{r}$ [mm] on a rigid surface

$\phi <$	μ_{GM}	σ_{GM}	μ_{MF}	σ_{MF}
2.5°	0.5	3.2	0.6	20.3
5°	0.5	3.1	0.5	19.4
10°	0.4	3.1	0.7	17.4
20°	-0.3	2.8	0.2	13.3

2.4.3 Radial Contact Distance with Compliant Contact

Contact with the pipe cleaner is an expected failure mode for the GM algorithm because the pipe cleaner bends during contact. The GM algorithm overestimates $\hat{r}$ when contacting a compliant surface because the whisker bends less than expected. This expected result is borne out in the large negative values for the means of the radial contact distance error (μ_{GM}) presented in Table 2.3. The MF algorithm accuracy outperforms the GM algorithm on a compliant surface, but precision (represented by σ_{MF}) remains poor in comparison to the GM method. Data from experimental measurements summarized in Tables 2.2 and 2.3 are also presented using box and whisker plots in Figure 2.10.

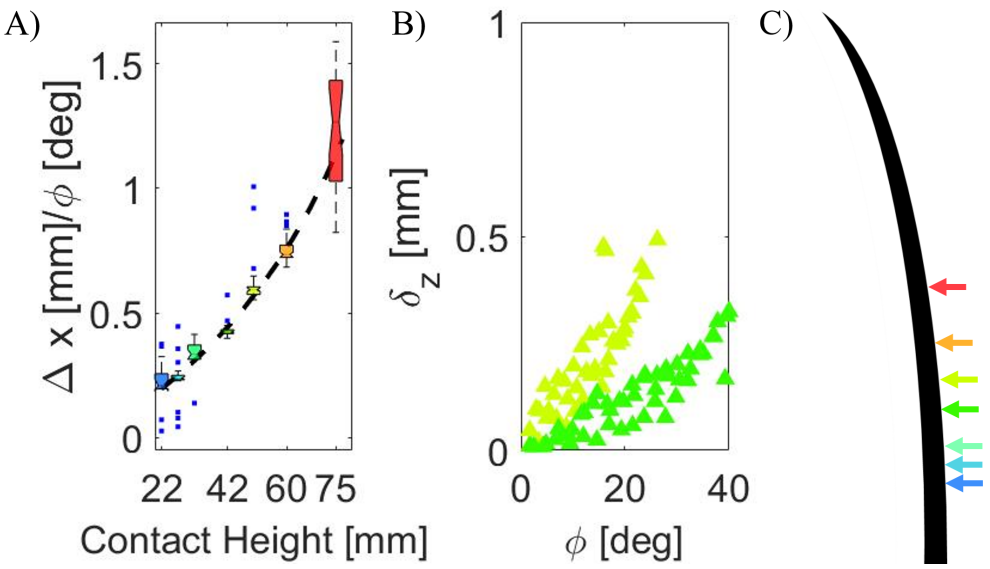

Figure 2.9: Values for ϕ, δ_z, and applied translation Δx were collected for the flexible whisker against a rigid contact at seven contact heights. A) The model in equation 2.9 is plotted against box plots, illustrating the distributions of the experimental data. The applied r values and experimentally measured $\frac{\Delta x}{\phi}$ were used to estimate constant C. Each box plot had a minimum of 18 data points. B) The MF algorithm uses classification on the ϕ vs δ_z graph to identify radial contact height. Example data from two applied r values (42 mm and 50 mm) are plotted here. C) The applied contact distances relative to l_w.

Table 2.3: Distance error $r - \hat{r}$ [mm] on a compliant surface

$\phi <$	μ_{GM}	σ_{GM}	μ_{MF}	σ_{MF}
2.5°	-23.5	8.2	7.4	24.6
5°	-23.5	8.2	4.6	24.2
7.5°	-23.6	8.3	0.9	22.6
10°	-23.1	1.1	-3.5	19.6

2.4.4 Z-Dissimilarity Score

We tested the Z-Dissimilarity score defined in Eqn. 2.12 on the data collected from rigid contact, compliant contact and the shape reconstruction task. Because the goal of the Z-Dissimilarity score is to identify times of incorrect prediction, we compared the Z-Dissimilarity scores with errors in radial contact distance estimation (e.g., $r - \hat{r}_{GM}$). A Z value above 1 indicates that the difference between the two $\hat{r}$ estimates is not likely to be explained by the standard deviation. When $r - \hat{r}_{GM} > 15$ mm, the Z-Dissimilarity score was greater than 1.0 for 82 % of the compliant contact and rigid contact data and greater than 0.5 for 94 % of the data. In contrast, when

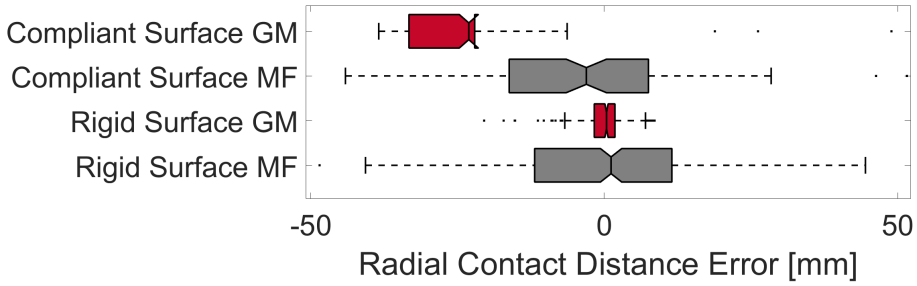

Figure 2.10: Boxplots of the error in radial contact distance estimation $r - \hat{r}$ using the GM and MF algorithms are compared on both compliant and rigid surfaces.

$r - \hat{r}_{GM} < 15\,\text{mm}$, the Z-Dissimilarity score was greater than 1.0 for 26 % of the data and greater than 0.5 for 36 % of the data. Although not a perfect measure of uncertainty, the Z-Dissimilarity score is a strong indicator of instances when more data might be needed to improve the estimate of radial contact distance.

A shape reconstruction task provides a graphical indication of Z-Dissimilarity score as shown in Figure 2.11. Sliding along a surface represents a second common failure mode for radial contact distance estimation. Upon initial contact, the GM algorithm is more precise and accurate as it traces the cube and cylinder shapes. However, as the translation increased and the gradient of the surfaces decreased, the whisker began to slip; during slip, the MF method maintained its accuracy while the GM method lost accuracy, and the Z-Dissimilarity score increased as indicated by the heatmap colors in Figure 2.11.

2.5 Conclusion

In this work we demonstrated a new whisker sensor system design that can sense the information required to implement two algorithms for radial contact distance estimation: Gradient-Moment (GM) and Moment-Force (MF). Using this sensor, we measured accuracy and precision for both methods and demonstrated that the GM algorithm does not accurately estimate radial contact distance during compliant contact and contact with slip. We introduced a Z-Dissimilarity score that can indicate these failure modes and showed that the MF algorithm can provide an

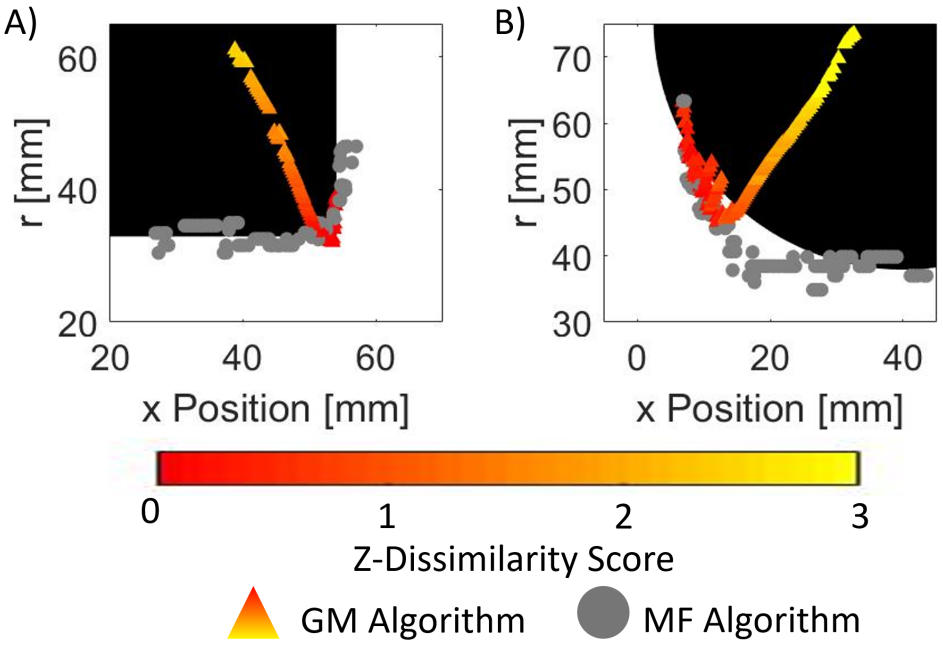

Figure 2.11: A linear stage swept the whisker across a box (left) and the circular cross-section of a water bottle (right) while data were collected from the sensor. Radial contact estimates from the GM algorithm (red/yellow) and the MF algorithm (gray) are compared. The GM algorithm can accurately and precisely localize the contact point until the whisker begins to slip, at which point the accuracy decreases significantly. The MF algorithm is less precise but remains accurate during slip. The Z-Dissimilarity score determines the color of each point plotted for the GM algorithm.

accurate, albeit noisy, contact distance estimate when the GM algorithm fails.

The whisker sensing system in this paper relies on a few key assumptions:

1. We estimate radial contact distance only when the whisker is in quasi-static conditions

2. We assume the whisker makes contact with only one object at a given time.

3. We assume all GM failure cases result from a reduced bend of the whisker. This assumption fails if an object moving towards the whisker.

4. We did not examine the direction of whisker bending.

Addressing these assumptions provides several avenues for future work.

It should be noted that our sensor generates predictions that are as precise as other MF sensors [40], but performs considerably worse than the GM algorithm in

cases of contact with a rigid object, due to poor resolution in δ_z. Non-slipping, rigid contact can be used for many applications and the $\hat{r}_{GM}$ estimate is a simple equation. Applying $\hat{r}_{GM}$ with our Z-Dissimilarity score could allow robots with whiskers to traverse space quickly, only slowing down when the robot predicts a more difficult mapping. The score allows researchers to remove data points above a threshold, incorporate the uncertainty into the mappings based on task requirements, or switch to the MF algorithm. The algorithm could also potentially help the robot determine when to make a whisk, i.e., when to reset the sensor in space. Combining multiple sensing algorithms can also have other benefits for whisker sensing. For example, the combination could be used to map surface compliance as suggested in [26] or to increase accuracy and precision during tapping contact [45, 48].

Chapter 3

Whisker Classification of Multiple Stimuli

Paper:

Kent, T. A., Kim, S., Kornilowicz, G., Yuan, W., Hartmann, M. J., & Bergbreiter, S. (2021). Whisksight: A reconfigurable, vision-based, optical whisker sensing array for simultaneous contact, airflow, and inertia stimulus detection. IEEE Robotics and Automation Letters, 6(2), 3357-3364.

My Contributions:

While the single whisker prototype was developed as a team. I progressed the research to an array and performed experiments on the classifying stimuli section. I also developed the code and algorithms which converted the camera images into sensor information. I developed the initial paper draft and figures.

Author Contributions:

TK, SK and GK designed an early version of the sensor. SK had the idea to use magnets to attach the whiskers to the membrane. WY provided extended feedback on the early version of the prototype. TK developed the whisker array, all code and algorithms. MH and SB guided the research and the paper's applications. All

edited the manuscripts and figures.

Abstract

The development of whisker-based sensing systems faces at least two important technical challenges: scaling up the number of whiskers to large arrays while retaining a simple interface; and detecting the wide variety of stimuli that biological whiskers can sense, including both direct touch (contact) and airflow. Here we present the design for a whisker array that leverages a camera to measure whisker rotations without a complex interface. Whiskers are magnetically attached to an elastomer "skin," ensuring that the system is both scalable and reconfigurable. Direct contact is measured from the relative motion between each whisker and the skin, while airflow and inertia can be inferred from the signal experienced by all whiskers in the array. Individual whiskers can resolve the direction of contact transverse to the whisker with a root mean square error of 6.2° and whisker rotation magnitude to with a root mean square error of 0.5°. An algorithm is developed to distinguish inertial forces from airflow and contact.

3.1 Introduction

Whiskers, also known as vibrissae, are important tactile sensors for almost all mammals. Mammalian whiskers are arranged in bilateral arrays, with ∼25 or more whiskers emerging from each side of the animal's face [54]. Unlike insect antennae, which have mechanical and chemical sensors along their entire length, mammalian whiskers resemble hairs; sensing occurs only at the whisker base within a densely-innervated follicle [55]. Animals use their whiskers to help with rapid motion planning and navigation, to localize contact with objects, to distinguish object size, shape, texture, and orientation, and to sense fluid flow. Moreover, whisker-based sensing can distinguish between stimuli that occur simultaneously (e.g., contact can be distinguished from the inertial forces generated by the animal's own motion).

Not surprisingly, engineers have tried to replicate these sensory systems on robots for similar tasks. Several engineered systems have exploited whisker bending to perform contact point determination with a single whisker ([27, 31, 39, 40, 56]). Other studies have used whiskers primarily as contact/non-contact detectors to develop algorithms that orient the entire array towards an object [57–59]. Yet other whisker-inspired sensors have been designed to detect non-contact mechanical stimuli such as flow (e.g., [31, 35, 60, 61]). Ultimately – if the full capabilities of the biological system are to be realized in hardware – these approaches will need to merge, but important technical challenges remain.

The first challenge involves the number of whiskers in an engineered array, especially if detailed information about individual whisker bending is to be retained. Natural whiskers each have their own complex, multi-dimensional transduction mechanism [55]. In an engineered system, adding transducers to each whisker significantly increases computational and hardware complexity. The largest engineered whisker arrays have used 18 [59] and 20 [58] whiskers with one transducer per whisker. By capturing deflections and (motor-controlled) rotations of each whisker, these arrays could determine the identities of the whiskers that made contact and then orient the array to a detected object. Although these arrays are impressive engineering feats, they are costly and complex; wiring scales with whisker number.

An alternative approach, taken by "TacWhiskers," uses a single camera as the transducer for a whisker array [41], similar to the approach used by several recent non-whisker tactile sensors (e.g., [62–64]). Although modern cameras use millions of photoreceptor-like elements, we classify a camera as a single transducer in this work because it has a single interface. The TacWhiskers used a modified version of the TacTip sensor described in [62]; a camera monitors the movement of 3D printed pillars beneath a domed array of whiskers. The whiskers were reported highly accurate during convergent whisking contact of an array of ten whiskers.

A second challenge is that a wide variety of stimuli – with amplitudes that can vary over several orders of magnitude – can impart forces and motions to the

whiskers. Direct contact (touch), airflow, and motion at the whisker base (which we will call inertial) stimuli can all be sensed by whiskers. Discriminating between these various stimuli is still an unmet challenge. We are aware of only two papers that demonstrated a single whisker that could detect (but not distinguish between) contact and flow [60, 65]. This is a notable gap, as airflow, inertia, and contact are all realistic stimuli that could be introduced as intentional or confounding variables in robotic implementation [66].

The primary contribution of this paper is to show that a reconfigurable, vision-based whisker array sensor (WhiskSight) can sense and discriminate between multiple stimuli. Building on the TacWhiskers approach ([41, 62]), the present work uses a variation on the GelSight tactile sensor [63] to measure whisker rotations and to distinguish between contact, airflow, and inertial stimuli (Figure 3.1). Whiskers are magnetically attached to a light-blocking elastomer membrane suspended above a camera. Magnetic attachments ensure modularity, scalability, and reconfigurability. Using a commercially available USB camera we demonstrate that the system can simultaneously gather information about whisker rotations in a 6-whisker array. Similar to the GelSight tactile force sensor [63], FingerVision [67], and GelForce [68], we use markers on the elastomer membrane to track deformations of the membrane in addition to the whisker movements. This extra information allows us to discriminate between different stimuli (contact, airflow, inertial) as well as to detect the direction and magnitude of individual whisker rotations regardless of rotations and deflections elsewhere in the array. Notably, WhiskSight achieves these capabilities even though it is not actuated. This new approach to whisker sensing could enable robotic navigation and obstacle detection/avoidance in low visibility settings without confounding data from system motion or airflow.

3.2 WhiskSight System Design

The WhiskSight system design is based on a scaled up version of the GelSight sensor [63] and is illustrated in Figure 3.1. The system includes a camera, an elastomer

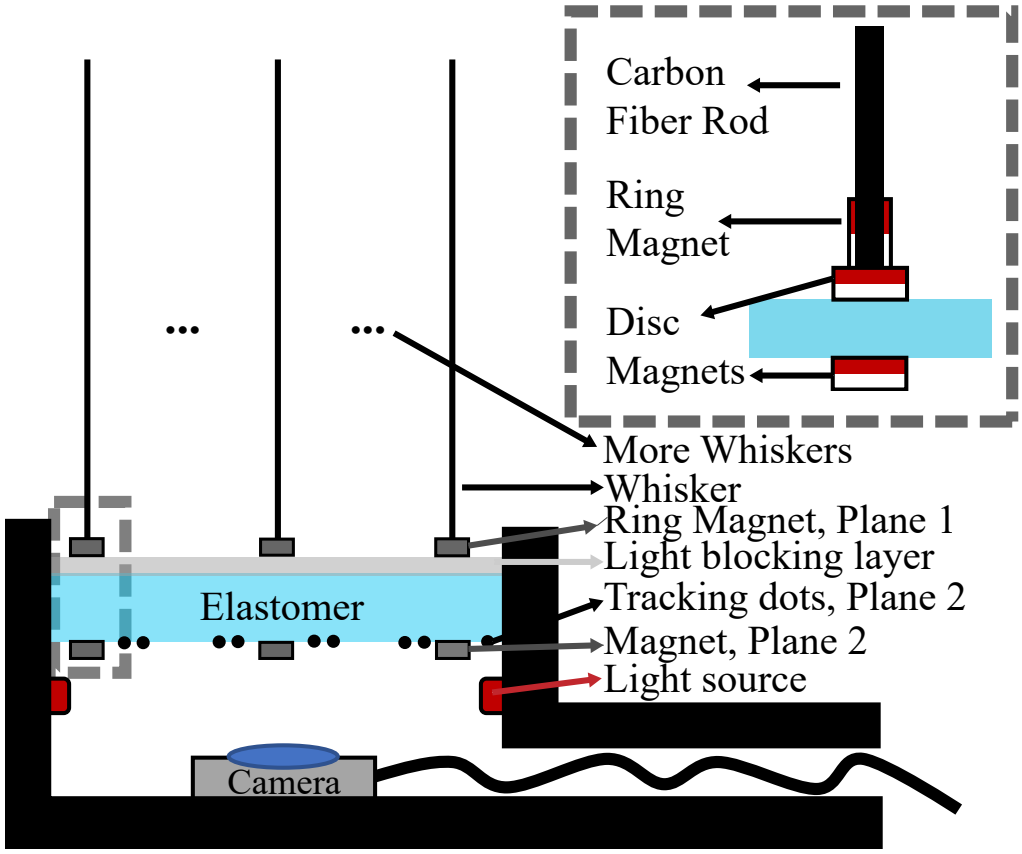

Figure 3.1: A schematic of the WhiskSight sensor. Whiskers (rigid carbon fiber rods) are attached to an elastomer membrane suspended above a camera. The attachment is magnetic, using a disc magnet attached to the whisker on top of the membrane and another disc magnet below the membrane. The camera captures whisker rotations along with the motion of tracking dots on the membrane. A light blocking layer and internal LEDs ensure consistent lighting. The image is not to scale.

membrane, magnetically attached rigid whiskers, and a light source. The elastomer membrane, held in tension, suspends the whiskers over the camera. The camera senses rotations and deflections of each whisker. As seen in Figure 3.2, θ represents the whisker 'rotation direction,' ϕ represents the 'rotation magnitude,' and 'z-axis deflection' represents a deflection of the elastomer membrane parallel to the whisker z-axis, typically caused by an axial force applied to a whisker.

More specifically, the camera tracks translation of the magnets as well as the tracking dots painted on the bottom surface of the elastomer membrane in the image plane described by u-v coordinates (Figure 3.2). Software correlates these translations back to rotations applied to individual whiskers. The light source internal to the sensing system decreases the effect of ambient lighting on the camera

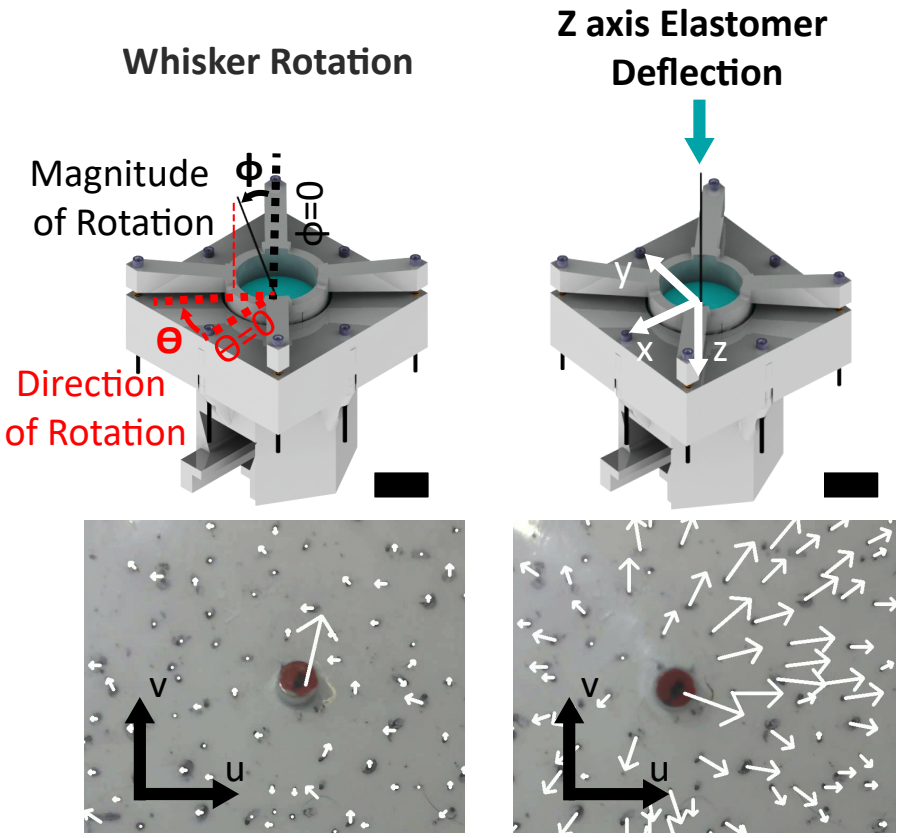

Figure 3.2: Coordinate systems for stimuli applied to rigid whiskers. Top row: The angles θ and ϕ (degrees) represent the direction and magnitude of whisker rotation from nominal (perpendicular to the elastomer membrane). The 'z-axis deflection' quantifies displacement in millimeters as the whisker moves parallel to its z-axis. Scale bars=30 mm. Bottom row: The images show typical camera output for whisker rotation (left) and z-axis deflection of the elastomer (right). The motion of a tracker dot on the whisker magnet or the elastomer is described as 'translation' in a u-v coordinate system. In both images, arrow magnitudes show translation of the dots scaled by 10x for visual clarity. Scale: magnet diameter (red circle) is 3.2 mm.

image, thereby improving consistency of the tracking algorithm.

3.2.1 Mechanical System

To enable reconfigurability, whiskers are attached with magnets to the elastomer membrane as shown in Figure 3.1. Each whisker consists of a 1 mm diameter, 100 mm long carbon fiber rod glued into a ring magnet, which is then glued on a disc magnet. Unlike biological whiskers, which are flexible and have taper, the carbon rod whiskers are stiff and have constant diameter. Using magnets on both the top and bottom of the membrane, whiskers can be attached anywhere within camera view. The

disc magnets are 3.175 mm diameter, 1.58 mm thick nickle-plated NdFeB axial force magnets (DH11, KJ Magnetics). The ring magnets are 3.175 mm outer diameter, 1.58 mm thick nickle-plated NdFeB axial force magnets (R211, KJ Magnetics) with a pull force of 0.31 pounds.

The rest of the sensing system is modular. The camera (Logitech HD Webcam C310) can be slotted into a hexagonal 3D printed camera assembly. This assembly holds the LEDs (LilyPad, DEV-13902) used as a light source halfway up the casing with wire pass-throughs in the casing (Figure 3.3). The elastomer membrane is $\approx$ 1 mm thick PDMS (Sylgard 184, Dow Chemical). The top of the PDMS is painted white with acrylic paint and black dots are made with marker on the bottom. The top and bottom holders clamp the elastomer in place, after which a tensioner is used to push the elastomer membrane downward to place it in tension. The tension in the elastomer can be adjusted by tightening the tensioner screws. The whiskers are added to the system only after the elastomer is in tension so that magnetic interaction does not affect the elastomer tension (Supplementary Video). Finally, the entire system is placed over the camera assembly and screwed into place. It should also be noted that this setup is designed to test and characterize the whiskers; a robotic implementation could be made far more compact.

3.2.2 Whisker and Membrane Tracking

Typical views captured by the camera can be seen in Figure 3.2. The entire bottom of the magnet is painted red/orange so that the whiskers' locations can be more easily resolved and to reduce reflection from the magnets. Black tracker dots are marked on both the bottom of the elastomer and the bottom of the magnets using a permanent marker. The dots and whiskers are initially identified using a custom segmentation algorithm, then tracked during tests using various tracking algorithms; Minimum Output Sum of Squared Error Tracker (MOSSE) [69] was chosen for its accuracy and speed, and Channel and Spatial Reliability Tracker (CSRT) [70] was chosen for its accuracy. Validation tests demonstrated that MOSSE could track

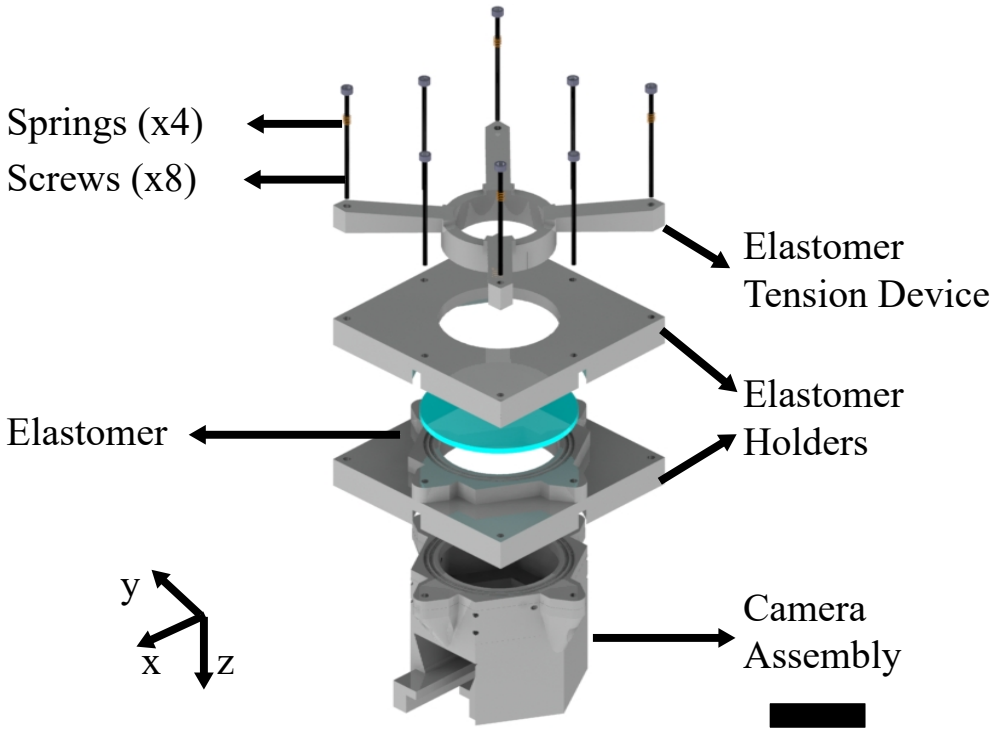

Figure 3.3: Assembly of the physical system. Scale bar represents 50 mm.

over 50 dots at 17 frames per second. Depending on the task, the tracker was either applied to pre-recorded videos, previously captured and labeled sequential images, or to live video.

Whisker rotation can be calculated using the translation of the whisker magnet in the image plane, δu and δv.

$$\theta = \arctan\left(\delta u / \delta v\right) \tag{3.1}$$

Calculating rotation magnitude requires knowledge of camera and geometric parameters including u and v axis resolution (u_{res} and v_{res}), u and v angle of view (u_{aov} and v_{aov}), distance between the camera and membrane (ΔZ), and the height of the magnet (h_{mag}) [71]. These parameters are used to calculate the average pixels per mm^2 (ρ); because the camera's resolution (pixels/mm) is not identical in the u and v directions, we average the two.

ϕ can then be calculated with these parameters and the assumption that the

points of interest all occur in a plane ΔZ away from the camera parallel to the image plane. Eqn. 3.3 converts the translation of the bottom of the magnet (pixels) into millimeters and then uses the known height of the magnet to obtain the rotation magnitude, assuming the translation is primarily in-plane.

$$\rho = \frac{1}{2}\left(\frac{\Delta Z}{u_{res}} \tan\left(u_{aov}\right) + \frac{\Delta Z}{v_{res}} \tan\left(v_{aov}\right)\right) \tag{3.2}$$

$$\phi = \arctan\left(\rho\sqrt{\delta u^2 + \delta v^2}/h_{mag}\right) \tag{3.3}$$

In the whisker system shown in Figure 3.3, $h_{mag} = 1.58\,\text{mm}$ and $\Delta Z = 54\,\text{mm}$. For the chosen camera, $u_{res} = 1280$ pixels, $v_{res} = 720$ pixels and the angle of view in the u-direction $u_{aov} = 26.95°$, v-direction $v_{aov} = 16.26°$. The z-axis deflection was not calculated but was accounted for using the movement of the dots surrounding each whisker. This motion was previously characterized in [63]. To determine whisker motion independent of membrane motion (which could be affected by neighboring whiskers or other stimuli), the membrane tracking dots closest to the whisker magnet were found using the L2 norm for distance. The average translation along u and v (pixels) of the k nearest dots was subtracted from the translation (pixels) of the whisker magnet. We ensured that dots were spaced at regular angular intervals around the whisker magnets.

3.3 Contact Characterization

To start, the whisker rotations and deflections that occur from direct touch (contact) with a whisker are characterized.

3.3.1 Experimental Setup

A Thorlabs manual stage with two linear axes and one rotation axis was used to apply known rotation directions (θ) and magnitudes (ϕ) to a single whisker (Figure 3.4a.). To test the system's response to various whisker rotation directions, θ was

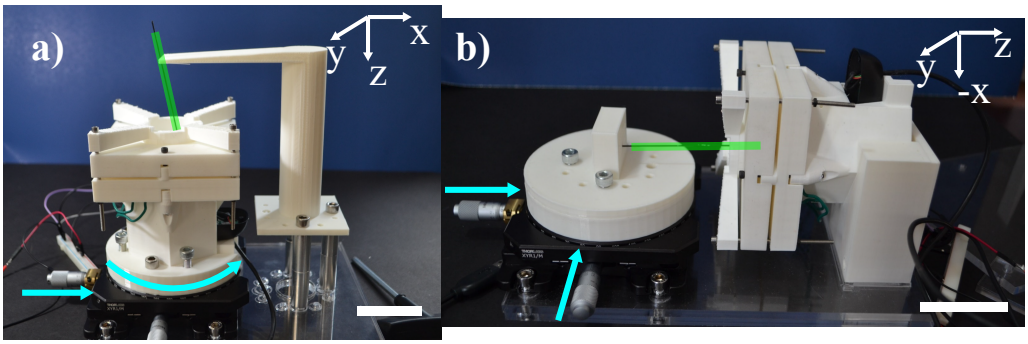

Figure 3.4: a) A test setup in which rotation magnitude (ϕ) and direction (θ) can be controlled. b) A test setup that can apply z-axis deflections and rotation about the y-axis. Scale bars = 50 mm. In both figures a green line has been drawn over the whisker for visual clarity. Cyan directional arrows indicate directions of stage motion.

incremented from 0° to 360° in 10° steps while ϕ was fixed at 7°. Whisker rotation magnitude, ϕ, was characterized by rotating the whisker in 0.49° increments along the positive x-axis. Linear translations of the stage used to deflect the whisker are converted to angles using the known geometry, and the MOSSE tracker was used to track dots.

Next, using the setup shown in Figure 3.4b, we evaluated how rotation measurements would be affected by z-axis deflections. We hypothesized that z-axis deflections could be subtracted from the total motion by monitoring both the magnet translation and the nearby elastomer membrane translation. The whisker was rotated about the x-axis ($\theta = 90°$) from $-2.77°$ to 2.77° in 21 equal steps. Each test was repeated with z-axis deflection ranging from 0 mm to 5 mm. Because this experiment used very small angular increments (0.29°), the tracker was changed to OpenCV's CSRT tracker, which has better (sub-pixel) accuracy than MOSSE.

In a separate set of experiments, we tested the effect of z-axis deflections when the whisker was placed at two different offsets (small and large) from the image center. The offsets determine how the whisker magnet will translate in the camera image during a pure z-axis deflection. If the magnet is centered in the camera image, it will appear to grow in size while staying fixed in position. If the magnet is offset from the image center, it will not only appear to grow in size but also appear to translate in the camera image. If the offset is too large, the magnet will ultimately

translate out of the image for a sufficiently large z-deflection [71].

The final characterization of contact stimuli tested a whisker array. Contact on other whiskers in the array or other stimuli like airflow applied to the whiskers can make it challenging to detect contact on an individual whisker. In the WhiskSight sensor, the relative motion between the elastomer membrane and whisker magnets can be used to determine contact. If the difference between the net translation of the elastomer dots surrounding a whisker and the translation of the whisker magnet was greater than a threshold, contact was indicated. To test this approach, we applied rotations to single whiskers in a 6-whisker array, and recorded if the correct whisker was indicated as the one in contact. In addition, we monitored all of the other whiskers to evaluate if they falsely reported contact or correctly reported no contact (false positives and true negatives). We then applied a z-axis deflection to one of the whiskers in the array and repeated the contact test on the remaining five whiskers, recording all true positives, false positives, and negatives. Each of these experiments was repeated twice. Two metrics were used to evaluate the accuracy of different threshold values: the percentage of true positives and percentage of true negatives.

3.3.2 Experimental Results

Whiskers were first characterized with contact applied to individual whiskers. Figure 3.5a shows a high-quality fit (RMS error = 6.2°) between the applied rotation direction, θ, and the whisker rotation predicted from the camera image. The error is slightly larger than the theoretically best achievable accuracy of our system (5.35°) due to discrete pixel displacements. With a higher resolution camera, we would expect the accuracy to increase. In addition, as rotation magnitude, ϕ, increases, the direction accuracy is expected to improve due to larger δu and δv in Eqn. 3.1.

Limitations imposed by camera resolution are easily observed in Figure 3.5b, which plots measured rotation magnitude, ϕ, versus the experimentally-applied rotation magnitude. At each step a 0.49° increase in ϕ was applied, but the dot on

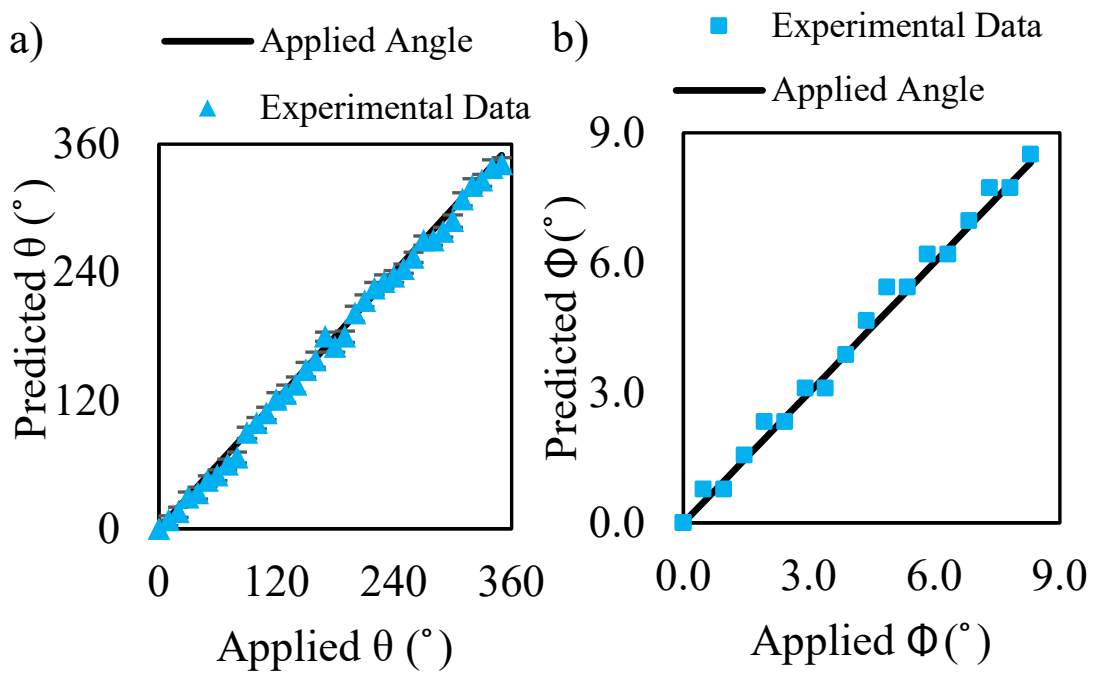

Figure 3.5: a) The value of θ predicted from the camera image (blue triangles) is compared to the value of θ applied by the testing system (black line). Error bars represent the full range of possible values for θ that a given u, v pixel location could represent. b) The value of ϕ predicted from the camera image (blue squares) versus applied ϕ (black line).

the whisker magnet does not always translate to a new pixel with each step. Based on camera and geometric parameters, an accuracy of 0.5° is expected for ϕ. The measured mean RMS error between the applied ϕ and the predicted ϕ angle is 0.25° – close to the expected accuracy. The accuracy of ϕ is significantly higher than the accuracy of θ. This result can be explained by two factors. First, 1° of rotation in ϕ causes significantly more pixel movement than 1° in θ. Second, the experimental measurement of ϕ was limited to motion along a single axis.

The rotation testing described above was performed without z-axis deflections. Membrane deflection is of particular concern because it changes the distance between the camera and elastomer surface, which is assumed constant in Eqn. 3.3. The nominal distance between the camera and membrane is small (54 mm), increasing the possible effect of small deflections. Translation during elastomer deflection can be further magnified when the whiskers are offset from the camera center, and this offset varies significantly across a whisker array. In Figure 3.6, it is clear that

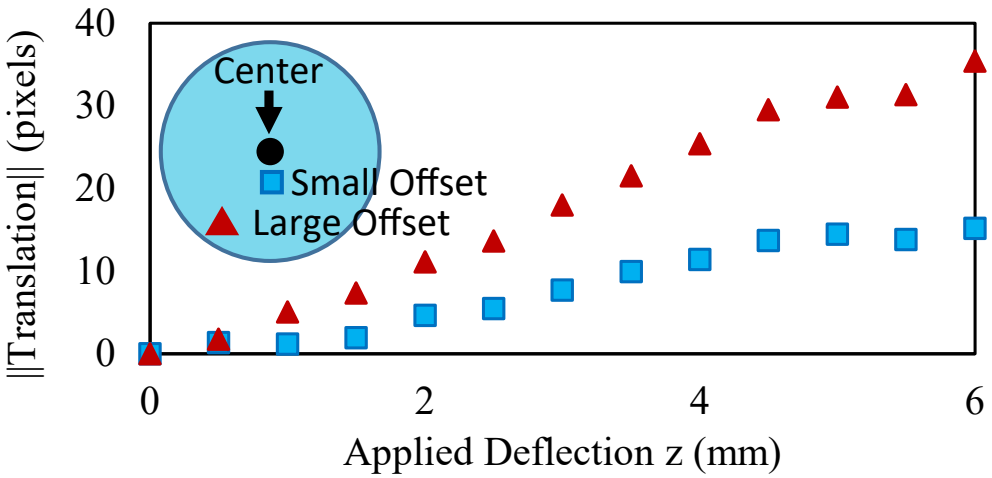

Figure 3.6: As the whisker location moves away from the center of the camera image, z-axis deflection has an increasingly large effect on the magnet's apparent translation in the camera image. This is represented as L2 norm of $(\delta u, \delta v)$. A whisker at the camera center would have zero translation.

measured translation due to applied z-axis deflection differs greatly depending on the whisker offset in the camera image; a deflection applied to a whisker at large offset is (incorrectly) predicted as three times the magnitude of the same deflection applied to a whisker with a small offset. Without mitigation this could have a detrimental affect to measuring independent whisker rotations in an array.

Fortunately, by tracking the membrane dots in addition to whisker magnets we are able to overcome this possible problem. As illustrated in Figure 3.2, during whisker rotation the pixel translation is mostly limited to the bottom of the magnet but in z-axis deflection the entire membrane moves. Using the experimental setup seen in Figure 3.4b we were able to test our ability to remove the effect of z-axis deflection. We subtracted the average translation of the nine elastomer dots closest to a whisker undergoing a rotation about the x-axis while the membrane was deflected from 0 mm to 5 mm in 0.5 mm increments.

We first defined the "zero curve" as the ϕ predicted using this subtraction method when zero deflection was applied. Results shown in Figure 3.7 revealed that the 5 mm prediction curve shifts to align with the zero deflection curve when elastomer translation is taken into account. With this subtraction method, the RMS error between the zero curve and other curves was an average of 0.37° , whereas without the

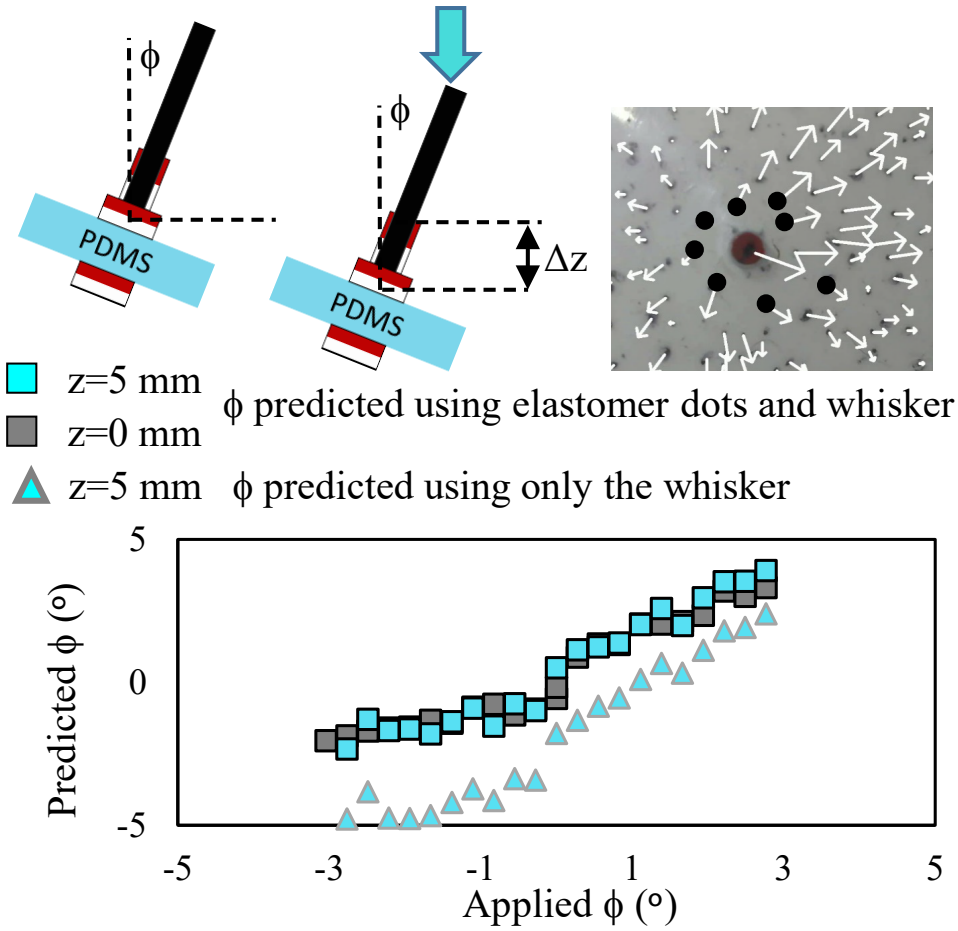

Figure 3.7: By subtracting the average translation of the nine closest elastomer dots (white arrows, 10x magnification) from translation of the dot on the magnet (red base), we can more accurately predict the angle ϕ during whisker deflection. The predicted ϕ that uses only the whisker translation (blue triangles) is significantly offset from the "zero curve" (grey squares). ϕ predicted using this subtraction method (blue squares) removes this offset, resulting in accurate predictions even under z-axis deflection.

subtraction method the RMS error grew aggressively up to 1.79° at 5 mm deflection. Only the 0 mm and 5 mm deflection results are shown in Figure 3.7 for clarity.

Exploiting the ability to isolate rotations from z-axis deflections, we tested an algorithm to distinguish tactile contact applied to individual whiskers in an array. When one whisker in an array is rotated or deflected, the resulting translation of the elastomer membrane could show up as unintended noise for other whiskers in the array. To account for this, contact for each whisker of a six-whisker array was indicated by a significant difference between the translation of the whisker magnet and the net translation of the closest six membrane dots to the whisker magnet. Six

dots were chosen instead of nine to reduce any influence from nearby whiskers in the array. The translation threshold for significance was an independent variable. A key tradeoff in this approach is the minimum rotation magnitude, ϕ, required to indicate contact. Lower thresholds are more likely to pick up noise from surrounding whiskers while a large threshold requires a much larger whisker rotation to achieve the necessary pixel translation.

The first two trials rotated a single whisker only. In the second two trials, one whisker was deflected along the z-axis to deform the membrane while other whiskers were rotated. When the threshold was small (0 or 1 pixel) the accuracy of detection was reduced to 80 % because of the large number of false positives. Using a higher threshold of 4 or 5 pixels resulted in only one false negative during the deflection plus rotation trials. In these large threshold cases, the required rotation magnitude is also expected to be relatively large ($\approx 6^\circ$ to 8°). As a result, a contact threshold of 3 pixels was chosen as the best threshold for future tests given the balance of high accuracy and small ϕ required to trigger the contact condition (Supplementary Video).

3.4 Airflow and Inertial Stimuli Characterization

After quantifying the response of whiskers to contact stimuli, we sought to understand the response to airflow and whisker motion due to inertial effects.

3.4.1 Experimental Setup

To study the effects of airflow, the whiskers were subjected to high, medium and low flow speeds using a 10 A Stanley fan (Model 655704). No attempt was made to make the flow laminar, as we were primarily interested in detection of airflow that may naturally occur in an environment. Airflow velocity was not measured. In a second airflow experiment, contact was applied to an individual whisker simultaneously with the airflow stimuli (Supplementary Video).

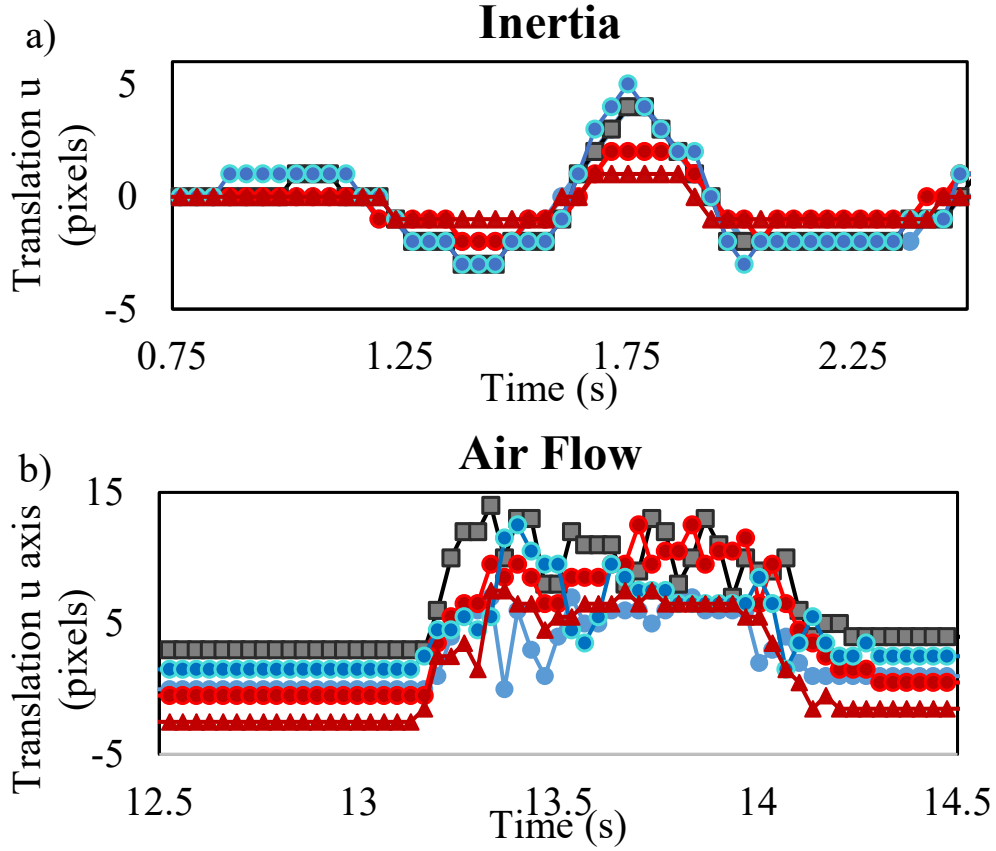

Figure 3.8: Response to a) inertial stimuli, and b) airflow stimuli. Both plots show the measured response of five of the six whiskers in the array. The same whiskers are shown in each panel and the colors are matched by whisker.

Active whisking in rodents is known to generate inertial effects [72, 73]. To approximate actuated, inertial whisking, the full whisker system (Figure 3.3) was rotated back and forth manually (Supplementary Video). Active whisking can confuse robotic systems [66] but poses no problems for animals. Rotations and translations were performed around both the x and y axes to better understand the signals generated under base excitations.

3.4.2 Experimental Results

When the whiskers undergo rotations due to airflow and inertial stimuli, the signals differ significantly, especially in frequency (Figure 3.8). In addition, a key distinction from the contact stimuli discussed previously is that these non-contact mechanical stimuli generally affect all whiskers in an array similarly.

Consistent with results from rodent whiskers [74], the varying flow speeds are primarily characterized by changes in the mean rotation magnitude as seen in Figure 3.9. This figure describes translation of one whisker in the array once its response has reached steady state. Translation of each whisker in the array as well as transients can be seen in Figure 3.8b. A whisker's response to airflow has two characteristic features: the translation oscillates, and the average whisker translation is significantly ($\approx$ 5x) larger than the translation of the elastomer membrane (Supplementary Video). Although the mean translation depends on flow speed, the oscillation patterns are consistent across the flow magnitudes. This frequency of the oscillation pattern can be explained by the flow turbulence and the natural compliance and damping properties of the elastomer.

We also demonstrated that the system could sense contact in the presence of airflow (Supplementary Video). In Figure 3.10, medium speed airflow is applied across an array of whiskers in the +x direction (a single whisker is plotted for clarity). Contact events are observed as clear data spikes relative to the relatively static translation from airflow. The contact is applied with varying rotation directions, θ, as evidenced by spikes with varying u and v magnitudes. It is important to note that contact in airflow will be more challenging to distinguish if a contact stimulus is applied to many whiskers.

Figure 3.8a shows the translation of the whiskers when a large acceleration was applied to the whisker sensing system (Supplementary Video). Like airflow, inertial forces generated by motion of the base cause all whiskers to move in a very similar pattern. However, the response to an inertial translation can be distinguished from airflow by the frequency content: inertial motion results in relatively smooth, low frequency whisker translation when compared to the higher frequency oscillations associated with airflow.

In addition, the elastomer membrane translation is much more significant during an inertial stimulus in comparison to airflow (Supplementary Video). Figure 3.11 plots the translation of a whisker and its six closest membrane dots in response to a

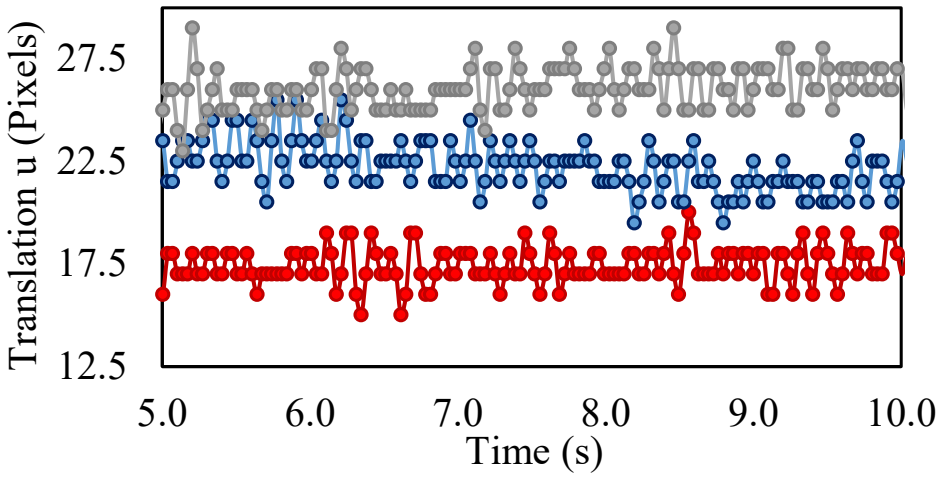

Figure 3.9: The response of one whisker in the array to airflow of low (red), medium (blue) and high (gray) speeds in steady state. Although responses to the three speeds have different mean values, the oscillation frequency is similar for all speeds.

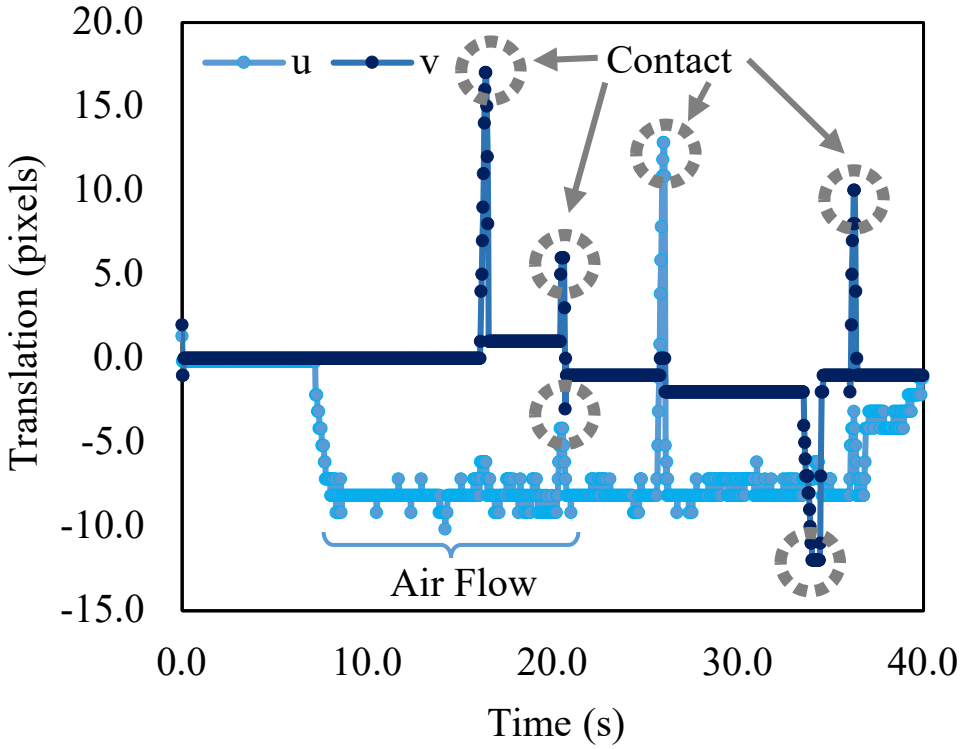

Figure 3.10: Translation in u and v of a single whisker in response to simultaneous contact and airflow. The characteristic oscillation is visible in the u translation parallel to the flow, while contact is observable in both u and v depending on the whisker rotation direction. (Supplementary video)

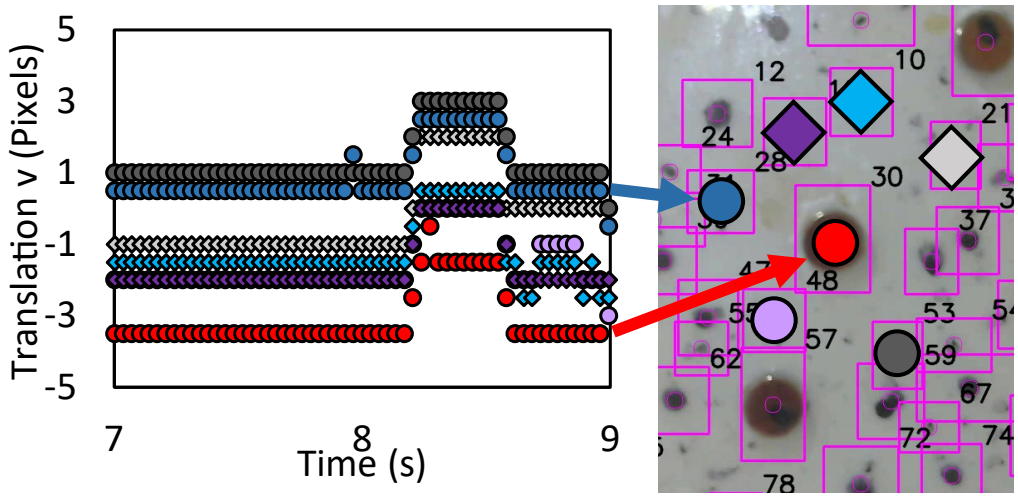

Figure 3.11: The translations of a whisker and its six closest elastomer dots are shown while the base of the system is accelerated along the system's y-axis. (Supplementary video)

base excitation. The figure shows that the six dots' responses to base excitation are remarkably similar to the response of the whisker. In other words, the whiskers and the elastomer membrane translate similarly in response to inertial stimuli. This is a key feature that will be used to distinguish contact from base excitation. However, it should be noted that a relatively large acceleration is required to capture inertial motion.

The differences in characteristics between airflow and inertial stimuli conforms with what we know about the physical sensing system. The airflow tests did not interact with the elastomer which was shielded by the protective casing but the whiskers experienced drag forces. Turbulent flow resulted in oscillatory behavior of the whiskers but no displacement of the membrane. In contrast, inertial forces affect the entire system as seen by motion in both the elastomer membrane and whiskers. The inertial forces reflect accelerations of the sensing system while constant velocity would be identified as airflow if that velocity is large enough.

3.5 Classifying Stimuli

To distinguish between touch contact, airflow, and inertial stimuli, a new algorithm was developed and tuned based on results from the contact, airflow, and inertial

characterization experiments. Eqn. 3.4 converts whisker directional translations in image coordinates, δu_i and δv_i, into the magnitude of whisker movement, $\delta W_{mag,i}$. In the equation below, i is used to index each whisker.

$$\delta W_{mag,i} = (\delta u_i^2 + \delta v_i^2)^{1/2} \tag{3.4}$$

The stimuli on each whisker is classified by 1) checking if the whisker has moved ($\delta W_{mag,i} >= 3$), and 2) determining the types of stimulus. For an inertial stimulus, the whisker magnet and membrane dots move together (Figure 3.11), while only the whisker dots move for airflow stimuli. Airflow is also indicated by higher frequency oscillations around a central offset magnitude (Figure 3.9,3.10) which are tracked by counting the number of direction changes within the previous 20 frames (corresponding to 0.66 s). If over half the full number of whiskers detect airflow or inertial stimuli (which should affect all similarly), the system is classified as detecting the relevant stimulus. If fewer than half of the whiskers have moved, contact is indicated. Contact can be detected simultaneously with airflow or inertia by then checking to see if any whisker's translation vector deviates significantly from the average. Further detail, including specific thresholds, can be found in the source code uploaded to our GitHub repository [75]. This approach works well for a small system of six whiskers, but would likely need to be modified for larger arrays in which large groups of whiskers may be in contact.

This algorithm was used on a new video in which all stimuli were present, sometimes simultaneously (contact, airflow, inertia, and airflow with contact). For these tests we used the CSRT tracker as inertia required a higher tracking accuracy. The array was able to identify stimuli correctly each time and individual whiskers were accurate most of the time (Supplementary Video, Figure 3.12). The individual whisker errors are most likely the result of tracker drift and could continue to be improved for future robotic implementations.

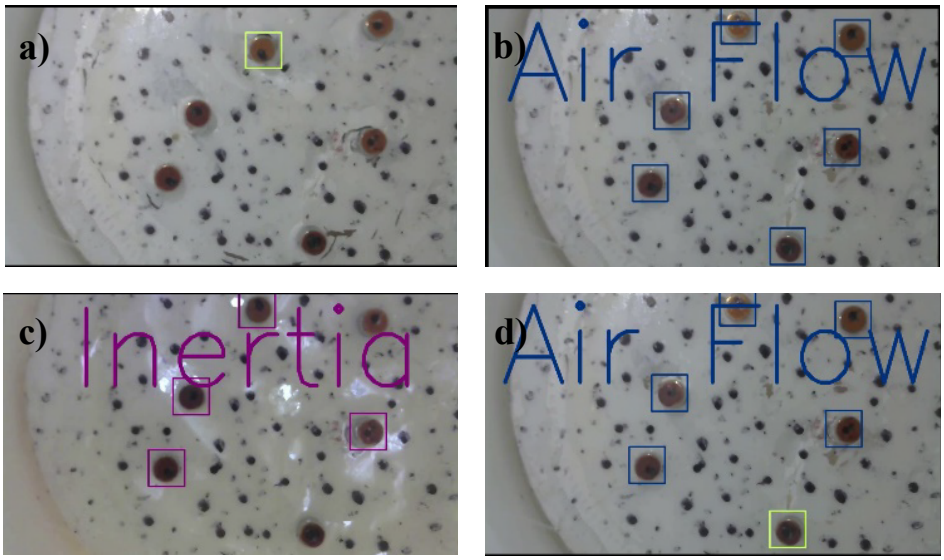

Figure 3.12: Frames from the supplementary video show that the WhiskSight can correctly classify varying applied stimuli: a) a single whisker in contact (green), b) the entire system exposed to medium speed airflow (blue), c) the WhiskSight base accelerated to generate inertial stimuli (purple), and d) the system exposed to medium speed airflow with a whisker in contact.

3.6 Discussion and Future Work

Here we demonstrated how a whisker variant of the GelSight sensor can help create larger whisker arrays and allow us to distinguish between various stimuli (contact, airflow, and inertial) by tracking the motion of both the flat, elastomer membrane, along with motion of the individual whiskers. A single camera was used to track an array of six whiskers along with the elastomer membrane, significantly decreasing the complexity and interface required for a whisker array. In addition, the WhiskSight used magnetic attachment for reconfiguration of the array as needed for specific applications. While our demonstrations were made using an array of six whiskers, the magnetic attachment makes it relatively straightforward to scale up to larger arrays. The magnetic attachment also presents a limitation on array spacing however; the minimum spacing between whiskers is determined by forces between the magnets. As the magnetic force increases, the attachment force to the elastomer membrane increases but the minimum distance between whiskers also increases due to interactions between the magnets. This work favors attachment force over larger arrays, but future work can determine more optimal magnet sizing.

In addition, if reconfigurability is not required, adhesives and other non-magnetic whisker attachments (e.g., [41]) could be used. Magnetic attachment also influences the choice of marker locations on the elastomer membrane; the benefits of markers in a regular grid pattern, random marker locations (as in digital image correlation, DIC), or markers spaced regularly around magnet locations are ideas to explore in future work.

Another key feature in the whisker array presented in this work was the use of a flat elastomer membrane. The ability to classify contact, airflow, and inertial stimuli emerges from our ability to track both the motion of individual whiskers and the motion of the elastomer membrane oriented parallel to the camera image plane. Domed and curved surfaces found in other sensors like the TacTip [62] and TacWhiskers [41] provide greater surface area visible by the camera. The parallel planes trade off surface area for consistent motion across the array. For example, constant airflow across the array along with similar whisker sizes will result in similar drag profiles and therefore similar motions in the image plane of the camera. In general, an elastomer membrane parallel to the image plane simplifies the math between motion of the elastomer membrane and motion in the camera image. Finally, because the elastomer membrane is not exposed to airflow, the whisker array can respond to airflow and inertial stimuli differently, simplifying classification of these two stimuli.

Finally, the presented whisker sensing system still has several avenues for improvement in future work. In this work, whiskers were characterized for accuracy in 3 DOF (ϕ, θ, and z-axis deflection), and conform to the expected performance of the system given the choice of camera and geometry. These degrees of freedom were assumed to be most important to determine whisker motion, but future iterations of the whisker system could validate this by tracking additional degrees of freedom by increasing the number of tracked markers on the whisker magnets (e.g., corners of square or rectangular magnets). In addition, current system performance is largely limited by choice of camera. Higher pixel counts per unit area could im-

prove the rotation and z-axis deflection resolutions. Higher frame rates could speed up the time to detect various stimuli. The whiskers themselves can also be modified; identical rigid whiskers were used in this implementation, but flexible and tapered whiskers could ultimately help identify contact location along each whisker [40]. Finally, adding actuation through pneumatics or some other method can provide additional information about contacts, especially given the ease of distinguishing contact from the motion of the whisking system. Overall, the ability to detect and classify various stimuli like airflow, inertia and touch opens possibilities for future robotic applications of the system as well as for physical models of various biological whisking systems.

3.7 ACKNOWLEDGMENT

This work began as a project for the Tactile Sensing and Haptics course in the Robotics Institute at Carnegie Mellon. The authors would like to thank the course TA, Arpit Agarwal, for the assistance with research progress.

Chapter 4

Asymmetric Whisker for Improved Flow Sensing

Paper:

Kent, T. A., Thomas, L., & Bergbreiter, S. Using Asymmetric Whisker Cross Sections to Enhance Wind Sensing on Drones ***(In Preparation)***

Author Contributions:

TK designed the sensor, designed, automated, and performed all benchtop tests, developed the code/ algorithms to interpret sensor signals, and performed all data analysis after the test. LT designed the system to attach sensors to the drone, controlled the drone during experimental testing, developed the code to connect the whisker sensors to Bluetooth, and guided the drone testing for accurate data capture. LT and TK worked together to design the experiments performed on the drone. SB guided the research. All edited the manuscripts and figures.

Abstract

One way to decrease the gap between natural aerial fliers and quadrotor robots is to improve the quadrotor's perception. Here, the perception of whisker-inspired sensors is improved by modifying them so they are asymmetrically sensitive to airflow from

different headings; adding asymmetry makes the engineered sensors more similar to the biological mechanosensors that inspired them. The critical design aspect that yields the perception improvement is an offset between the asymmetric whiskers. This offset requires the side of maximum sensitivity for one whisker to occur at the same flow heading as the minimum sensitivity for a second whisker. The relative strengths of the signals from the two whiskers provide an extra piece of information for flow heading estimation. For a whisker whose asymmetric cross section can be described as triangular, the optimal offset is 60° and yields a 19% improvement in flow heading localization over two symmetric whiskers. The extra information from asymmetric offset cross whiskers means the flow heading can be predicted within 30° with 50% fewer data points. Finally, a pair of triangle cross-section asymmetric whiskers have enough information to quantify the likelihood of wind flow during drone motion in real-time, a valuable metric for a drone maneuvering in the wind.

4.1 Introduction

Research into quadrotor control is advancing towards grasping [76, 77], perching [77–79], and autonomous environmental monitoring tasks [80–82]. Some of the most ambitious control tasks have included picking up an object while moving [76], manipulating a tethered payload, and simulating a landing in heavy wind [83]. During these demonstrations, experimental conditions are constrained so that the data from the sensors can be interpreted correctly. However, for real-world applications, the sensor fusion algorithms must differentiate between more stimuli. For example, the accelerations from a moving payload [84], forces from external contact [84], quadrotor motion [85] and wind [86] can all generate similar IMU signals. Adding flow sensors, which are direct measures of the quadrotor's velocity with respect to the surrounding airflow, can simplify the differentiation of causal forces to IMU signals, resulting in improved flight control and state estimation [37, 87, 88].

Specialized flow sensors are much more common in biological flight than in quadrotor research [89]. Flow sensor hairs in bats [3, 90] and avian feathers de-

tect the flow indicative of stall [91]. Tiny hairs on mosquitos are believed to be the reason these animals can avoid surfaces they can not see during flight[92]. Similar tiny hairs on a locust's head allow them to reorient into the wind [93]. The locust can quickly respond to gusts of wind, which is believed to be facilitated by an array of individual hairs, each sensitive to specific wind flow direction signals [93].

The biological benefit of flow sensors has motivated numerous hair and whisker-inspired sensors on aerial vehicles [34, 35, 60, 89]. These hair sensors have improved control through quadrotor state estimation during flight [36] and during simulations of landing in high wind [83]. The hair-inspired sensors have also been used to quantify the flow or stabilization of a hovering drone in wind flow [36, 94–98]. The drag elements in these whisker-inspired flow sensors typically have symmetric cross sections to enable flow sensing from all directions.

In this work, we consider how whisker-inspired flow sensors with asymmetric cross sections can improve our understanding of relative airflow on quadrotors (Fig. 4.1a). Towards that goal, we use whiskers with varied asymmetric cross sections to determine how this asymmetry influences both the accuracy and time required to accurately estimate flow. We evaluate five whisker cross sections ranging from full symmetry (circle) to severely asymmetric (chevron) (Fig. 4.1b). The asymmetric cross sections are more sensitive to flows from specific directions because of variations in the drag coefficient and cross sectional area depending on the flow heading.

We also explored how the use of multiple asymmetric whiskers might improve the accuracy of flow measurements. Specifically, we studied how sensing might improve when the asymmetry of one whisker is offset relative to a second whisker so that one whisker might be most sensitive when the other is least sensitive to flow. Finally, we showed how these asymmetric whisker pairs can aid in the disambiguation of multiple flow sources. A quadrotor might experience multiple flow sources when it is both moving through the air and experiencing a gust of wind. This is the first demonstration of its kind as previously, flow sensors have only been able to distinguish multiple flows in benchtop experiments [99]. Quickly identifying gusts

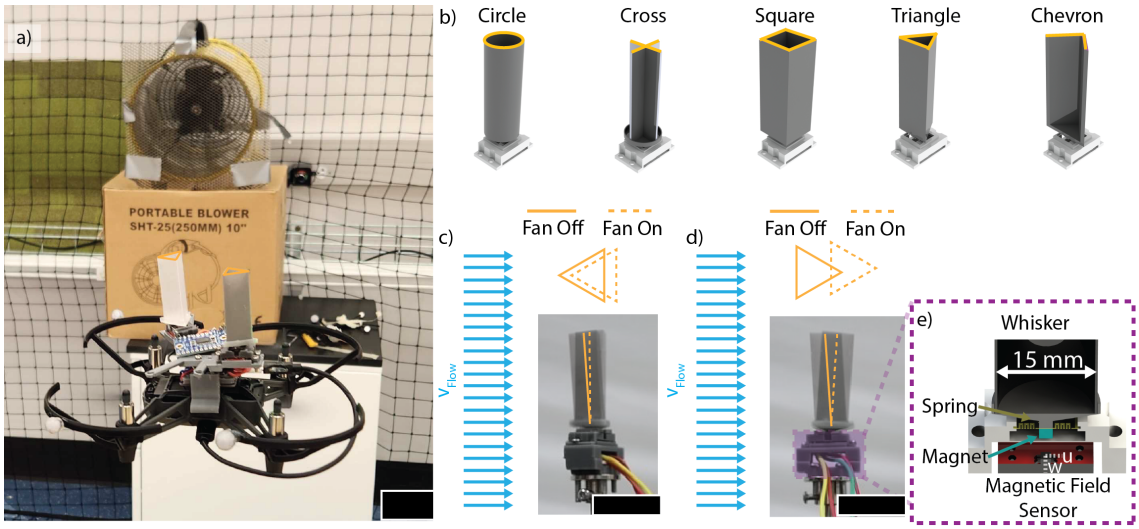

Figure 4.1: In this study, we explore how a whisker-inspired sensor with an asymmetric cross section, like the triangle whiskers shown in a) respond to flow from different headings. We measured a whisker array's ability to detect the speed and heading of flow both on the benchtop and on quadrotors. b) We tested five whisker cross sections and found that pairs of asymmetric whiskers offset to align the two whisker-inspired flow sensors' c) minimum sensitivity and d) maximum sensitivity led to the best performance. e) Each sensor measures flow by rotating a magnet relative to a Hall Effect sensor. By measuring motion in two axes orthogonal to the drag element (B_w and B_u) we can calculate both a flow magnitude $||B||_2$ and direction θ. Scale bars represent 30 mm.

of wind as well as the direction that this gust is coming from can be a significant advantage for quadrotor control in windy environments.

4.2 Results

4.2.1 Characterization of Asymmetric Whisker's Response to Flow

Whisker-inspired sensors, similar to their biological counterpart, have no sensing along their length; instead, they have a drag element (whisker) that transmits force to the fixed end at the whisker base. Airflow causes whisker-inspired sensors to deflect due to the drag force on the whisker body (Fig. 4.1c). The rotation at the base could be measured through vision signals [38], pressure signals [60], or, as in this work (Fig. 4.1e), magnetic field signals measured by a Hall-effect sensor [35].

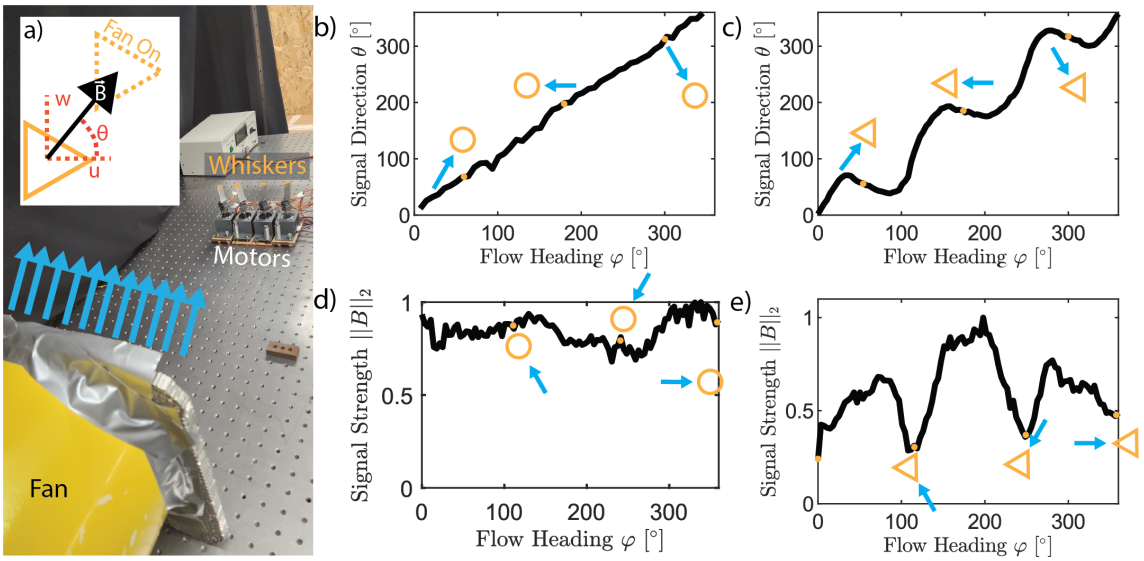

Figure 4.2: a) Wind from the fan applies a drag force to the whisker cross section causing the whisker to rotate about the springs. The whisker rotation causes a magnetic field change which is represented by vector $\overrightarrow{B}$. The motor's rotate each whisker in the airflow so we can record the effect of different flow headings, φ on $\overrightarrow{B}$. The direction of the force is calculated from the sensor signals as θ (eqn 4.1). The total drag force on the sensor is proportional to $||B||_2$ calculated from equation 4.2. Each cross section has its own B vs φ and θ vs φ curve. The curves for a symmetric whisker (circle) (b,d) and an asymmetric whisker (triangle) (c,e) are shown here.

Previous whisker-inspired sensors on quadrotors have used a circle [99] or a cross-shaped cross section for their whisker body (Fig. 4.1b) [35, 36] and assumed minimal asymmetry. Symmetric whiskers simplify the assumptions used to solve for the heading and strength of flow. For example, the flow direction signal, θ (the arctan of the magnetic field components) (eqn. 4.1, Fig. 4.2a), of a circle under a single flow is a good approximation for the flow heading φ (Fig. 4.2b).

$$\theta_n = \arctan \frac{B_w}{B_u} \tag{4.1}$$

However, due to manufacturing tolerances and assemblies, no sensor is truly symmetric. The circle whisker is symmetric in theory, but generally needs to be calibrated to account for manufacturing imperfections [99]. Without calibration, the signal strength can be stronger than expected along certain axes (Fig. 4.2 d).

For the cross, previous work found that flow on the cross vertex had noticeably stronger magnetic field (B) signals than flow on the edge [36] (Fig. B.2 d). In this work, we investigate the advantage of considering whisker sensor asymmetries rather than trying to mitigate them.

Asymmetric Whisker Characterization

Asymmetric signal strength response dependent on the direction of the flow is not unique to the cross whisker [100]. Airflow on the triangle whisker vertex will produce a signal 4x smaller than that same airflow applied on the triangle's flat side (Fig. 4.2 e, Fig. 4.1 c,d). The strength of the whisker signal, $||B||_2$, is proportional to the drag force (eq. 4.3) on the whisker. Therefore, if the drag coefficients (C_D) and cross-sectional areas (A) vary according to the flow direction (φ), so will the strength of the asymmetric whisker signal $||B||_2$.

$$||B_n||_2 = \sqrt{B_u^2 + B_w^2} \tag{4.2}$$

$$F_{Drag} = \frac{1}{2}\rho v^2 C_D A \tag{4.3}$$

The effect of asymmetry on signal strength is visualized in Fig. 4.2 where d represents the signal strength of a symmetric whisker and e an asymmetric whisker as they rotate in our flow field. Due to its asymmetry, the variation in the triangle curve is more significant and periodic than that in the circle curve. It is noteworthy that there are three minima on the curve in in Fig. 4.2e corresponding to flow incident on the triangles vertices.

The effect of an asymmetric whisker shape is also seen in the signal direction (θ) curve. Compared to the linear relationship (y = x) between θ and φ shown by the circle, a triangle demonstrates considerable non-linearity (Fig. 4.2 b,c). The authors expect this because the normal force due to wind has a proportionally larger effect on the whisker displacement than the sheer force from the wind. This hypothesis is supported by the fact that the semi-horizontal portion of the triangle

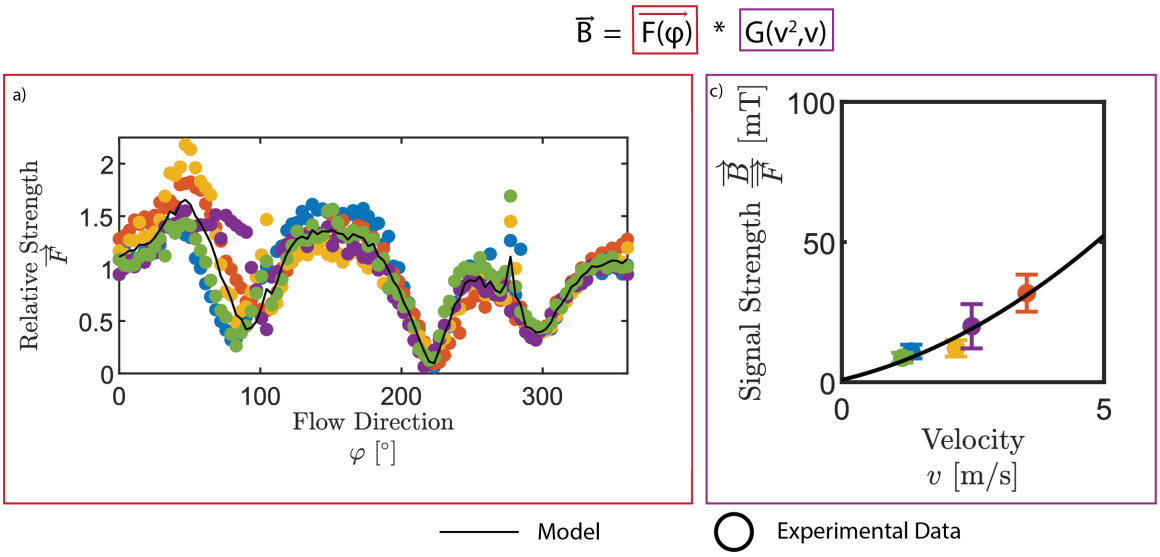

Figure 4.3: For a triangle whisker we can model the expected magnetic field signal as a combination of the flow heading affect curve, $\overrightarrow{F}$, and the velocity affect, $G(v^2, v)$ curve. The data collected from flows at 101 heading angles at five velocities is plotted with the scattered colored points representing the data at a given velocity, and the model curve is shown in black. On the $G(v^2, v)$ curve (right), the 101 data points are represented by their mean and standard deviation.

curve $\theta(\varphi)$ is centered around the flow on the flat edge of the triangle. The graphs shown in Fig. 4.2 represent the results of two sensors only for visual clarity, the curves for each whisker discussed in this work can be found in Figure B.1.

The curve $\theta(\varphi)$ is also used here to quantify the asymmetry of each whisker. The asymmetric measure is the root mean square error between a linear φ vs φ curve and the φ vs. θ curve; for the circle whisker and triangle whisker shown in figure (Fig. 4.2 b,c), the sensors asymmetry are 11.4° and 28.6°, respectively. The average asymmetry value for each whisker cross-section can be found in Table B.1, and a visualization of the amount of asymmetry is the order of the whiskers in Figure 4.1 b.

Modeling

For flows within a similar Reynolds range, we expect that we can model each sensor as a response to the input flow vector. The input flow vector is defined by its velocity and heading. Our sensor response is similarly split, so the expected sensor signal is defined by two curves: 1. $\overrightarrow{F(\varphi)}$ that represents the effect of heading on the B_u and

B_w curves, and 2. $G(v, v^2)$ which represents the effect of the flow velocity (Fig. 4.3) on the overall signal strength (B). We found that small variations in manufacturing led to measurable changes in the sensor profile (Fig. B.1, Fig. B.2), and therefore, we decided to have a separate calibration curve for each sensor.

$$\overrightarrow{B} = \overrightarrow{F} * G(v^2, v) \tag{4.4}$$

Model Performance

The fit between the model and the experimental data for one triangle whisker can be seen in figure 4.3. The $\overrightarrow{F(\varphi)}$, generated from five trials of different velocity flows, can predict variations in signal strength caused by variations in the flow heading with an accuracy of 3.42 mT RMSE. The curve $G(v, v^2)$ predicts variations in the strength of B due to the flow velocity with an accuracy of yy RMSE. When the two curves are multiplied together (eqn. 4.4) they represent the expected magnetic field vector based on an input flow vector. Table 4.1 represents the average Root Mean Square Error of three whiskers per cross section between the expected magnetic field vector from the known input flow and the recorded magnetic field vector from experimental results.

Table 4.1: RMSE of the Model Predicting Sensor Signals

	Circle	Cross	Square	Triangle	Chevron
$\overrightarrow{B}$	3.8 mT	3.9 mT	3.1 mT	2.6 mT	3.0 mT

Visualization of the curve fits for the other asymmetric whisker sensors can be found in figure B.2.

4.2.2 Estimating Airflow from Sensor Signals

We quantify the benefits of each sensor shape by their ability to accurately predict the incoming flow velocity (v) and heading (φ). Here we compare how the whisker

shape, pairs vs single whiskers and different algorithms affect the accuracy of the incoming flow prediction. In this work, all algorithms predict flow heading before velocity to quantify airflow speed accurately.

Single Whisker Flow Estimation

To predict the flow heading for a single whisker, we input the sensed flow direction, θ, into the interpolated $\varphi(\theta)$ curve (Fig. 4.2 b,c). After we have a flow heading estimate ($\hat{\varphi}$), we use $B' = \frac{\vec{B}}{F(\hat{\varphi})}$ to estimate the velocity. The Root Mean Square Error for a single whisker to estimate flow can be seen in Table 4.2. Unsurprisingly, if only one whisker is used, a symmetric whisker is the best choice for measuring flow between 0° and 360°. Given that the triangle and chevron θ vs. φ curves were not bijective (Fig. 4.2c, Fig. B.1e), it is unsurprising that larger asymmetry led to a poorer performance with the θ vs. φ curve method.

Table 4.2: RMSE for Individual Whiskers Predicting Flow

	Circle	Cross	Square	Triangle	Chevron
v	$0.40\,\mathrm{m\,s^{-1}}$	$0.40\,\mathrm{m\,s^{-1}}$	$0.67\,\mathrm{m\,s^{-1}}$	$0.58\,\mathrm{m\,s^{-1}}$	$0.45\,\mathrm{m\,s^{-1}}$
φ	8.2 °	8.3 °	20.7 °	37.8 °	31.7°

Considering the curve's shape yields better performance than estimating flow using equation 4.1. Using equation 4.1 is the method applied to previous work [35, 99, 100]. The asymmetric metric (Table B.1) is also the RMSE that would be found if we used equation 4.1 to estimate flow heading.

Whisker Arrays

Single whisker/ hair sensors do not exist in nature. Instead some animals have as few as 9 [5] whiskers but others have over 275 whiskers [6]. Flow-sensing hairs in insects allow animals to respond quickly to changes in airflow. It is theorized that these hair sensors have evolved to reduce the complexity of interpretation through mechanical filtering. For example, the locust has differently oriented hairs, which

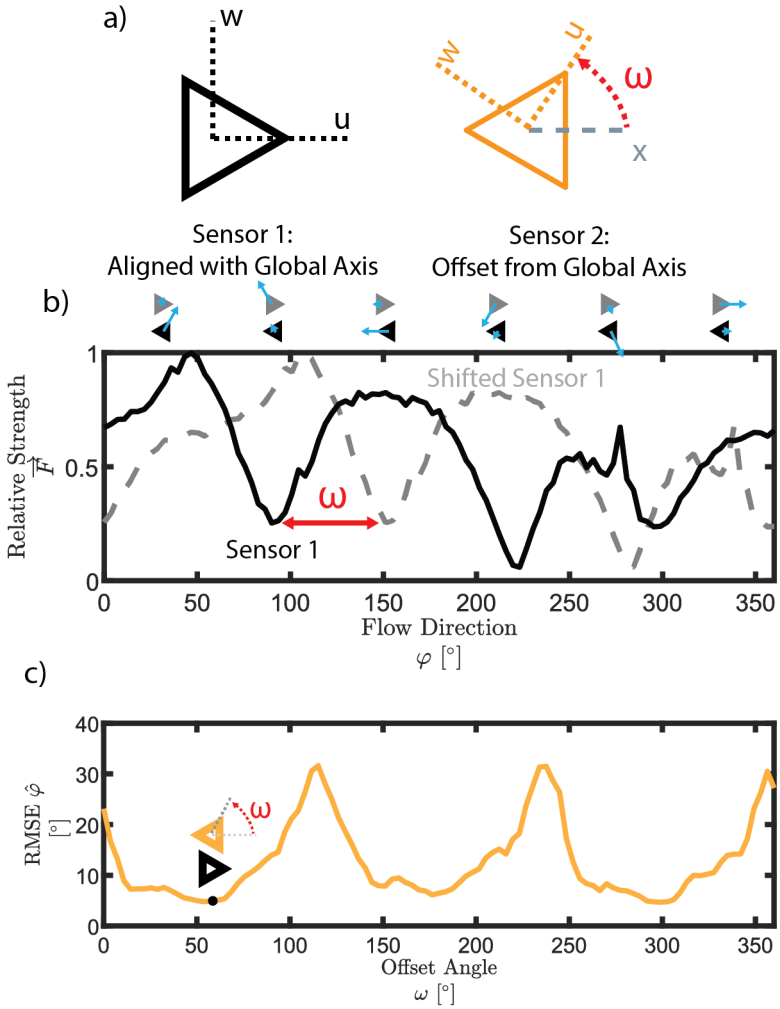

Figure 4.4: a) We investigate the effect of changing the relative orientation of two whiskers in a whisker array by rotating the second whisker by an offset, ω. b) This rotation makes it so times when one whisker has a strong signal strength can exist at the same time as a second sensor with weaker signal strength. For diagrammatic purposes this is visualized with the same signal strength curve. c) The amount of offset has a marked affect on how accurately algorithm 2 can predict the flow heading, φ.

are mainly sensitive to flow headings within a 20° span [101]. One benefit of this mechanical selectivity could be that it elucidates the causal heading of flow.

Here, we take inspiration from the arrays of hairs used by locusts and consider how paired whiskers with different relative orientations can improve flow heading estimation. We define the offset in orientation between two whiskers as ω, visualized in Fig. 4.4 a. The relative rotation shifts the offset whisker's signal curve so two whiskers receiving the same flow will generally have different sensor measurements (Fig. 4.4 b). Here we consider how different offset angles ω affect the two algorithms

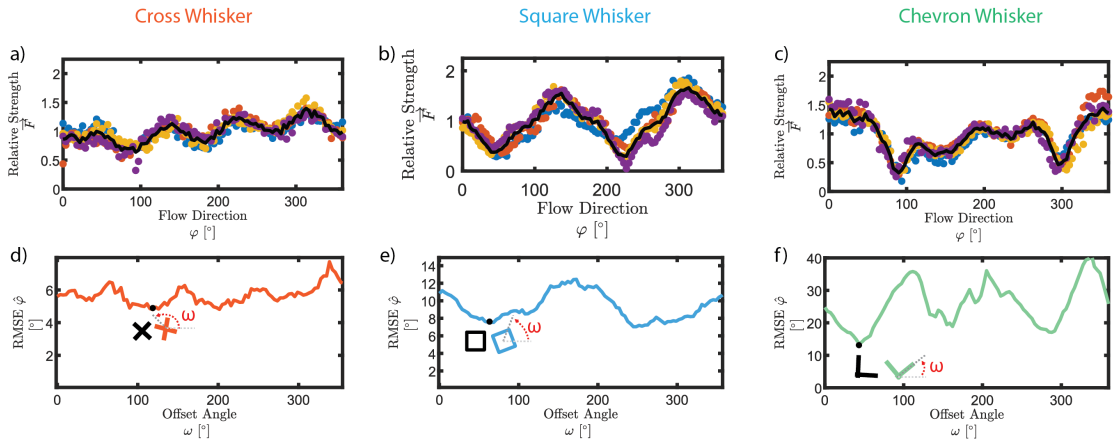

Figure 4.5: Top Row: The model (black line) and experimental data (scatter points for each velocity) of the effect of the whisker's cross strength on signal strength for airflow from various headings. φ. Bottom row: The variation in these curves means that each whisker has different ideal offsets between the two whisker sensors, ω in order to accurately estimate the flow heading. Here we show the asymmetry with paired data from the same whisker to highlight the ideal offset.

we use to estimate flow heading. Algorithm 1 aligns with the flow heading prediction of a single whisker; each sensor estimates flow heading, φ, from the φ vs θ curve and the estimate is the average of the two values. In the second method, we consider the relative strengths of each component of each whisker's signal ($B_{u,1}$, $B_{w,1}$, $B_{u,2}$, $B_{w,2}$). The algorithm works to answer the question: What flow heading most likely caused all four signals sensed by the 2-whisker array?

Algorithm 1: Estimating φ using the θ vs φ curve The accuracies in Table 4.3 represent the best performance of algorithm 1 for a pair of whiskers with the same cross section. We measure performance as the root mean square error of the φ estimate when averaging the $\hat{\varphi}$ from two sensors at their best offset. All of the predictions were improved by introducing a second whisker to help reduce the effect of noise. But, by offsetting the whiskers, we see a larger improvement in sensor performance for the triangle and chevron, which have non-bijective θ vs φ curves. The best offset orients the whiskers so the non-bijective point does not occur for both whiskers simultaneously. The increased accuracy in predicting φ also results in better velocity predictions using the calibration curve, as the method to solve the velocity does not change from a single whisker, but the enhanced $\hat{\varphi}$ improves the

accuracy of $\hat{v}$.

Table 4.3: RMSE For Paired Whiskers Predicting Flow using the θ vs φ Method

	Circle	Cross	Square	Triangle	Chevron
v	$0.33\,\mathrm{m\,s^{-1}}$	$0.27\,\mathrm{m\,s^{-1}}$	$0.32\,\mathrm{m\,s^{-1}}$	$0.38\,\mathrm{m\,s^{-1}}$	$0.33\,\mathrm{m\,s^{-1}}$
φ	5.4 °	5.6 °	13.0 °	20.1 °	26.7 °

Algorithm 2: Offset Method In the second algorithm, we compare the signals from two whiskers. When the offset creates differences in signal strength (Fig. 4.4 b), the relative strength of the two signal responses becomes an extra clue into the flow heading. For example, when two triangle sensors are offset by an angle of 60° as in figure 4.4, the sensor with flow incident on the vertex will have a signal strength approximately $0.25x$ (Fig. 4.1c) the signal strength of the sensor with flow on its flat side (Fig. 4.1d). In practice, we compare the strengths of B_u and B_w because the magnetic field vector components contain inherent direction information. By considering the strength and direction of two whiskers at once, our algorithm can considerably narrow the possible solution space.

The offset, allows us to achieve significant differences in the strength curve, $\frac{||B||_{1,Sensor1}}{||B||_{1,Sensor2}}$ (Fig. 4.4b). In Fig. 4.4 c, we visualize how different offsets between the two whiskers alter the root mean square error for estimating flow heading using our offset method. For the triangle whisker, there is a local minima (black dot on Fig. 4.4 c) when the offset is approximately 60° ±120°. This correlates to curves that align the vertex of one whisker and the flat side of another, aligning the maximum and minimum signal periodically.

This result holds with the results from the other asymmetric whiskers tested. For the asymmetric whisker cross sections, which similarly have local maxima and minima in their $\overrightarrow{F}$ curves (Fig. 4.5 a-c), the RMSE varies with the offset (Fig. 4.5 d-f). The cross has 4 local maxima, aligning with angles where the offsets between the two shapes would lead to symmetry, e.g.,0° ±90° $* k$, where k is an integer. Notably, for all whiskers but the circle, the ideal offset and algorithm 2 improves flow

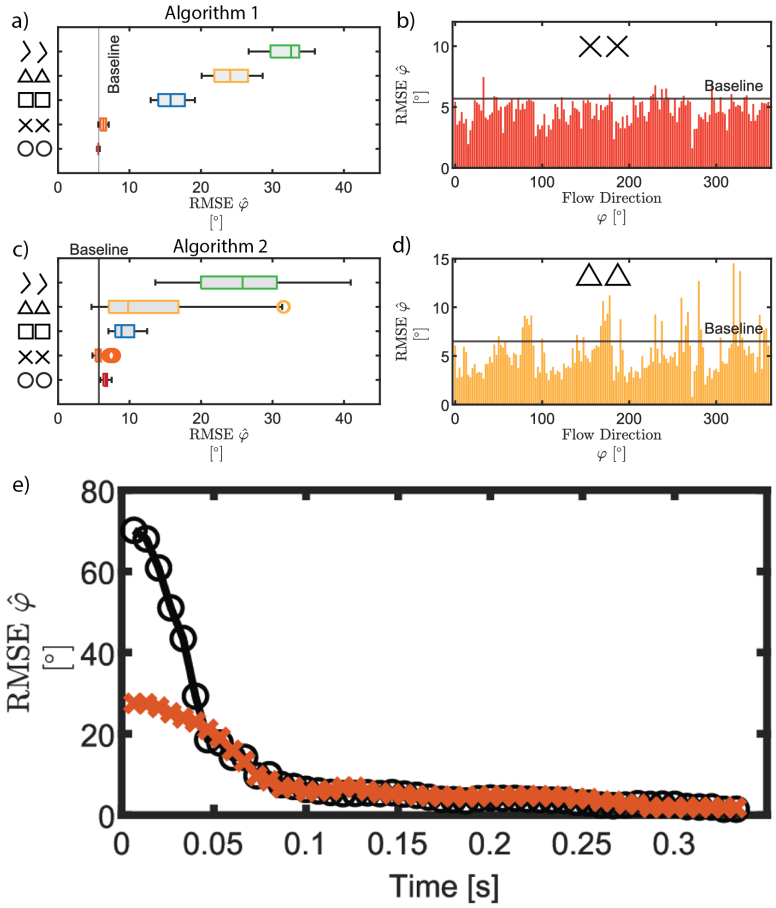

Figure 4.6: Box and Whiskers plots show the span of accuracies for different offsets for a) Algorithm 1 and c) Algorithm 2. The minimum represents the accuracy at the best offset. Two whiskers at the best offset may better sense flow from some flow headings than others. This is visualized in the bar chart showing accuracy over five trials of a b) cross whisker pair and d) a triangle whisker pair sensing flow from 101 flow headings. e) At the best offset, we calculate the effect of having more sensed data on flow heading accuracy. Each point on the graph represents an additional data point.

heading prediction over algorithm 1 at the optimal offset. Additionally, the cross, and triangle whiskers outperform the pair of symmetric circle whiskers, indicating the benefit of asymmetry in whisker shape. The baseline accuracy to improve past for flow heading is 5.7° which is the root mean square error of two circle whiskers with no offset estimating flow heading using algorithm 1.

The RMSE for the best pair of whiskers at their best offset from the experimental data is listed in Table 4.4.

Table 4.4: RMSE For Paired Whiskers Predicting Flow using the Offset Method

	Circle	Cross	Square	Triangle	Chevron
v	$0.28\,\mathrm{m\,s^{-1}}$	$0.22\,\mathrm{m\,s^{-1}}$	$0.29\,\mathrm{m\,s^{-1}}$	$0.31\,\mathrm{m\,s^{-1}}$	$0.23\,\mathrm{m\,s^{-1}}$
φ	5.9°	4.8°	7.0 °	4.6 °	13.6 °

4.2.3 Comparison of the Flow Estimation Methodologies

All paired whiskers have a lower root mean square error than their same-shaped single whiskers. However, the offset can significantly increase performance. In Fig. 4.6a the span of possible RMSE errors for algorithm 1 depending on the offset is represented by the box and whiskers plot. For the shapes with a non-bijective $\theta(\varphi)$ curve (e.g., the triangle and chevron curvse seen in Fig. B.1) the span of the RMSE is significantly higher, indicating a larger offset impact than for the one to one functions. The impact on the offset selection is even more dramatic for the non-bijective curves for algorithm 2. For algorithm 2, we show here 3 whisker shapes that show better flow heading detection at their ideal offset.

We expect that increasing the number of whiskers would improve the RMSE of the most asymmetric whisker relative to the RMSE of medium asymmetry whiskers. This is because we belive the most asymmetric whiskers still have large dead zones, angles where the sensor has trouble pinpointing the sensor angle. We believe more sensors could diminish these dead zones. For example, the triangle whisker in its ideal offset beats the baseline 83% of the time but struggles at specific flow headings(Fig. 4.6 d). The potential of a large number of whiskers is consistent with previous work on large arrays of 1D hair sensors, which show that considering the entire array leads to a more comprehensive signal than any single whisker could identify [89].

For both algorithms, increasing the accuracy in predicting the flow heading also translates to an increased accuracy in predicting the velocity using the calibration curve. The exception is the chevron curve, where velocity prediction increases despite medium performance in direction prediction. A possible explanation is that the dead zones of the chevron whiskers occur in places where the $\overrightarrow{F}$ curve is rela-

tively flat, meaning the strength used to solve for the velocity is correct even though the angle is not as accurate (fig.4.5c).

4.2.4 Temporal Accuracy

Thus far, we have calculated flow heading accuracy from the median B_w and B_u signal over one second (150 data points). Filtering the data through averages is important because the whisker oscillates about the force balance point, meaning that any given single signal is not likely to be that accurate. In figure 4.6e, we show how the extra information about the relative whisker strengths provides us with more accurate estimates using fewer data points. Because the whisker is oscillating approximatly around the modeled strength, the relative strength between two whiskers is often more indicative of flow than a direction signal at a single instant in time. The time on the x-axis represents the time it takes to collect 150 data points. Accuracy with fewer data is important for drone wind sensing as it can decrease the lag between stimuli and the drone response.

4.2.5 Whiskers on a Drone

The increased accuracy with lower samples is ideal when flow sensors move from benchtop to drone testing because of increased signal noise and the desire for accurate dynamic sensing. Therefore, better performance and a smaller averaging window are significant advantages on a drone.

A second issue for drone wind sensing in application environments is that there can be two flow sources relative to the drone: one caused by the drone's motion, which we call drag flow, and one caused by airflow, which we call wind. The forces from the two sources combine on a whisker to create one signal. For two symmetric whiskers the combined forces would combine on the whiskers the same way leading to both whiskers signals to indicate a single flow source vector that would correlate to airspeed.

By contrast, on asymmetric whiskers, the magnitude of the effect of each flow

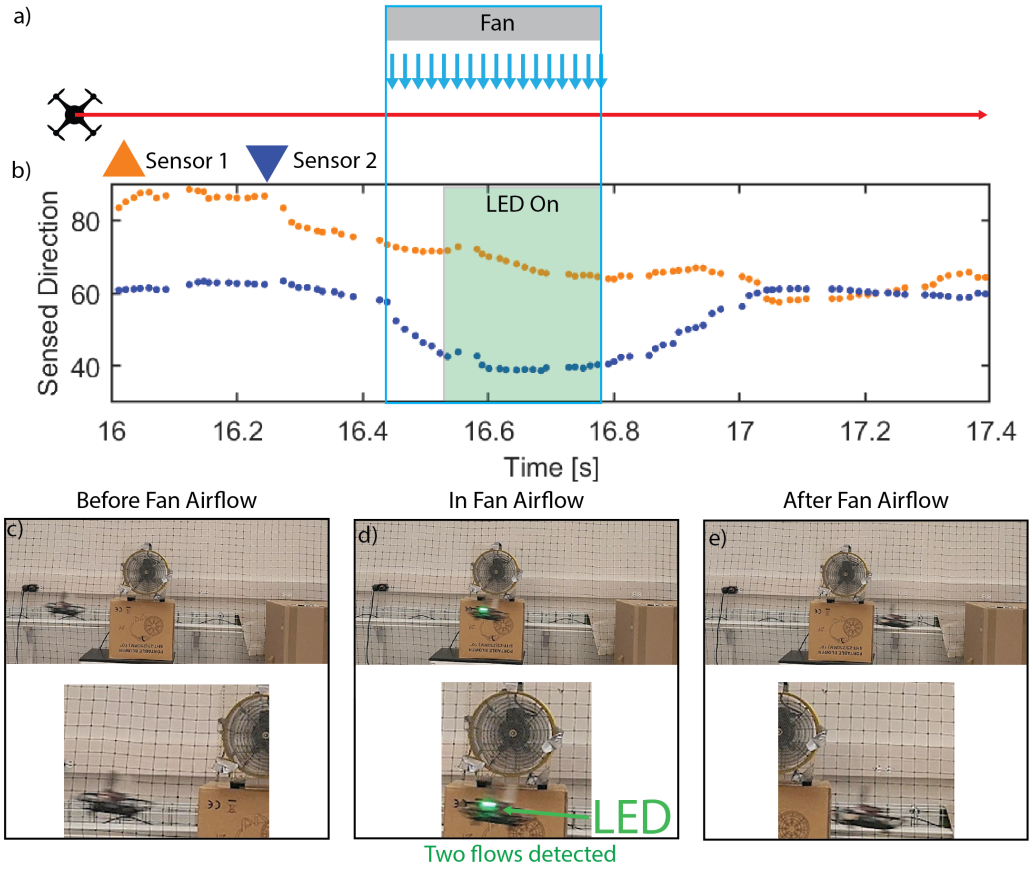

Figure 4.7: Both drag from motion and external wind flow will cause forces on our whisker-inspired sensors. As our quadrotor passes a box fan, the force of the external flow on the whisker depends on the orientation of the whisker relative to the heading. Here, we have two triangle whiskers offset by $\omega = 60°$ in the orientation shown in a. a) The whiskers travel across a room through the airflow. b) When the drone is at full speed but there is no wind (t=17 to 17.4) the two whisker sensors should predict the same flow heading. By contrast, we can identify two separate drag forces when we have two whisker signals with 1. strong signal response (not shown) and 2: two distinct flow heading predictions. c-e) We demonstrated the viability of these conditions by programming an LED into the sensor system, which lit when the two prior conditions were met. 12 demonstrations of this can be found in the Supplementary Videos.

source on a whisker depends on the individual flow headings. The different signal strengths correlate to different forces on the whisker, meaning the combined force from the two wind vectors yield two distinct whisker signal vectors.

This idea was tested with two triangle whiskers offset by $\omega = 60°$ on our micro-drone, subject to single- and double-flow sources (Fig. 4.7a). Under single flow, the signal strength varied, but both whisker's predicted a flow source with the same flow heading (Fig. 4.7b). However, when a second flow source is introduced, the

sensed angle of flow depends on the whisker's cross-section perpendicular to the flow heading. A whisker with its flat side (the strong signal) oriented towards the wind source had a strong reaction to the wind, while a whisker with its vertex (the weak signal) oriented towards the wind source had a stronger response to the drag flow as the wind effect was smaller. The result is whiskers which sensed angle of flow θ is distinct. In the test we ran the angle between the two flows was approximately 90° and the difference between the sensed angles was about 30°.

The experiments where we quantified dual flow were repeated this time using an LED to indicate times when both whiskers detected air flow but the gaps between the sensed angles were substantial (Fig. 4.7c-e). These conditions indicated two flow sources. Consistently over four orientations of the drone and several trials, we saw the LED turn on in front of the fan and turn off after leaving the fan flow (Supplementary Video 3). Still images from one trial are shown in Fig. 4.7. This demonstrates a sensing methodology to identify strong wind during flight. This distinction was accomplished with only two whisker sensors on a relatively lightweight (80 g) drone. We expect that more whiskers and a more substantial drone could expand the ability of these asymmetric whisker arrays even further.

4.3 Conclusion

In this paper, we have shown that strategically orienting a pair of asymmetric whisker sensors can mechanically elucidate the causal direction of flow, simplifying signal interpretation. Critical to the asymmetric whiskers' success was the amount of offset between the whisker sensors; offsets which maximized the difference between the two signal strengths performed best. We found that we needed to collect fewer data points to improve sensor accuracy below a set threshold using a pair of asymmetric whiskers than a pair of symmetric circle whiskers. The best asymmetric whisker pair improved the prediction of velocity and flow heading by 62 % and 36 %, respectively over a pair of sensors with circular cross-sections.

A second major benefit of using whiskers which are asymmetrically sensitive to

flow from different headings is the ability to identify when more than one flow source is present. As long as the flow sources interact on different profiles of the whisker cross section their forces will combine differently. A major limitation of this is they will not work well if the two flows headings are close to an angle of symmetry (for a triangle this would be 120°) because the forces would combine in the same way. The authors want to caution, this is only viable when one of the airflow sources is caused by self motion, flow mixing is a very real concern for two external flow sources. Interpreting flow accurately and quickly is an asset to quadcopters looking to incorporate external wind and drag into their control algorithm. We expect there are whisker cross sections which will improve our results even further. Sparser and clearer signals will lead to further improvements for quadcopters hoping to behave autonomously and semi-autonomously outdoors.

In this work we explore asymmetric sensitivity for five asymmetric shapes. Importantly, the authors don't believe they have found the best asymmetric shapes to apply this methodology; future work could explore a large optimization space for the asymmetric cross-section. We expect that these results will be further improved with new designs for asymmetric whiskers. This work also explores two relatively large whiskers for asymmetric flow sensing, future applications can take this work further with larger arrays of smaller whiskers.

4.4 Experimental Section

4.4.1 Whisker Manufacturing

This work studies how an asymmetric whisker cross-section affects a quadrotor's ability to estimate and differentiate flow. We tested five cross sections (Figure 4.1 b). Each whisker is printed using a Form Labs 3D printer. The cross and cheveron whiskers have a wall thickness of 2 mm and circle, square and traiangle whiskers have 0.4 mm walls but are internally hollow. Each shape takes up maximally a 15 mm x 15 mm square.

Outside of the changes to the drag element, the sensing mechanism is the same as [35] (Figure 4.2 b-e). When the whisker experiences drag force from wind, it rotates about the center of the rotation of the laser cut steel spring (photolaser U4, LPKF cutting 0.1 mm spring steel) it is glued to. The magnet, (2 mm^3 magnet C0020, Supermagnetman) glued on the opposite side of the spring rotates an equal magnitude in the opposite direction. This rotation is detected by the Hall Effect Sensor (TLE493-W2B6 A0, Infineon) kept 2 mm away from the center of rotation by the 3D printed housing. When more than one whisker is considered, a multiplexer (TCA9548A 1-to-8 I2C Multiplexer) gives each sensor a unique address to be read by the Micro Controller boards (Arduino Uno for bench top, Seeed Studio BLE for drone cage).

4.4.2 Data Processing

In this work, we detect air flow using the same sensing modality as whisker-inspired flow sensors from previous work [35, 99]. The raw signals from these sensors are magnetic field component vectors B_u and B_w. The signals can be converted into the component vectors into a signal direction (θ) and a signal strength ($||B||_2$) described by equations 4.1, 4.2.

Notably, the whisker sensor does not rotate to a fixed rotation, it oscillates in the wind around a rotation angle which balances the drag force and spring force [35] (Supplementary Video 1). To find this balance point, the directional magnetic field signals (B_u and B_w) from the sensor are put through an averaging filter with a window of five, which will remove up to one value if it's an outlier. The outlier removal is rarely triggered but remains in the code to catch data due to a momentary electrical glitch. The filtered signals are then evaluated using equations 4.1 and 4.2. θ_n is the angle of the direction of rotation of the whisker and $||B_n||$ is a measure of the magnitude of rotation. On a circular whisker θ_n would be a good representation of φ-ω and $||B_n||$ would be proportional to $m * v^2$ in all directions [100].

4.4.3 Experimental Design

Bench Top

The test setups are improved over previous work [99], allowing us to get a more precise calibration curve of the whiskers 0° to 359° response under single speed flow (Fig. 4.2a). A fan (Vevor Utility Blower Fan 10" diameter) was used to supply wind through an MRP Aiflow Straitner (12" x 12" 0.25" honeycomb cell) to the experimental test. The velocity of the fan was controlled by a BN-Link Exhaust Fan Speed Controller. The airflow speed was measured by an anemometer (4330, Thomas Scientific). Four sensors at a time where, each placed on its own Nema 17 stepper motor, which was controlled by an Arduino Uno to turn in 3.6° steps. The whiskers are 35 mm apart. This separation allows us to test the whisker's response to flow without a strong likelihood that the airflow hitting one whisker affects the signal on another, such as what happens in flow shadowing [99].

A video of our data collection can be seen in Supplementary Video 2. The four whiskers are subjected to five trials at five airflow speeds. The speed that reaches each of the whiskers can vary as much as 10% so we use the anemometer readings in front of each whisker after a test and take the average of the four speeds. The motors control the whiskers' rotation, and sensor signals are collected every 3.6°. The signals are collected 20s after the end of the rotation to prevent any inertial effects. 150 data points are collected for each whisker, angle and flow, which equals 1 s of data. The experimental data likely only holds for flows at similar reynolds numbers, here a value between 1000 and 6000 with most flows in the transition zone. If one would like sensors for flows outside the range tested here the sensor needs to be redisigned so the flows can be detected/ don't break the sensor, which requires recalibration anyway.

After the data is collected an algorithm shifts the data to minimize the asymmetry score of the sensor. In other words to minimize the distance between the motor angles and θ values. This shifting will bring the curve back to the origin if the test was accidently started with the sensor at 1.6° instead of 0°.

Drone Cage

Quadrotor tests integrated the asymmetric triangle sensors with the DJI Tello quadrotor. The quadrotor flew in a 10 m x 10 m indoor motion capture arena. The quadrotor was controlled via hand-held control that ran over wifi.

The whiskers were mounted via an assembly of 3D printed parts. The Seeed Studio BLE Sense board collects data from the multiplexer. The data from the sensor(s) and the board's accelerometer is then saved on an SD Card using a MicroSD card breakout board. Two experiments were run.

1. The drone flew along its +x axis reaching a maximum speed of approximately $1.2\,\mathrm{m\,s^{-1}}$ in front of the same box fan from experimental data before. The drone maintained its speed until it reached the opposite side of the drone cage then slowed to a stop. Signals to begin and end data collection was sent over Bluetooth Low Energy. Signals were collected every 60 Hz. The fan airflow was applied across the drones +y axis.

2. The same test was repeated with the drone flying along its (+x,-x,+y,-y) axes over separate trials. The airflow source was always at 90° from the direction of travel. These angles where chosen because they don't induce flow shadowing [99] an issue for arrays of whiskers on drones. In this test no data was saved to the SD card. Instead an LED was turned on when the conditions of Dual Flow were met. Without saving data the drone could sample the two whiskers at greater than 130 Hz. The x and y data from the drone was filltered twice with a filter window of 10 data points. The conditions for dual flow are:

   (a) Both whiskers with a signal strength above a threshold (15 mT) indicating both whiskers are sensing an airflow signal.

   (b) $|\theta_1\text{-}(\theta_2 - \omega)| > 30°$

4.4.4 Algorithms

Data Driven Model

We found the underlying function for the model by collecting each whisker's B_u and B_w response to five trials of velocity flows with $\varphi - \omega \in \{0, 360\}$. Each component of the signal response vector $\overrightarrow{B}$ is then normalzed by the median signal strength ($||B||_2$, eqn 4.2) for that one trials velocity. By averaging $\frac{\overrightarrow{B}}{med(B_2)}$ over the five velocity trials we get a curve that represents $\overrightarrow{F}$ for each sensor. We then use $\overrightarrow{F}$ curve to get the average $\frac{\overrightarrow{B}}{\overrightarrow{F}}$ value for each velocity tested as shown in Fig. 4.3b. For each sensor, the least squares method is used to find the constants C_1 , C_2 and C_3 in the equation $\frac{\overrightarrow{B}}{\overrightarrow{F}} = C_1 * v^2 + C_2 * v + C_3$. In addition to the averages from the experimental data a sixth point is added at the origin as part of the fit. By combining the F and G curves fit from the experimental data we can predict the expected magnetic field response given a flow of known heading (φ) and velocity (v) as long as we know the sensors offset (ω) from the global cordinate system.

$$B(\varphi - \omega) = \overrightarrow{F(\varphi - \omega)} G(v^2, v) \tag{4.5}$$

Single Flow Analysis

Two different algorithms are compared for their performance to predict the flow heading φ. The two algorithms are named the Theta Method, the Offset Method.

Theta Method: This method modified the current practice for whisker-inspired sensors [35, 36, 99, 100] to work well on asymmetric whiskers, which do not have linear φ vs θ curves (Fig. 4.2c). From the $\overrightarrow{F}$ curve we can calculate expected sensor signals (θ) for each flow heading, (φ). When estimating $\hat{\varphi}$ we use this calibrated curve to indicate what $\hat{\varphi}$ most likely caused the θ signal. When considering two whiskers, with the second whisker at an offset, the offset is a known variable that can be subtracted before averaging the two guesses.

We use this method, with no offset for the circular whiskers to generate the baseline as it is most similar to prior work. A mathmatical representation of this

algorithm is shown in algorithm 1.

Algorithm 1 Theta Method: Estimating φ using a φ vs θ curve

$\omega \leftarrow$ known offset(s)
$n \leftarrow$ number of whiskers
$F_u \leftarrow$ known response of the whisker based on φ
$F_v \leftarrow$ known response of the whisker based on φ
$\theta(\varphi)_n \leftarrow$ known curve of sensor n solved for from experimental data and equation 4.1 ▷ 360xn
for $\varphi \leftarrow 0$ to 359 **do**
    for $i \leftarrow 1$ to n **do**
        $\theta'\{\varphi, i\} = \arctan \frac{F'_{wn}}{F'_{vn}}$
    end for ▷ 360 x n
end for
for $i \leftarrow 1$ to n **do**
    B'_{ui} , $B'_{vi} \leftarrow$ sensors signals from a single φ ▷ 2x1
    $\theta_i = \arctan \frac{B'_{wi}}{B'_{vi}} - \omega_n$
    $E = \sum_{N=1}^{n} (\theta_i - \theta')^2$ ▷ 360
    $\hat{\varphi}_i = argmin\{E\}$
end for
$\hat{\varphi} = \sum_{i=1}^{n} \frac{\hat{\varphi}_i}{n}$

Offset Method: The offset method takes advantage of two whiskers offset at an angle, which will have different strength and directional responses because of different axis orientations, drag coefficients, and areas in the angle of the flow heading. By considering the two signal responses at once, we hope to estimate the signal more accurately than by taking the average of the two whiskers' predictions (Fig. 4.4).

To do this we need to know the expected relative signal strength between the two whiskers for every flow heading φ. Given a known offset we use the $\overrightarrow{F}$ curve to find to expected, B_u, B_w and signal strength of each whisker. We then normalize the sensor signals by the strongest absolute signal strength. The normalized B_u and B_w signals for $\varphi = 0 : 359$ are then stored in our Look Up array.

The cumulative root mean square error between the expected signals (360x4) and normalized experimental signals (1x4) gives us a likelihood that the four experimental sensor signals were caused by a given flow heading (360x1). In the offset method, we estimate $\hat{\varphi}$ as the point where there is the minimum error between the look up table and the experimental data.

A mathematical representation of this algorithm is shown in algorithm 1.

Algorithm 2 Estimating φ using the Offset Method

$\omega \leftarrow$ known offset(s)
$n \leftarrow$ number of whiskers
$F_u \leftarrow$ known response of the whisker based on φ
$F_v \leftarrow$ known response of the whisker based on φ
for $\varphi \leftarrow 0$ to 359 **do**
    for $i \leftarrow 1$ to n **do**
        $\theta'_i = \varphi + \omega_i$
    end for
    $F'\{\varphi, :\} = \frac{\{F_u(\theta'_1), F_v(\theta'_1) \ldots F_u(\theta'_n), F_v(\theta'_n)\}}{\max|\{F_u(\theta'_1), F_v(\theta'_1) \ldots F_u(\theta'_n), F_v(\theta'_n)\}|}$ ▷ 360 x 2n
end for
B'_{un} , $B'_{vn} \leftarrow$ norm sensors signals from a single φ
$E = \sum_{N=1}^{2n}(\{B'_{u1}, B'_{v1} \ldots B'_{un}, B'_{vn}\} - F')^2$ ▷ 360
$\hat{\varphi} = argmin\{E\}$

Evaluating the Algorithms

On the benchtop, for all but the temporal analysis, the 150 data points collected at one speed and flow direction are compressed to the average B_u and B_w value over the data points to calculate the $\hat{\varphi}$ and $\hat{v}$ estimates.

For the temporal analysis an averaging filter is applied to the B_u and B_w over the 150 data points so that when the filter is 1 it is just the raw data and when the filter is 150 B_u is the average which matches the previous benchtop test value. The estimates are then calculated for all of the 150 B_u and B_w values generated.

For all data the RMSE of φ and v represents five velocities and 101 angles of flow.

Chapter 5

Flow Shadowing a Method for Detecting Dual Flow

Paper:

Kent, T. A., & Bergbreiter, S. (2024) Kent, Teresa A., and Sarah Bergbreiter. "Flow Shadowing: A Method to Detect Multiple Flow Headings using an Array of Densely Packed Whisker-inspired Sensors." IEEE International Conference on Robotics and Automation (ICRA)

Author Contributions:

TK designed the sensor, developed the whisker array and all code/ algorithms, and performed all analyses. SB guided the research. All edited the manuscripts and figures.

Abstract

Understanding airflow around a drone is critical for performing advanced maneuvers while maintaining flight stability. Recent research has worked to understand this flow by employing 2D and 3D flow sensors to measure flow from a single source like wind or the drone's relative motion. Our current work advances flow detection by introducing a strategy to distinguish between two flow sources applied simultaneously

from different directions. By densely packing an array of flow sensors (or whiskers), we alter the path of airflow as it moves through the array. We have named this technique "flow shadowing" because we take advantage of the fact that a downstream whisker shadowed (or occluded) by an upstream whisker receives less incident flow. We show that this relationship is predictable for two whiskers based on the percent of occlusion. We then show that a 2x2 spatial array of whiskers responds asymmetrically when multiple flow sources from different headings are applied to the array. This asymmetry is direction-dependent, allowing us to predict the headings of flow from two different sources, like wind and a drone's relative motion.

5.1 Introduction

Direct measurement of airflow around a drone (e.g., the velocity and direction of flow) has led to several improvements in drone flight control [36, 37, 102]. Most drones experience at least two sources of airflow: 1) the relative motion of the drone and 2) environmental sources, such as wind. Direct measurement of drone velocity through airflow can provide real-time feedback and improved state estimation [35, 36, 103]. Measurement of environmental wind flow can allow a drone to incorporate drag forces into its motion and navigation [36, 87] and, importantly, improve stability [83, 104].

A measurement challenge arises when both airflow signals are present; the flow signal caused by drone motion cannot be easily distinguished from the flow signal caused by wind. No published sensor has been shown to distinguish and interpret flow from two sources simultaneously. This gap contrasts with the natural world, where animals interpret complex flow signals during flight or while swimming using arrays of whisker/hair sensors [3, 10, 105, 106]. For animals such as the harbor seal, an array of whiskers is critical to interpreting the vortices caused by prey while the seal is swimming. As a vortex passes the seal's upstream whiskers, the whiskers' shape amplifies the vortices that are then detected by the downstream whiskers [10].

Using the idea that the shape of an array can modify flow across an array, we

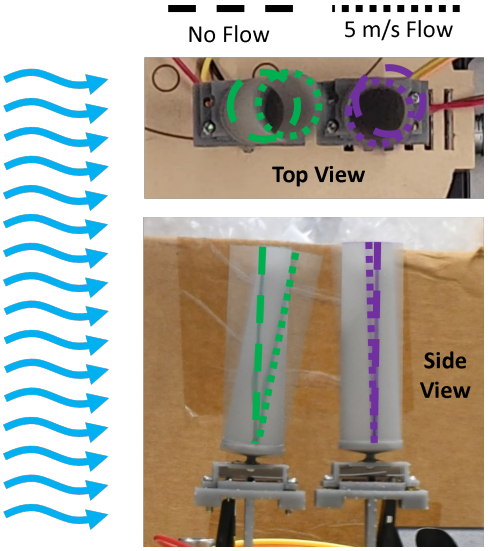

Figure 5.1: Top and side views of two whisker-inspired flow sensors demonstrating flow shadowing. The upstream whisker (green) rotates significantly in response to an incident flow. In contrast, the downstream whisker (purple) in the shadow of the upstream whisker oscillates around its original position.

engineered a sensing array with the novel ability to isolate the distinct headings of two separate flow sources. In our array, upstream whisker-inspired sensors can block or partially block the flow to downstream whiskers, a phenomenon we call "flow shadowing". In flow shadowing, the upstream whisker(s) receive the full effect of the airflow, but the downstream whisker(s) (which are in the front whisker's "shadow") only receive a portion of the flow (Fig. 5.1). The shadowing becomes multi-directional when a second flow source is introduced, increasing the asymmetry in signal response. Comparing the response of all whiskers in the array allows us to identify the origin heading of two simultaneous flows.

Our first experiment quantifies the flow shadowing phenomenon using a modified version of two previously developed sensors [35, 107] under partial and complete occlusion. We found a linear response between the percent of whisker shadowed and the magnitude of the comparative signal responses. The linear relationship exists in ideal conditions (wind tunnel) and imperfect flow (box fan). Importantly, we determined that reduced spacing between the two whiskers increased the magnitude of the flow shadowing phenomenon under imperfect flow. In our second experiment, we subjected a 2x2 array of whiskers to flow from one or two different sources, show-

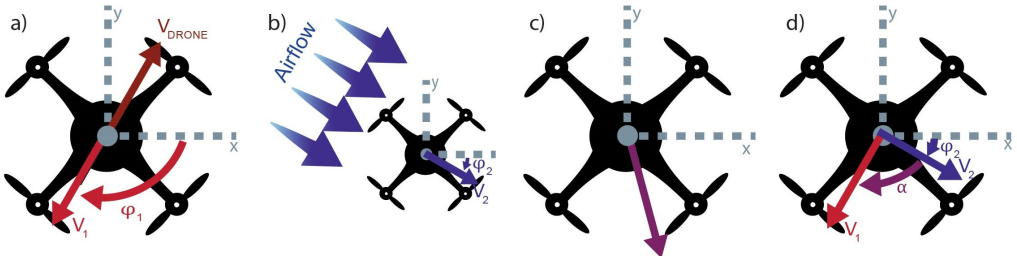

Figure 5.2: Diagram of nomenclature for two flow signals. a) Flow 1: A drone flying at velocity v_{Drone} with a flow sensor onboard measures a flow signal equal to but opposite the drone's velocity (v_1, φ_1). b) Flow 2: The environment in which a drone flies has wind. An onboard flow sensor will respond to the wind flow (v_2, φ_2). c) A flow sensor that responds to both flow types equally will measure a combined signal. d) α is a measure of the difference between the headings of the two flow stimuli (φ_1 or φ_2) which are estimated from an array of flow sensors.

ing that shadowing in multiple directions yields a predictable asymmetric response in an array. We use these asymmetric signals to estimate the flow headings under two conditions: 1) we know the heading of one of the flows, and 2) we have no prior information about the flows.

5.2 Related Work

5.2.1 Arrays of hair sensors in biology

Flow-sensing hairs are often critical to aerial flight, giving animals information about speed and stability. One study showed that when hairs were removed from bat wings, the bats altered their flight, performing more naturally stable maneuvers and flying faster [3]. Locusts also use hairs to detect flow and for flight stability. Airflow across locust hairs induces flight movements, which does not occur when their hairs are temporarily desensitized. Hair desensitization also prevents the locust from maintaining stable flight [105].

Most animals that use whiskers/hairs to sense flow use an array of hairs. Understanding the importance of the array neurologically is complex, so much of the prior research on arrays has focused on the array mechanics. Research shows flow-sensing hairs can work together to provide a complete picture of the flow. For example, each of the flow-sensing hairs on a locust responds most strongly to flow from a single

direction, but locusts are covered in hairs with different orientations, allowing them to better understand the flow environment [106]. Harbor seals also have whisker arrays. In harbor seals, the upstream whiskers maximize the vortex-induced vibrations caused by their prey to increase the sensing ability of the downstream whiskers [10].

5.2.2 Direct Flow Sensors

There is a long history of 1D flow sensing on commercial aircraft, but here we focus on 2D and 3D flow sensing as it is more relevant to drone flight. Four types of flow sensors have been used to capture both the direction and magnitude of airflows: anemometer arrays [96, 108–111], pitot tube pressure arrays [94, 112], hot wire arrays [37, 113–115], and whisker-inspired sensors [35]. The first three sensors (all but the whisker-inspired sensors) use an array of 1D sensors to obtain a 2D or 3D flow vector. Our work is based on the whisker-inspired sensor; the functionality of this sensor is described in the Methods section.

Previously published flow sensors have demonstrated the benefits of drone velocity sensing [35, 94, 96]. The authors compared the drone velocity estimated from flow sensors to the drone's velocity profile collected from motion tracking data [35, 94]. Good velocity estimation is important for state estimation and navigation tasks. Accurate velocity estimates are also essential for advanced maneuvers, where measurements can help predict lift and drag [103]. All prior demonstrations of velocity estimation via flow were performed in a drone cage with negligible wind.

Information about wind flow provides force information to a drone's flight controller. In [37] and [102], researchers incorporated the flow sensor signal into the drone control algorithm to maintain position stability in gusty flow. In [36], researchers combined flow sensor and IMU data to estimate the direction of an external gust while subtracting flow from motion. The same researchers later showed in simulation how the flow sensor could help a drone land in gusty conditions [83]. In all three papers, the gust represented a significantly larger magnitude flow than

any flow due to the drone's motion in contrast to the study presented in our current work.

5.2.3 Indirect Measures of Flow

While the sensors discussed in the prior section measure flow directly, drone velocity, wind [85], and drag [116] have also been measured through indirect measurements. The challenge, similar to direct flow measurements, is that another sensor type must be present to measure multiple flow sources [86]. Optical flow sensors estimate the velocity of a drone by tracking features on earth during the drone's flight [117, 118] provided the environment has sufficiently distinct features. Inertial measurement units (IMUs) have been used to both calculate drone velocity [119] and external wind [86]. Often, data from IMU sensors, GPS and optical flow [120, 121] are fused together to predict velocity, as each one is situationally imperfect at measuring velocity.

5.3 Methods

5.3.1 Nomenclature

The sensing array aims to define the origin of two flow sources of similar velocity (v). The headings of the two flows are labeled φ_1 and φ_2 relative to the drone. In experimental results, α, the smallest angle between the two flows is also calculated because differentiating two separate flows becomes more difficult as α gets smaller. We also expect that the relative magnitudes of the two flows, $\frac{v_1}{v_2}$, will also affect our ability to accurately distinguish multiple flow sources. These variables are depicted in Fig. 5.2.

5.3.2 Array Manufacturing

The design of the sensing system is the same as [52, 107] and is modeled using the same methods as [52, 107]. The only update is a change in fin shape from a cross

[52] to a 50 mm tall, 15 mm diameter hollow cylinder. The cylinder is expected to have a uniform drag response for various flow directions in 2D, which was not true for the cross shape [36].

A diagrammatic representation of the sensor design is in Fig. 5.3c. A 2 mm^3 magnet (C0020, Supermagnetman) is glued on the backside of a laser-cut spring (photolaser U4, LPKF) made from 0.1 mm steel. A hollow cylinder with a taper at the base is 3D printed using a Formlabs printer and attached to the spring opposite the magnet. As the flow hits the cylinder surface, the cylinder "whisker" rotates about its fixed point (the center of the spring) (Supplementary Video). The magnet also rotates through an equal and opposite angle. A Hall effect sensor (TLE493-W2B6 A0, Infineon) detects this rotation. The magnet and Hall effect sensor are kept at a constant separation by a 3D-printed housing.

The array of sensors (Fig. 5.3b) maintains a spacing, s, between whiskers of 35 mm unless explicitly specified otherwise. The spacing is maintained using laser cut and 3D-printed housings and secured with screws. Each sensor in the array is connected to an Arduino Uno through a multiplexer (TCA9548A 1-to-8 I2C Multiplexer) which can sample all four sensors in the array at over 100 Hz.

5.3.3 Data Processing

When flow hits a whisker, the whisker oscillates about a point where the spring forces and the drag forces are balanced [52] (Supplementary Video). The average rotation magnitude and direction are indicative of the velocity and direction of flow. These features of rotation are measured by changes in the magnetic field signal recorded by the 3 axes of the Hall effect sensor (B_{xn}, B_{yn} and B_{zn}). The Hall effect sensors' axes are aligned with the axis of the full array (Fig. 5.3a) and the numbers circled in Fig. 5.3b represent the whisker number in the array.

To counteract variability in the manufacturing process, each sensor is calibrated individually by applying a 5.5 $m\,s^{-1}$ flow parallel to the Hall effects sensor's +x, -x, +y, and -y axes in turn. These stored values can be used to normalize the response

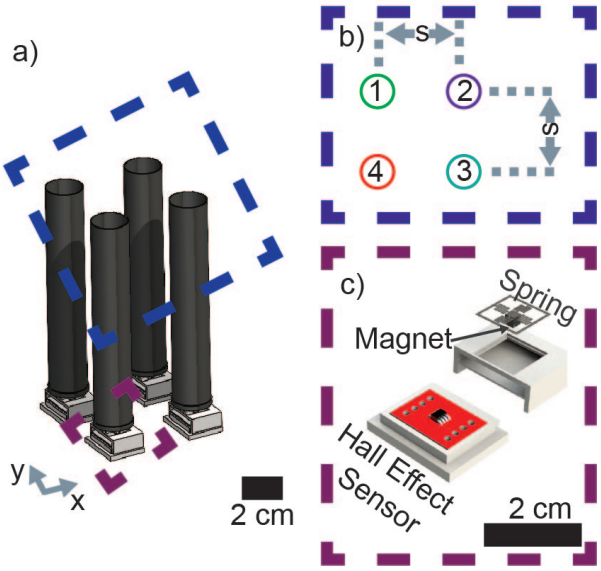

Figure 5.3: a) 2x2 array design. b) Four whiskers are separated by $s = 35\,\text{mm}$ in both x and y axes in an array. c) The sensors are designed similar to [52]. A Hall effect sensor measures the rotations of the whisker drag element suspended by a spring. (Supplementary Video).

to analyze data. After calibrating the sensor, the magnetic field signals B_{xn} and B_{yn} are passed through an averaging filter with a window of 5 before solving for the magnitude of the signal ($||B_n||_2$). Subscript n refers to the sensor number in the array. Averaging is important as it allows us to solve for the net vector rather than the magnitude of oscillation. Finally we solve for the direction of each sensor's signal (θ_n). θ_n is always a measurement of an individual sensor and φ (Fig. 5.2) is always a prediction about environmental flow.

$$\theta_n = \arctan \frac{B_{yn}}{B_{xn}} \tag{5.1}$$

$$||B_n||_2 = \sqrt{B_{xn}^2 + B_{yn}^2} \tag{5.2}$$

When measuring flow shadowing, the final step is to normalize the signal magnitude by $||B_{max}||_2$, the max value of $||B_n||_2$ in the array. This step provides a magnitude relative to the array rather than relative to the calibration velocity.

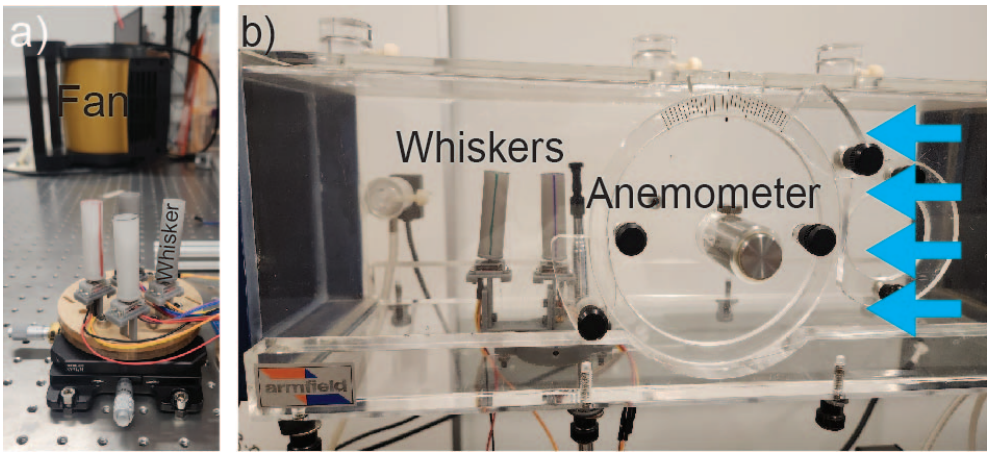

Figure 5.4: The whisker arrays were tested under two types of airflow. a) One or two fans supplied airflow to a whisker array mounted on an optical table. The optical table and a ThorLabs rotational stage aided repeatability as the headings of flow were varied around the array. b) A wind tunnel was used to apply airflow from a single direction to whisker arrays.

5.3.4 Experimental Setups

Wind Tunnel Tests

Wind tunnel tests (Fig. 5.4b) were carried out in a C15-10 Armfield subsonic wind tunnel. An anemometer (4330, Thomas Scientific) was placed next to the sensing array to ensure that the desired velocities were reached. The mounts for the tests were 3D printed to allow flow orientation to be controlled at intervals of 5°. Wind tunnel tests were used to evaluate the response of pairs of sensors to flow from a single direction.

Box Fan Testing

Multiple flow directions cannot be provided in a controlled wind tunnel setup, so instead two box fans (Lasko Pro performance three-speed fan, Stanley Model 655 704 three-speed fan) were used to evaluate flow from multiple sources (Fig. 5.4a). The second fan was only used to test flow from multiple sources, and we made no attempt to keep these flows laminar. Here, the array was placed on a Thorlabs manual stage which allowed for control of the incident angle of flow within 0.5° relative to the array. Fan tests were used to evaluate the response of individual sensors, pairs of

sensors, and a 2x2 array of sensors to flow from one or more sources.

5.3.5 Experimental Tests

Sensor Characterization

Using the box fan setup, a single whisker was tested under single flow with orientations between 0°-360° in increments of 10°. The test was performed at $6.5\,\mathrm{m\,s^{-1}}$.

Flow Shadowing

We characterized flow shadowing with pairs of whiskers using both the box fan and wind tunnel environments. Using both environments allowed us to determine how whisker sensor responses could be affected by the additional turbulence applied by the fans. Two whiskers were separated by a spacing s = (35 mm in the wind tunnel30 mm using the fan). The whiskers were rotated around the upstream whisker in headings (φ) of five degree increments between $-30°$ and 30°. The variation in heading angle changed the percent of occlusion ($\%_{occ}$) of the downstream whisker which was calculated as follows, where d represents the diameter of the drag element.

$$\%_{occ} = \frac{d - min\{s * sin(\varphi), d\}}{d} \tag{5.3}$$

In the wind tunnel, flow velocities of both $5\,\mathrm{m\,s^{-1}}$ and $6.5\,\mathrm{m\,s^{-1}}$ were applied to the sensors. For the box fans, velocities of $5.5\,\mathrm{m\,s^{-1}}$ and $6.5\,\mathrm{m\,s^{-1}}$ were applied. First the signals were normalized compared to the values recorded during the calibration data. Second we solved for θ_n and $||B_n||_2$ using Eqns. 5.1,5.2. Finally, the value of the upstream and the downstream whiskers were compared to calculate $\frac{||B_{down}||_2}{||B_{up}||_2}$, where 'up' represents the signal from the upstream whisker, e.g., the whisker closer to the fan. The tests were repeated, switching the upstream and downstream whiskers.

Spacing Tests

We also tested how the spacing between a pair of whiskers, s, affected the amount of flow shadowing under 100% occlusion (Eqn. 5.3, the upstream whisker completely shadowing the downstream whisker) using the fan experiment. s was varied from 30 mm to 50 mm in 5 mm increments (Fig. 5.4a). The applied flow speed was $6.5\,\mathrm{m\,s^{-1}}$. In initial tests, we found that the two whiskers made contact at this flow speed if the spacing was below 30 mm.

Single and Double Flow Characterization

We tested how the measured response of a 2x2 array of four whiskers (Fig. 5.4a) varied under different headings and velocities of airflow. The array was tested in all combinations of the following variables $\varphi_1 = \{0°, 15°\}$, $\alpha = \{45°, 90°, 135°\}$, $v_1 = \{$ 5.2 ,$6.5\,\mathrm{m\,s^{-1}}\}$ and $v_2 = \{7.3,\ 8.3\,\mathrm{m\,s^{-1}}\}$. Combinations of the flow speeds led to $\frac{v_1}{v_2}$ ratios of $\{0.60, 0.71, 0.90\}$.

5.3.6 Algorithm

Two algorithms were considered in this work. In Method 1, we assume that φ_1 is known (e.g., from an IMU or optic flow sensor) and we use the array results to solve for φ_2. In Method 2, we assume that no information is known about either φ and solve for both headings. The magnitude and angle from each whisker sensor is combined into a vector $\overrightarrow{B_n}$. The two methods are outlined below, but are also visually represented in Fig. 5.10.

Method 1: φ_1 is known

1. Using Eqns. 5.3, 5.4 predict the expected response of Flow 1, $\overrightarrow{B_n'}$, with known φ_1.
2. $\Delta\overrightarrow{B_n} = \overrightarrow{B_n} - \overrightarrow{B_n'}$
3. Remove whisker data where $\%_{occ} = 0$.

4. Decompose $\Delta\overrightarrow{B_n}$ into ΔB_y and ΔB_x.

5. predicted $\varphi_2 = \arctan(\frac{\sum_{i=1}^{n} \Delta B_y}{\sum_{i=1}^{n} \Delta B_x})$

Method 2: Solving for both φ values

1. Estimate φ_1: A first estimate for φ_1 can be found from the θ_n value furthest from the mean of all θ_n, $\hat{\theta}$. Picking this value decreases the chance of predicting φ_1 as the net flow.

2. Using Eqns. 5.3, 5.4 predict the expected response of first flow, $\overrightarrow{B_n'}$, with predicted φ_1.

3. $\Delta\overrightarrow{B_n} = \overrightarrow{B_n} - \overrightarrow{B_n'}$

4. Decompose $\Delta\overrightarrow{B_n}$ into ΔB_y and ΔB_x

5. predicted $\varphi_2 = \arctan(\frac{\sum_{i=1}^{n} \Delta B_y}{\sum_{i=1}^{n} \Delta B_x})$

6. Repeat steps 2-5, starting with φ_2 as the input flow to improve upon φ_1 prediction.

5.4 Results and Discussion

5.4.1 Single Sensor Characterization

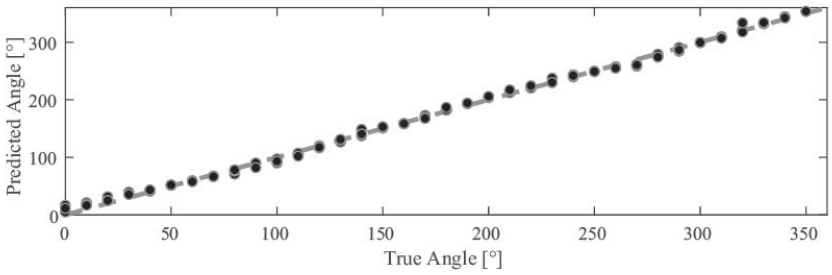

Figure 5.5: Comparison of the true heading of flow (φ) versus the sensor predicted flow heading (θ) for a single sensor with airflow provided by a fan. Each heading includes two trials.

The sensor was updated from [52] to obtain a uniform response from all flow headings by changing the previous cross shape to a circle. The accuracy of the

sensor's θ reading was compared to the applied flow φ and found to be accurate with a root mean square error of 5.22° (Fig. 5.5).

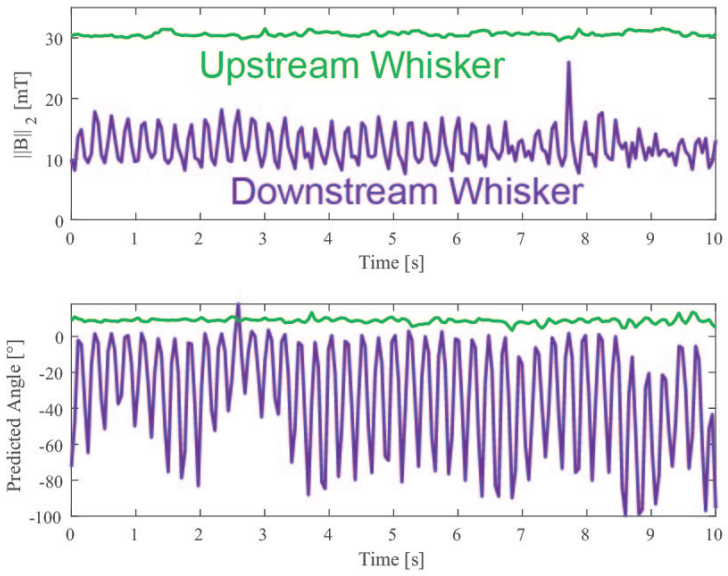

Figure 5.6: Results from a single trial of two whiskers placed under a flow of v =6.5 m s^{-1}, $\varphi = 0°$ in the wind tunnel. In this case, $\%_{occ} = 100$ %. a) Magnitude of the upstream (green) and downstream (purple) whisker response ($||B||_2$, Eqn. 5.2). b) The estimated direction of the whiskers' responses (θ, Eqn. 5.1).

5.4.2 Flow Shadowing Characterization

Two sensor arrays were used to characterize flow shadowing. As expected (and seen in Figs. 5.1 and 5.6), the downstream whisker exhibits a smaller signal response $||B_{down}||$ when occluded by the upstream whisker. Results in Fig. 5.6 also indicate that a more turbulent flow is incident on the downstream whisker. The $||B_{down}||$ signal is more oscillatory and the predicted angle changes frequently. These results were true in both the wind tunnel and under flow from the box fan although the oscillations of both whiskers were greater under the more turbulent flow from the box fan.

Spacing

We predicted that the effect of flow shadowing would decrease as the spacing between the whiskers increased. This expectation agreed with the results in Fig. 5.7. The

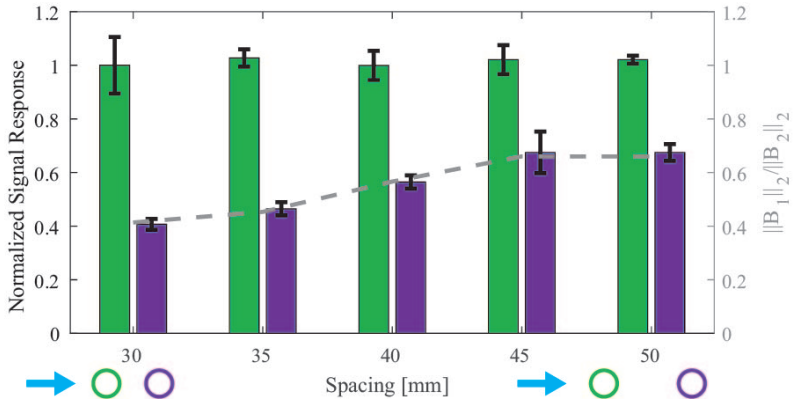

Figure 5.7: The signal response of two whiskers under 100% occlusion were recorded as the spacing, s, between the two whiskers was changed. Error bars represent the standard deviation over 3 trials.

results indicated that a more densely packed array of whiskers will improve the flow shadowing effect. We chose a final spacing of 35 mm to maximize flow shadowing while minimizing the chance of whisker-to-whisker contact.

Percent Occlusion

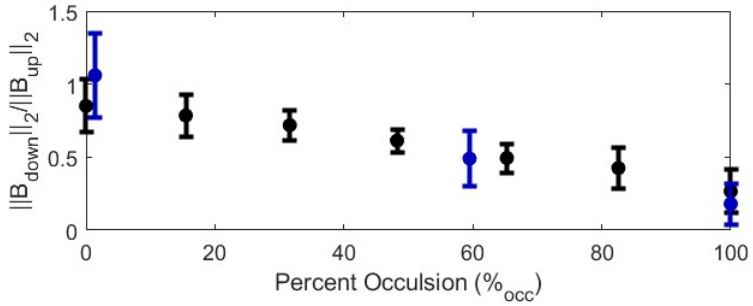

Figure 5.8: Whisker sensors were rotated relative to each other and the heading of flow. This rotation changed $\%_{occ}$ as calculated in Eqn. 5.3. When $\%_{occ} \approx 100\%$ the downstream whisker's surface area is fully shadowed by the upstream whisker. When $\%_{occ} \approx 0\%$ the downstream whisker is fully exposed to the flow. The affect of this shadowing on the sensor signal was measured using the fan and wind tunnel setups. The tests were performed with a fan (black) and then repeated in a wind tunnel (blue). The spacing in the fan test was 30 mm and in the wind tunnel 35 mm. Error bars represent the standard deviation over three trials.

Fig. 5.8 compares the relative magnitudes of the upstream and downstream whiskers versus the expected percent of occlusion (Eqn. 5.3). Note that in the results, some flow reaches the downstream whisker even at 100% occlusion. Flow occlusion was tested in a variety of wind flow types and directions of the whisker;

in every result a linear trend was the best descriptor between the percent occlusion and the magnitude ratio. For the algorithm portion of the study, this relationship is represented with the following equation.

$$\frac{||B_{down}||_2}{||B_{up}||_2} = 1 - 0.8 * (\%_{occ}/100) \tag{5.4}$$

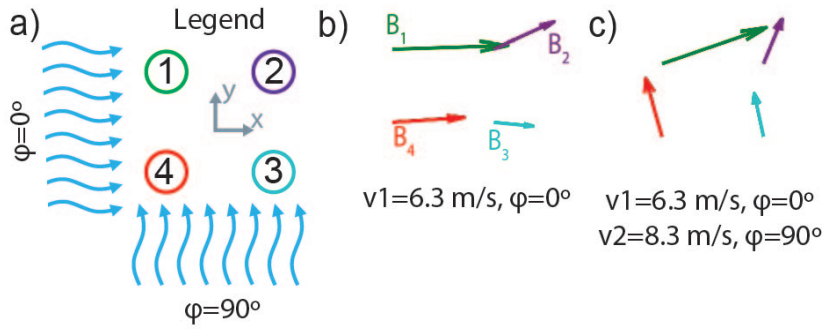

Figure 5.9: Visualization of the flow vectors from the 2x2 array of whiskers in a) under b) one and c) two sources of flow.

5.4.3 Single and Double Flow Characterization

The effect of occlusion is also seen on a 2x2 array of four whiskers under single flow (Fig. 5.9b). In the example shown, the upstream whiskers' magnitude response $||B||_2$ is larger than the downstream whiskers. The flow direction predicted by the upstream whiskers (θ) is also more accurate to the true flow heading ($\varphi_1 = 0°$). When a second flow source is introduced (Fig. 5.9c), flow blocking becomes multi-directional. In this experiment, whisker 1 is 100 % occluded from the second flow source at $\varphi_2 = 90°$ and therefore the majority of its magnetic field response (B) is due to flow 1 ($\varphi_1 = 0°$). In contrast, whiskers 3 and 4 are 0% occluded from the 90° flow which is also a higher velocity flow than flow 1 so their signal is strongly affected by flow 2. Whisker 2 is 100 % occluded from both sources of flow and its direction prediction is closer to the net flow that we would expect if no flow shadowing occurred. The flow shadowing responses in Fig. 5.9c illustrate the asymmetry in the whisker response across the array that allows us to estimate

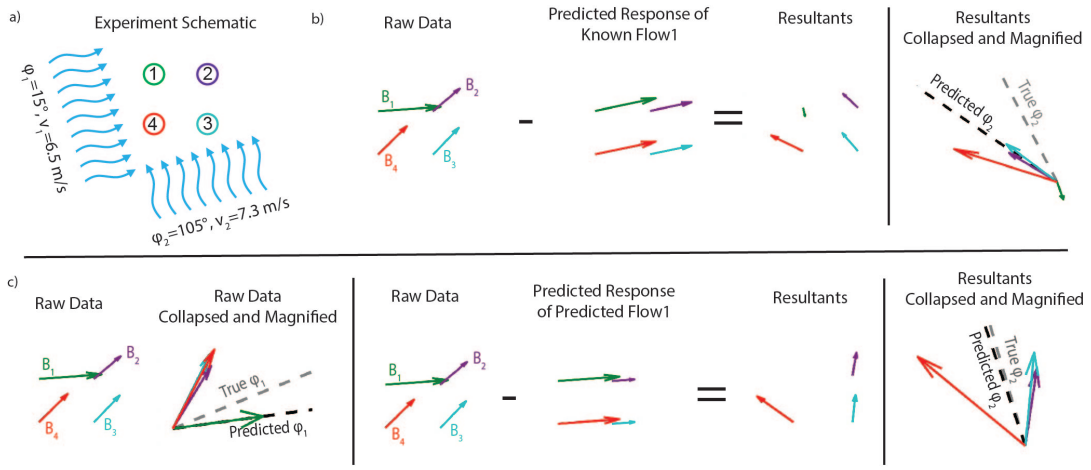

Figure 5.10: a) A single trial of data is used to illustrate how the two algorithms work. b) Algorithm 1 considers a scenario where one of the directions of flow is known (φ_1) and the algorithm needs to estimate $\hat{\varphi}_2$. c) Algorithm 2 is designed to estimate $\hat{\varphi}_1$ and $\hat{\varphi}_2$ with no prior knowledge. It therefore begins by making a guess about $\hat{\varphi}_1$ before applying a similar method to Algorithm 1.

headings of the two flow sources and prevents the problem shown in (Fig. 5.2c) where all four sensors respond to the average flow.

5.4.4 Algorithm

The algorithms to estimate φ_2 (if φ_1 is known) or $\varphi_{1,2}$ (if no flows are known) take advantage of the array's asymmetry. Method 1 uses the known φ_1, calculates the expected flow across the array for this flow from Eqn. 5.4, and uses the result to estimate the direction of the second flow (Fig. 5.10b). Method 2 assumes no prior knowledge of the flow headings. A first estimate of φ_1 is found from the flow direction in the array most separate from the mean (Fig. 5.10c). φ_2 is then estimated using a similar approach to Method 1.

Results were collected across at least 2 trials of 24 different combinations of two flows with varying headings and speeds and are summarized in Table 5.1 for angle combinations with $\alpha = 90°$ and 135°. For each α and flow speed ratio, a root mean square error (RMSE) was calculated for all trials as $\text{RMSE} = \sqrt{\Sigma_1^n(\varphi_x - \varphi_{x,predicted})^2/n}$.

Overall, the calculated RMSE for the various headings across both algorithms were relatively low, especially given that a small array of whiskers (2x2) was used in this study. We did find in test cases when $\alpha = 45°$ (not included in Table 5.1)

Table 5.1: Flow Heading RMSE Across All Trials

		Method 1	Method 2	
α	$\frac{v1}{v2}$	φ_2 RMSE	φ_1 RMSE	φ_2 RMSE
90°	0.9	30.5°	9.9°	22.9°
90°	0.7	16.0°	13.2°	23.7°
90°	0.6	15.4°	7.8°	7.3°
135°	0.9	8.9°	43.2°	26.1°
135°	0.7	22.1°	36.3°	24.9°
135°	0.6	20.2°	45.0°	16.8°

that error became significantly higher. In these cases where the two incident flow sources are closer in direction, the small 2x2 array is not able to provide enough asymmetry. The creation of larger arrays to improve accuracy and the smallest distinguishable α is an interesting direction for future study. The velocity ratio also seems to affect the accuracy of the heading predictions although we cannot yet say this with statistical certainty. As expected, prediction estimates seem to improve as the velocity ratio moves further away from 1 (e.g., one flow is significantly faster than the other). Finally, while the results presented are calculated from 50 collected data points, the algorithms will work with as few as 5 data points since these result in a standard deviation below the sensor's RMSE. This will ultimately reduce the time required to estimate the flow vectors.

5.5 Conclusion

This work demonstrates the benefits of flow shadowing, a phenomenon that occurs when whiskers are packed densely in an array, for estimating the headings of multiple flow sources. Using a modified version of whisker-based flow sensors from previous work [35], we quantified the flow shadowing effect and derived an empirical model. Using a 2x2 whisker array, we showed that flow shadowing creates a direction-dependent asymmetric response. Asymmetry in the array response allowed our algorithms to predict the flow headings with relative accuracy. We expect that more whiskers, a higher density, and improvements to the algorithm can further improve

our results, including an estimate of velocity for both flows. The work presented here represents the first steps toward sensors that are capable of a more nuanced understanding of the flow surrounding a variety of unmanned aerial vehicles.

Chapter 6

Modeling Flow Shadowing to Detecting Dual Flow

Paper:

Kent, T. A., Thomas, L., & Bergbreiter, S. Flow Shadowing: Detecting Wind on a Moving Drone using a densely packed array of Whisker-Sensors ***(In Preparation)***

Author Contributions:

TK designed the sensor, designed, automated, and performed all benchtop tests, developed the code/ algorithms to interpret sensor signals, and performed all data analysis after the test. LT designed the system to attach sensors to the drone, controlled the drone during experimental testing, developed the code to connect the whisker sensors to Bluetooth, and guided the drone testing for accurate data capture. LT and TK worked together to design the experiments performed on the drone. SB guided the research. All edited the manuscripts and figures.

Abstract

Dedicated 2D or 3D wind sensors have proved advantageous in keeping quadrotors stable in the wind. However, flow sensors are rarely used on a moving quadrotor be-

cause the quadrotor's motion creates a drag signal on the flow sensor. When the flow sensors try to measure wind during quadrotor motion, the sensor instead measures the quadrotor's combined airspeed and windspeed. Here, we build on earlier work demonstrating the potential of densely packed whisker sensors to separate multiple flow sources through a phenomenon we call "flow shadowing." Flow shadowing is given that name because, in a densely packed array, the upstream whiskers shadow the downstream whisker, changing the amount of flow that reaches them. Here, we extend the proof of concept to a model that accurately represents the flow shadowing phenomenon and can be applied to arrays of different shapes. The improved model increased flow heading detection accuracy. We also demonstrate the flow shadowing phenomenon on a moving quadrotor. The improved accuracy and proof of the flow shadowing phenomenon further emphasizes the potential of flow shadowing to enables a deeper understanding of the environment in which quadrotors operate.

6.1 Introduction

Commercial applications of quadrotor research, including midflight package pickup [76] and outdoor infrastructure inspection of wind turbines [122], have shown impressive performance in the lab. To translate these capabilities and control from the lab to deployment, it is important to consider the effect of less structured environments. Specifically, researchers often avoid windy conditions when designing new control systems, waiting for clear weather, or conducting tests indoors.

When wind is present, quickly estimating wind forces is essential for flight stability and achieving the desired control [123]. Wind can be quantified using inertial measurement units [86], ground speed (measured by cameras and GPS) [123], and motor signals such as power requirements and propeller rotation speed [124]. However, these sensor signals could also indicate payload motion, external contact, or motor degradation [85]. For this reason, in addition to redundancy, a dedicated wind sensor, less affected by extraneous stimuli, would be an asset to drone sensing.

Unlike airspeed sensors on fixed-wing aircraft, quadrotors need sensors capable of

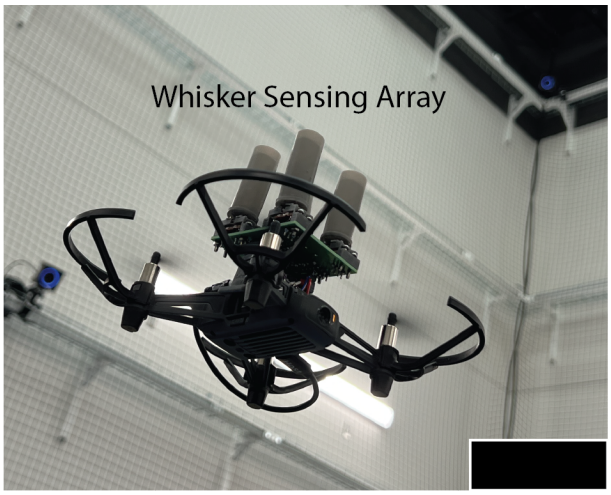

Figure 6.1: A Flow Shadowing 2 x 2 grid of whiskers on a micro quadroter in flight. Scale bar represents 100 mm

.

estimating 2D or 3D wind vectors. Whisker/hair-inspired flow sensors are a common approach to wind sensing on quadrotors. These sensors have been used to estimate drone speed by measuring relative airflow due to drone motion [36, 125], estimate wind speed during hover [95–98], and to improve hovering stability [36, 126].

However, to the authors' knowledge, using whisker-inspired sensors to estimate wind speed on a moving quadrotor has yet to be demonstrated. This task is more challenging because the wind and drone movements both create drag forces on the whisker flow sensor [36], which will combine into a single vector signal. Previously, we hypothesized that an array of densely packed whisker-inspired sensors could be used to identify two separate flow sources, such as wind and flow due to drone motion, and we demonstrated the basic principle of this idea in a benchtop experiment [99]. In that work, a whisker downstream of the flow source could be "shadowed" by an upstream whisker, reducing its signal response. Measurement of signals from a four-whisker array allowed us to estimate the relative angles of two flow sources using algorithms based on a simplified model of the flow shadowing phenomenon. The approach demonstrated an innovative methodology but still had significant limitations: it worked best when 1) the two flow sources had similar velocities, and 2) when the relative flow angles from two sources caused large amounts of shadowing. Despite these limitations, in specific flow combinations, a secondary flow heading could be

estimated with a root mean square error (RMSE) of 7.3° using this approach [99].

The work described in this paper includes several contributions beyond the previous initial demonstration of the flow shadowing phenomenon. We expand the previous flow shadowing model by using a data-driven approach to develop a set of equations that estimate how flow shadowing affects sensor signals based on input flow vectors and array shapes. Our model can predict sensor signals from shadowing for novel array shapes, including expanded arrays of up to nine whiskers (compared to the original four).

The improved accuracy of our data-driven model also allows us to generate synthetic data to improve our flow estimation algorithms. For example, we use this data to generate expected array signals when exposed to multiple flow sources, which our algorithms match to the collected signals. We then demonstrate wind flow and airspeed signals on a quadrotor for the first time. We incorporated a 4-whisker array onto a small (80 g) quadrotor to quantify a wind vector (from a fan) while the quadrotor is in flight (Figure 6.1).

6.2 Methods: Model Development

Our goal is to create an array of whisker-inspired flow sensors that can accurately define airflow when there are one or two airflow sources. To achieve this, we created a whisker-inspired airflow sensing array based on the flow shadowing principle described in [99].

6.2.1 Nomenclature for the Airflows and Flow Shadowing

In this work, we develop data-driven models to map incoming airflows to sensor signals as well as algorithms to determine airflows from measured sensor signals. As such, it is important to define a nomenclature for both the airflows and sensor signals. Airflow vectors are defined by their velocity component v and direction component φ measured in $\mathrm{m\,s^{-1}}$ and $^\circ$ respectively (Figure 6.2). These vectors are

defined relative to the drone coordinates.

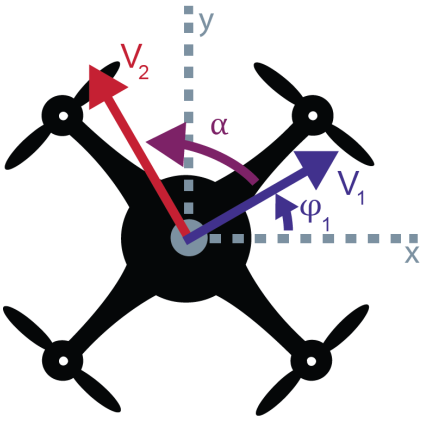

Figure 6.2: Problem Nomenclature: The goal of this research is to define two flows by their heading (φ_1 and φ_2) and speed (v_1, v_2) relative to the drone's axis. The relationship between the two flows, such as the angle between the two flows (α) and the velocity ratios ($\frac{v_1}{v_2}$), can affect the difficulty of calculating the flow vectors from the sensor data.

In addition, because flow shadowing is a critical component of this work, it is important to define this phenomenon as in our previous work [99]. In a densely packed array, the whiskers closest to the incoming flow source are fully exposed to the flow (and defined as "upstream" whiskers; any whiskers "downstream" of another whisker may exist in the upstream whisker's "shadow" and receive less exposure to the wind flow. For this reason, this idea was called "flow Shadowing".

6.2.2 Sensor and Array Design

This work uses the same sensor design used in previous work [99], which was based on the sensors in [35]. A brief description of the sensor is shown in Fig. 6.3b is provided for convenience.

The whisker-inspired body is a hollow cylinder 40 mm high and 15 mm in diameter (Fig. 6.3b). Airflow on the whisker sensor causes a rotation about the center of a serpentine spring cut from steel (LPKF photolaser U4). The whisker tapers for 2 mm beyond its height to create a square the same size as a plate at the center of rotation of the spring. Glue is applied to join the spring and the whisker. The spring dimensions are listed in [35, 99].

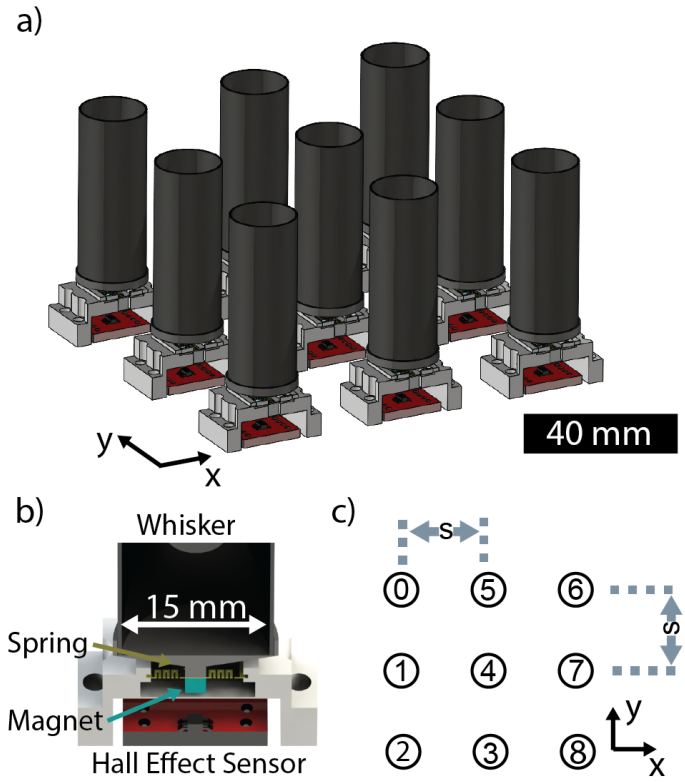

Figure 6.3: a) An array of nine whisker sensors is densely packed in a grid shape. b) Each sensor has a whisker body attached to a spring, with a magnet on the opposite side. A Hall Effect sensor measures the changes in the magnetic field caused by the whisker's rotation in the wind. c) The array shape has whiskers spaced (s) 35 mm apart and numbered in accordance with the picture.

Simultaneous to the whisker rotation, an equal but opposite rotation occurs for a magnet (2 mm^3 C0020, Supermagnetman) beneath the spring. The rotation of the magnet is sensed by measuring the magnetic field using a Hall Effect Sensor (TLE493-W2B6 A0, Infineon). The change in the magnetic field is approximately linearly related to the drag force [100]. The edges of the spring are fixed inside a slot in the 3D printed housing, which is secured to a circuit board where the Hall Effect sensors are soldered.

In this work, many of these individual whisker-inspired sensors were combined into a densely packed array. The shape of the array was maintained using a custom printed circuit board (PCB). Each sensor in the array is connected to an Arduino Uno through I2C multiplexers (TCA9548A 1-to-8 I2C Multiplexer). The PCB provided a 3x3 grid onto which whisker sensors could be assembled; the centers of each

whisker on this grid are spaced a distance $s = 35\,\text{mm}$ apart. The Hall effect sensors' axes are aligned with the axis of the entire array (Fig. 6.3a) and the numbers circled in Fig. 6.3c represent the whisker number in the array. Whisker-inspired sensors are attached to the circuit boards with screws, and the setup can sample all nine sensors at sample rates of 60 Hz (Fig. 6.3a).

6.2.3 Signal Processing

Each whisker sensor outputs magnetic field strength signals that need to be processed. Due to manufacturing tolerances, each sensor can react somewhat differently to the same airflow so it is important to calibrate each sensor in advance. To calibrate, we collect the magnetic field signal strength when airflow is applied to the the Hall Effect sensor's +x, -x, +y, and -y axes. For each whisker, we apply airflow at three different velocities and record the magnetic field signal along that same axis. The magnitudes of this airflow range from $2\,\text{m}\,\text{s}^{-1}$ to $6\,\text{m}\,\text{s}^{-1}$.

From the analytical model of the springs [127] used in previous work [99, 100], we know that an approximately quadratic relationship exists between the magnetic field magnitude B and the airflow velocity, v: $B = m * v^2$. m is a constant that we fit to the calibration data using the least squares method. Because we calculate an m value for each axis we have four total values, $\overrightarrow{m_i}$, for each whisker.

To effectively compare the whisker signals in the array we also need the signals to be equal when no shadowing occurs. To achieve this, we normalize each whisker's response in the whisker array. In Eqn. 6.1, $\overrightarrow{B_i}'$ represents the raw (non-normalized) magnetic field measurement for a given airflow vector, $\overrightarrow{m_i}$ represents the related calibrated fit constant, and $\hat{m}$ represents the average fit constant across the entire array (assuming n whiskers in the array, this is the average of $4n$ different calibration m values). $\overrightarrow{B_i}$ represents the normalized magnetic field measurement.

$$\overrightarrow{B_i} = \frac{\hat{m}}{\overrightarrow{m_i}} * \overrightarrow{B_i'} \tag{6.1}$$

After this normalization step, the magnitude of the magnetic field B is related to the airflow velocity by Eqn. 6.2 on each whisker regardless of flow heading.

$$B = \hat{m} * v^2 \tag{6.2}$$

When exposed to airflow, the sensors also oscillate due to flow turbulence and flow vortices generated when the flow interacts with the whiskers. As such, it is also necessary to filter the magnetic field signals B_{xi} and B_{yi} to remove some of this additional noise. A moving average filter (5-sample window) is used on B_{xi} and B_{yi} before calculating the magnitude (Eqn. 6.4) and direction (Eqn. 6.3) of each sensor's signal. In these equations, the subscript i refers to the sensor number in the array (Fig. 6.3c).

$$\theta_i = \arctan \frac{B_{yi}}{B_{xi}} \tag{6.3}$$

$$B_i = \sqrt{B_{xi}^2 + B_{yi}^2} \tag{6.4}$$

6.3 Results: Model Development

In our previous work, we demonstrated the potential of a densely packed array of whisker-inspired flow sensors to generate signals that provide information about the flow vectors from up to two flow sources [99]. Inherent to that work's ability to interpret the signals and estimate multiple flow vectors was a model that could predict the expected sensor response based on a known airflow. As an extension to that previous work, this paper develops a more accurate and more generalizable model between flow input and sensor response to further improve our ability to estimate flows across a wider variety of flow conditions. We develop this model using a data-driven approach.

This model uses an expanded set of equations compared to [99], with constants fit using a least squares method. The model estimates the expected change in the

magnetic field vector of our sensor $\overrightarrow{B}$ given one or more known airflow vectors of velocity v and direction φ.

6.3.1 Experimental Data Collection

To fit our model. We tested how varying arrays of whiskers responded to flows from a single flow source at different flow headings. The flow source was provided by an exhaust fan (VEVOR 10" Exhaust). The speed of the fan could be adjusted using an Exhaust Fan Speed Controller (BN-Link) and was measured using an anemometer (4330, Thomas Scientific). We attached a 12" x 12" flow straightening screen (made from a $\frac{1}{4}$" thick metal plate patterned with a honeycomb design) to the front of the fan using tape. The array was placed on a NEMA 23 stepper motor that could rotate in increments of 1.6°. The whisker sensors were screwed into the circuit board, making the array shape modular. Arrays of 1, 2, 3 and 4 whiskers were used for fitting different components of the flow shadowing model.

The model was designed based on flow speeds between $1\,\mathrm{m\,s^{-1}}$ to $5\,\mathrm{m\,s^{-1}}$, and therefore we only assume its validity in this range of velocities. These speeds result in a Reynolds number between 1000 and 6000 for air passing the whiskers, making the flow transitional. In previous work, [99], flow shadowing was measured using a box fan, which was also in the transition regime, and in a wind tunnel, which produced laminar flow. Responses were found to be similar for both of these airflow conditions.

6.3.2 Single Flow, Single Whisker

Before we can fit our model, every whisker used must be calibrated according to our signal processing methodology. The sensors are calibrated one at a time to avoid interaction forces with other whiskers. After calibration, the sensors are marked so that they are always in the location on the PCB that they were calibrated in. After calibration, Eqn. 6.2 can be used to predict the magnetic field strength, B, within $0.47\,\mathrm{mT}$ given a known airflow velocity. The fit between Eqn. 6.2 and the

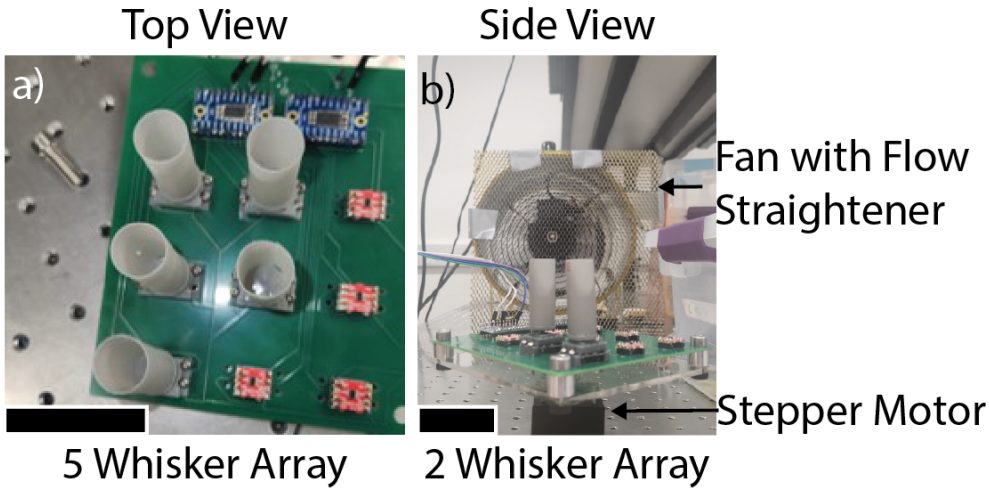

Figure 6.4: Experimental Test Setup: a) Screws attach five whiskers to the circuit board in a 3 x 3 grid. b) Airflow is applied to two whiskers as the whiskers as they are rotated by a NEMA 23 motor. Scale bars represent 40 mm

experimentally collected magnetic field strength of for four whiskers tested at four non-zero velocities has an R^2 value of 0.99 (Fig. 6.5). The Root Mean Square error between the applied angle of airflow (φ) and the calculated θ from sensor readings (Eqn. 6.3) for airflow at a velocity of $4.5\,\mathrm{m\,s^{-1}}$, is 5.2°.

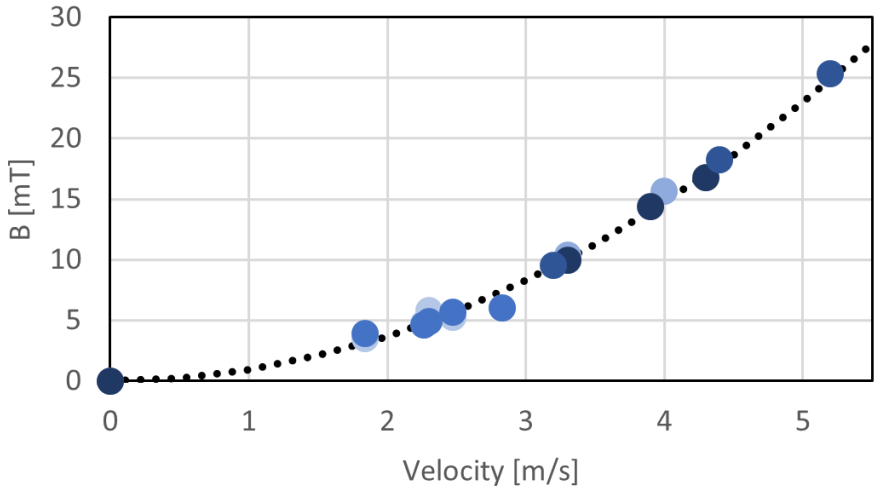

Figure 6.5: The relationship between velocity and magnetic field for this sensor design has previously been established as $B = m * v^2$ [100, 127]. After calibration (Eqn. 6.1), the signal strength, B for each whisker (4 shades of blue) should be approximately the same given the same applied flow velocity.

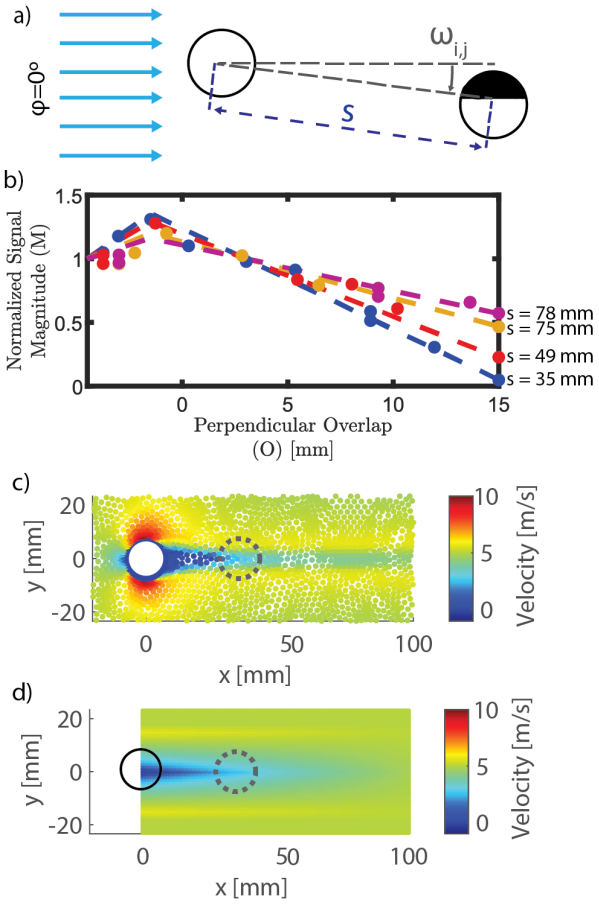

Figure 6.6: The goal of modeling is to create a set of equations that can faithfully approximate how airflow travels through the array. a) For two whiskers, the important variables are the overlap O and the spacing s. To evaluate the generated model, we compared the following: a) experimental results, b)results from ANSYS fluent, and c) the results of the data-driven model. In this example, a cylinder is placed at the origin in a $5\,\mathrm{m\,s^{-1}}$ flow field parallel to the x axis. The dashed gray circle shows where the closest whisker would be located under this flow.

6.3.3 Shadowing from a Single Whisker

In flow shadowing, a downstream whisker exists in the upstream whisker's shadow (Fig. 6.6a), which prevents the full magnitude of flow from reaching the downstream whisker (Fig. 6.6). For this array design, previous work has shown that the ratio, M, between the normalized signal strength of the upstream whisker (B_j) and the downstream whisker (B_i) is not velocity dependent [99].

$$M_{i,j} = \frac{B_i}{B_j} \tag{6.5}$$

Previous work has also shown that the ratio M is affected by the overlap, O, (indicating the length of whisker directly shadowed by an upstream whisker, Fig. 6.6) and the spacing, s, between the two whiskers.

Unlike prior work, our new model allows M to be greater than 1 by setting the denominator as the signal from the upstream whisker instead of the whisker with the maximum signal. As a result, our new model recognizes that the flow velocity increases as the flow travels around the upstream whisker circumference. This local velocity increase is visible in the results from the ANSYS fluent test performed for laminar flow over a 15 mm diameter cylinder (Fig. 6.6c). The velocity increase was also verified in separate tests in which we used the anemometer to read the flow speed directly in front of the downstream whisker.

In our new model, we use a series of equations to quantify the affect of the overlap O and spacing s on the magnitude ratio M. The equations are fit to experimentally collected data of two whiskers rotated by a motor to vary the angle between the whiskers relative to the flow field ($\varphi - \omega_{i,j}$) (Fig. 6.4b). Four spacings (s) between the whiskers were tested under an airflow of $4\,\mathrm{m\,s^{-1}}$. From the experimental data we estimated the constants in our equations by minimizing the error.

It is first important to calculate the overlap, $O_{i,j}$, of the two whiskers in the direction perpendicular to the flow heading. This variable is represented pictorially in Fig. 6.6a, where the height of the shadow (shaded region) represents an overlap of 6 mm. The variable is quantified using Eqn. 6.6 where $s * sin(|\varphi - \omega_{i,j}|)$ represents the distance between the centers of two whiskers along an axis perpendicular to the airflow using the global angle between the two whiskers ($\omega_{i,j}$) and the global angle of flow (φ).

$$O_{i,j} = d - s * sin(|\varphi - \omega_{i,j}|) \tag{6.6}$$

Spacing (s) affects airflow that reaches the downstream whisker (Fig. 6.6a). The larger the spacing between two whiskers, the more time the velocity field has to

return to the uniformity it had before encountering the upstream whisker. We represent the affect of spacing in Eqn. 6.7, where $S_{min}^{i,j}$ represents the minimum value of $M_{i,j}$ for a given spacing. This minimum occurs when the downstream whisker has an overlap equal to the whisker diameter, d. We use a linear relationship to represent the relationship between $S_{min}^{i,j}$ and s with C_2 and C_3 fit to the experimental data collected when there was a 15 mm overlap.

$$S_{min}^{i,j} = C_2 * s_{i,j} - C_3 \tag{6.7}$$

We combine Eqn. 6.6 and Eqn. 6.7 to model $M_{i,j}$ as a piecewise function of $O_{i,j}$ and $S_{min}^{i,j}$ in Eqn. 6.8. The transition points of the piecewise function are values of O and are depicted pictorally on Fig. 6.6b. For values of O below C_1 (the point at which the perpendicular distance between the two whiskers results in the maximum $M_{i,j}$ signal, $S_{max}^{i,j}$) the first equation is used. C_4 is the experimentally fit overlap point where $M_{i,j}$ equals 1. The equation forces $M_{i,j} = S_{min}^{i,j}$ when $O = d$ and $M_{i,j} = 1$ when $O = C_4$.

$$M_{i,j} = \left\{ \begin{array}{ll} \frac{O-C_4}{d-C_4} * S_{min}^{i,j} + \frac{d-O}{d-C_4}, & \text{if } O < C_1 \\ 1 + (O - C_5)\frac{S_{max}^{i,j}-1}{C_1-C_5}, & \text{if } C_1 < O < C_5 \\ 1, & \text{if } C_5 < O \end{array} \right\} \tag{6.8}$$

The fit variables for all O values below C_1 are in Table 6.1. It is important to note that sensor calibration significantly affects the constants in Eqn., 6.7.

Table 6.1: Calibration values for modeling normalized signal magnitude during flow shadowing

Variable Name	Equation Number	Variable Name	Value
C_1	eqn. 6.8	Max M Point	−1 mm
C_2	eqn. 6.7	Spacing Slope	0.01
C_3	eqn. 6.7	Spacing Intercept	0.1
C_4	eqn. 6.8	Transition Point	3 mm
C_5	eqn. 6.8	Max Effect Point	−4 mm

The final variable we fit to the data is C_5 which represents the overlap value where increasing the perpendicular distance is too large for measurable flow shadowing affects. After this point no shadowing occurs so $M_{i,j} = 1$

For the experimental data we collected at four different spacings (Fig. 6.6c), the average R^2 value for $M_{i,j}$ is 0.94.

The model for M gives us the strength ratio of the signal B between the upstream and downstream whiskers at any given x- and y-point. Since B is proportional to v^2, $\sqrt{M}$ represents the ratio of the sensed flow velocity for the upstream and downstream whiskers (Fig. 6.6d). Our model predicts what a whisker would sense if it were centered at an x,y point. This means our model is closer represents averages over the 15 mm diamater whisker surface area. By contrast, the ANSYS results in Fig. 6.6c represents the true airflow velocity at that point. Therefore, we do not expect a perfect match between the two models. Even still, the shape and approximate velocities at specific locations demonstrate significant visual similarity.

6.3.4 Shadowing from Multiple Whiskers

Previous models did did not consider a flow angle φ where a downstream whisker is in the shadow of more than one other whisker. Here, we model multiple shadows, hereafter referred to as dual shadowing. There are two different cases of dual shadowing: 1) non-overlapping dual shadowing, and 2) overlapping dual shadowing.

Non-Overlapping Dual Shadowing

In non-overlapping dual shadowing, the downstream whisker is shadowed by two whiskers (j and k) whose shadows do not overlap on the whisker (Fig. 6.7a). We therefore treat each signal effect ($M_{i,j}$, $M_{i,k}$) independently when calculating the total magnitude effect on the downstream whisker i (M_i):

$$M_i = 1 - (1 - M_{i,j}) - (1 - M_{i,k}) \tag{6.9}$$

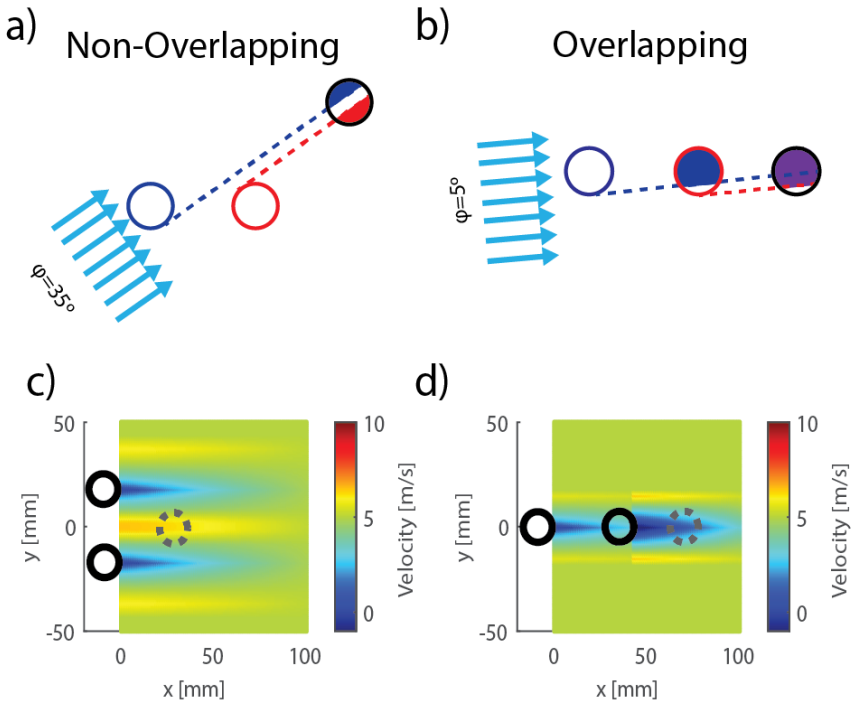

Figure 6.7: a) In non-overlapping occlusion, two shadows are cast by two separate whiskers onto a single downstream whisker. The downstream whisker feels the effect of both whiskers but never receives more shadowing than it would in a single whisker 100% occlusion case. b) In overlapping occlusion, two whiskers are shadowed. Here, the most upstream whisker (blue) casts a shadow on two downstream whiskers (red and black). The red whisker is also upstream from the black whisker, leading it to cast its own shadow. Our model demonstrates the expected sensed flow of whiskers at different x and y positions in cases of c) non-overlappingshadowing and d) overlapping shadowing. Our model shows that the shadowing and velocity effect can be magnified in the overlapping case. Compared to the model shown in Fig. 6.6c, the shadowed area (near 0 velocities) area is much larger, as are the zones where the velocity speed increases on the outside of the whisker.

Overlapping Dual Shadowing

By contrast, in overlapping dual shadowing, one of the whiskers shadowing the downstream whisker is already shadowed itself (Fig. 6.7b). In that case, the ANSYS model demonstrated that the overlapping shadow can be more significant than shadows cast by a single whisker. For this reason, we chose to model a downsteram whisker experiencing overlapping dual shadowing as related to the upstream whisker's M value. This model design decision makes it important to solve for the shadowing affects from the most upstream whisker to the most downstream whisker so the algorithm can have the whisker's magnitude ratios (M_j,M_k) for eqn. 6.10

(Fig. 6.7d).

$$M_i = 1 - (1 - M_{i,k}) - (1 - M_{i,j} * M_k) \tag{6.10}$$

6.3.5 Dual Airflows

A significant advantage of flow shadowing is the ability to discern multiple airflows present on the whisker array. The previous models were for a single airflow incident on the whiskers. To model the response from two different airflows, we assume that the total response of a whisker sensor is the combination of responses from each individual airflow on the whisker, including shadowing.

$$B_i = \sum_{Flow=1}^{2} M_{i,a} * \hat{m} * v_a^2 \tag{6.11}$$

6.3.6 Combined Model

Order is critical to correctly combining the equations we developed to estimate the sensor response. Whiskers closer to a flow source are not modeled to be affected by flow shadowing from the whiskers behind them. Algorithm 3 represents how the equations from the previous sections are combined to estimate $\overrightarrow{B}$ for each whisker from one or two known flow vectors.

6.3.7 Model Validation

The accuracy of Algorithm 3 under single flow was experimentally tested on arrays of three and four whiskers rotated between 0° and 180°. One example is shown in Fig. 6.8. In the pictured test, four whiskers are rotated relative to a flow source. While the whiskers rotate, three are shadowed, and two whiskers experience overlapping shadows (whiskers 6 and 8). The shadowing on whiskers 6 and 8 are mirrors of each other because of the array shape symmetry. The root mean square percent

Algorithm 3 Estimating Sensor Response to Known Airflow Vector(s)

Known Variables:
$F \leftarrow$ Number of Flow Sources
$n \leftarrow$ Number of Whiskers
$x, y \leftarrow$ global positions of whiskers in the array
I $\leftarrow$ indices of whiskers from upstream to downstream (F x n)
for $a \leftarrow 0$ to F **do**
    for $l \leftarrow 0$ to n **do**
        $i \leftarrow I[a, l]$ ▷ Most Upstream First
        $M_{i,a} \leftarrow 1$ ▷ Solve Starts from 1
        for $k \leftarrow 0$ to $l - 1$ **do** ▷ Only look upstream
            $j \leftarrow I[a, k]$
            $M_{i,j,a} = f(s_{i,j}, \omega_{i,j}, \varphi_a)$ ▷ eqn.: 6.6,6.7,6.8
            if $M_{i,j,a} \neq 1$ **then**
                $M_{i,a} = M_{i,a} - (1 - M_{i,j,a} * M_{j,a})$ ▷ 6.9,6.10
            end if
        end for
    end for
    $B_{i,a,x} = m_{i,x} * M_{i,a} * cos(\varphi_a) * v_a^2$ ▷ eqn.: 6.3,6.4,6.1
    $B_{i,a,y} = m_{i,y} * M_{i,a} * sin(\varphi_a) * v_a^2$ ▷ eqn.: 6.3,6.4,6.1
end for
$B_{i,x} = \sum_{a=0}^{F-1} B_{i,a,x}$ ▷ eqn.:6.11
$B_{i,y} = \sum_{a=0}^{F-1} B_{i,a,y}$ ▷ eqn.:6.11

error (RMSPE) between the data shown and the model was 14% and a test of three had a RMSPE of 15%.

6.4 Methods: Sensing Two Flows

The ultimate goal of this work is to use measured signals from the flow shadowing array to correctly solve for the airflow velocity(s), v, and heading(s) φ incident on the whisker array. In this paper, we assume that we know the number of airflows, and if there are two airflows, we know one of the airflows (e.g., the velocity of the drone). For both single and dual flow scenarios, we compare estimates of the flow velocity and heading generated from two algorithms (Net Vector and Look Up Table). Both algorithms use the whiskers' magnetic field signals as inputs. In addition, both methods are velocity invariant, and we estimate the velocity of the airflow, $\hat{v}$ only after solving for the airflow heading $\hat{\varphi}$.

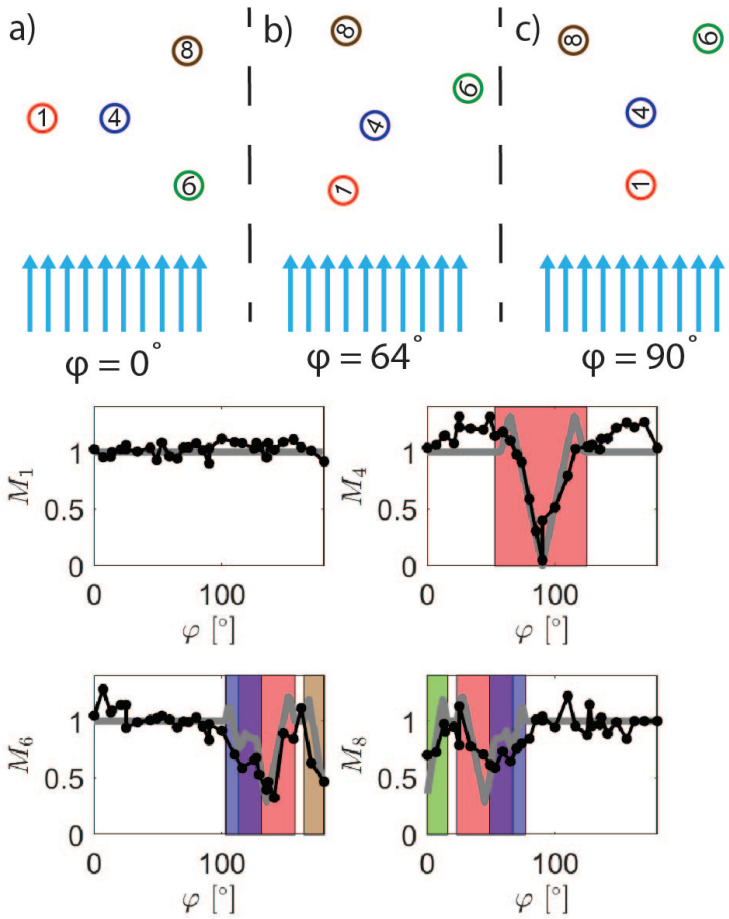

Figure 6.8: Four whiskers placed on a NEMA 17 motor are spaced in the configuration shown in a). As the motor rotates, the whiskers travel into and out of each others shadow. The modeled (gray) and experimental (black) signal are shown for each whisker in the graphs below the visualization of the rotation in a-c.

6.4.1 Net Vector

This method is a modified version of flow estimation used in previous work [35]. To estimate the flow direction, x and y components of the normalized magnetic field signals are summed together. Because we use the normalized magnetic field signals, this results in more weight accorded to the upstream whiskers for predicting $\hat{\varphi}$. The $\hat{v}$ is the average velocity predicted from the strongest signals of $\sqrt{n}$, where n is the number of whiskers in the array. For an array with a single whisker, this equation is no different from Eqn. 6.3. For multiple whiskers spaced far enough apart that no shadowing occurs, this equation will result in the average prediction from all n

whiskers. The velocity estimate $\hat{v}$ is the average velocity predicted from Eqn. 6.2.

$$\hat{\varphi_{net}} = \arctan(\frac{\sum_{i=0}^{n} B_x}{\sum_{i=0}^{n} B_y}) \tag{6.12}$$

6.4.2 Look Up Table

The look up table algorithm estimates $\hat{\varphi}$ by considering each whisker signal's relative magnitude compared to the array's maximum signal. We generate the look up table using our model and Algorithm 3 with a 1° resolution for each whisker in the array, resulting in a 360 x n x 2 look up table. Because our model has M values greater than 1 we need to normalize each of the 360 rows so the maximum absolute signal strength in the row is 1. This same normalization is preformed to any new experimental data collected so both the look up table and experimental data contain whisker array values between -1 and 1. We can then use this look up table in Algorithm 4.

Algorithm 4 Predicting $\hat{\varphi}$ using a Look Up Table

$LU \leftarrow$ Look-Up Table ▷ 360 x n x 2 Array
$B_{norm} = \frac{[B_{x0},B_{y0}....B_{xn},B_{yn}]}{max(abs([B_{x0},B_{y0}....B_{xn},B_{yn}])}$ ▷ n x 2 Array
$Dist = \sum_{axis=2,3}(LU - B_{norm})^2$ ▷ 360 x 1 Array
$\hat{\varphi} = argmin(Dist)$
$\hat{v} = \sqrt{median(\frac{B}{LU[\varphi,:,:]})}$

6.5 Results: Sensing Two Flows

6.5.1 Validation Data Sources

The algorithms to convert sensor signals to airflow vectors were validated using two methods: 1) simulated data, and 2) experimental data. Using Algorithm 1 3, we created expected array magnetic field signals for different whisker arrays in response to flow vectors whose velocity and flow heading were randomly selected from the test space. The simulated data had Gaussian noise added to the magnetic field

responses of ± 1 mT, which was found to be the approximate Root Mean Square Error between the model and the experimental data in Fig. 6.8. The algorithms are further tested on experimental data previously collected from a four whisker array arranged in a 2x2 grid [99].

In addition, we also provided a baseline comparison using four whiskers with a large enough separation so that no flow shadowing would occur. These four whiskers were placed on individual NEMA 17 motors and rotated in increments of 1.6° in front of the fan (Fig. 6.9).

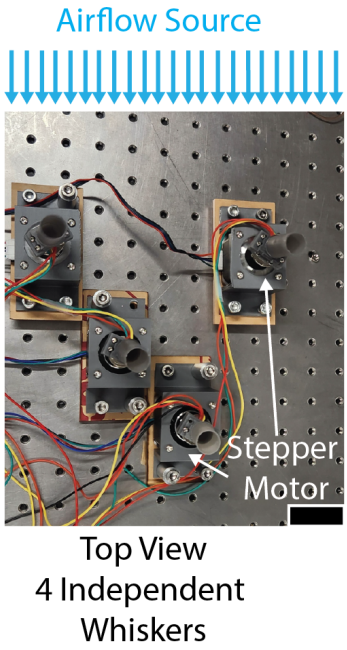

Figure 6.9: Experimental Test Setup: Four whisker sensors are placed on four NEMA 17 motors in order to measure their response to airflow without any flow shadowing affects. Scale bar represents 40 mm

6.5.2 Predicting a Single Airflow

We found the flow shadowing array with our updated algorithm could predict the heading of a single flow with an RMSE of 3.7°. This accuracy is comparable to the baseline of four whiskers, which could collectively predict the heading of flow with a Root Mean Square Error (RMSE) of 3.4°. The Look Up table algorithm was the better solver for the flow shadowing array than the net vector method because it could use the shadowing as insight into the flow source.

Despite similar prediction errors, the individual whiskers and the densely packed array both have their benefits. The four independent whiskers do not require a large specific area but cannot get closer together than 78 mm; as we have shown, there will be flow shadowing effects even at that spacing. The four-whisker flow shadowing array must exist in one 60x60 mm^2 square area, which is a more rigid requirement but allows the flow sensing to be confined to a more compact area which may be more important on a drone. The modeled and experimental results of predicting velocity and flow from a single airflow are shown in Tables 6.2 and 6.3 respectively.

Table 6.2: Flow Heading RMSE Across Single Flow Trials

	Net Vector	Look Up Table
Single Whisker	5.3°	–
Baseline: 4 Independent Whiskers	3.4°	–
Simulated 4 Whiskers	2.8°	3.0°
Experimental Results 4 Whiskers	16.6°	3.7°
Simulated 9 Whiskers	2.4°	2.3°

Table 6.3: Velocity RMSE Across Single Flow Trials

	Net Vector	Look Up Table
Single Whisker	$0.51\,\mathrm{m\,s^{-1}}$	–
Simulated 4 Whiskers	$0.10\,\mathrm{m\,s^{-1}}$	$0.16\,\mathrm{m\,s^{-1}}$
Experimental Results 4 Whiskers	$0.58\,\mathrm{m\,s^{-1}}$	$0.61\,\mathrm{m\,s^{-1}}$
Simulated 9 Whiskers	$0.19\,\mathrm{m\,s^{-1}}$	$0.10\,\mathrm{m\,s^{-1}}$

The gap between the model predicted and experimental accuracy of the flow shadowing array is minimal, indicating the model may be a good predictor for the look-up table performance. However, the gap between the solver on the modeled data and experimental data was much more substantial for the Net Vector method. One hypothesis for this larger gap is that the heavy oscillations induced in the downstream whiskers, which we have previously seen as a result of the shadowing phenomenon [99], increase the noise on the downstream whisker significantly which has a disproportionate effect on the net vector solver method. Both the single whisker and the flow shadowing method did poorly at predicting the flow speed.

Future work should continue to explore improvements to the algorithm methodology.

6.5.3 Predicting Dual Flow

Unsurprisingly, there is more noise in the sensor signal when there are two flow sources compared to one. The RMSE for the experimental and modeled data resulting from two flows can be found in the tables below:

Table 6.4: Flow Heading RMSE For Second Flow

	Net Vector	Look Up Table
Single Whisker	16.2°	–
Simulated 4 Whiskers	3.0°	3.2°
Experimental Results 4 Whiskers	33.3°	5.3°
Simulated 9 Whiskers	2.2°	2.0°

Table 6.5: Flow Velocity RMSE For Second Flow

	Net Vector	Look Up Table
Single Whisker		–
Simulated Four Whiskers	$0.17\,\mathrm{m\,s^{-1}}$	$0.11\,\mathrm{m\,s^{-1}}$
Experimental Results Four Whiskers	$1.08\,\mathrm{m\,s^{-1}}$	$1.04\,\mathrm{m\,s^{-1}}$
Simulated Nine Whiskers	$0.24\,\mathrm{m\,s^{-1}}$	$0.11\,\mathrm{m\,s^{-1}}$

For the array of four, both the model and the experimental results indicated a modest increase in the RMSE for predicting the φ. This analysis was performed on the same data as the data used to make Table I in [99]. In that publication the RMSE for predicting φ_2 spanned between 8.9° and 30.5° demonstrating the significant improvement the updated model yields in second flow source prediction. Here, we see a marked improvement in predicting the direction of the second flow source within 5.3° for the same data.

Our algorithms were significantly less accurate in predicting the velocity from the old experimental data compared to predicting flow heading. One of the reasons we believe the velocity prediction was so inaccurate was the test set up. The authors want to caution future researchers against using the test setup shown in [99]. There, we used two fans to simulate the flows. We recommend that future work use a

moving platform and one external flow source, as we do for the final section of this work. This recommendation is because when the authors switched to a larger fan the potential for two external flows to mix became a much more glaring issue with the prior test setup.

6.6 Flow Shadowing on a Drone

6.6.1 Experimental SetUp

Here, we test a flow shadowing array on a drone for the first time. A 2x2 array with the same parameters as [99] array was placed on a DJI Tello quadrotor (Fig. 6.9b). Instead of an Arduino Uno the I2C Mux was connected to a SEED Studio BLE Sense board. Data was collected and saved on a SD Card via a MicroSD card breakoutboard. The SD Card collected data at 40 Hz. The tests were performed in a 10 m x 10 m indoor motion capture arena using 24 Optitrack PrimeX 41 cameras. The same fan as had been previously used for benchtop tests was also placed in the drone arena to collect flow signals. The signal processing was done offline.

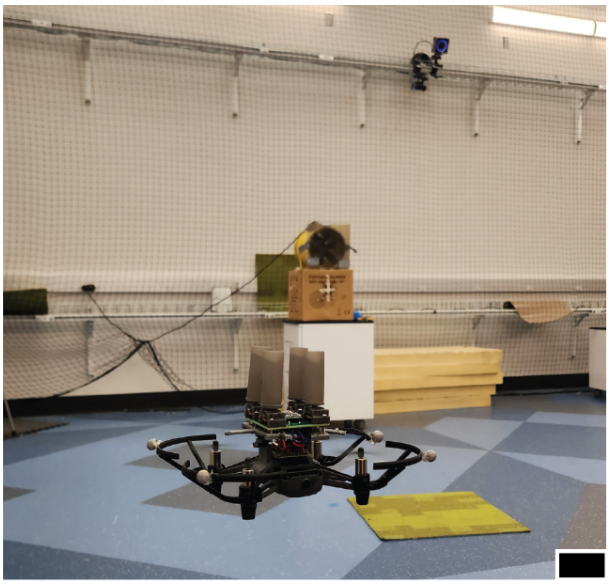

Figure 6.10: Experimental Test Setup: To test dual flow, a 2 x 2 array attached to a DJI Tello drone flies around a room with an airflow source. Scale bar is 40 mm.

6.6.2 Result

As the drone flies around the drone cage it travels in and out of the fan flow. An example of a drone entering the flow field is shown in Figure 6.11b. In the selected data, we have shown that shadowing occurs in two ways. First, the drone's motion creates dominant signals on the orange and blue whiskers. The navy blue whisker is the first to show a response to the fan, with the cyan whisker reaching the fan's airflow about 0.4 s later. The delay is a first for flow shadowing because, in all previous examples, we could assume the airflow was the same for all whiskers on the array. The dip in the velocity flow measured by the orange signal is not the flow mixing but the drone slowing down as it enters the flow field because our quadrotor must slow down to maintain stable flight in the wind.

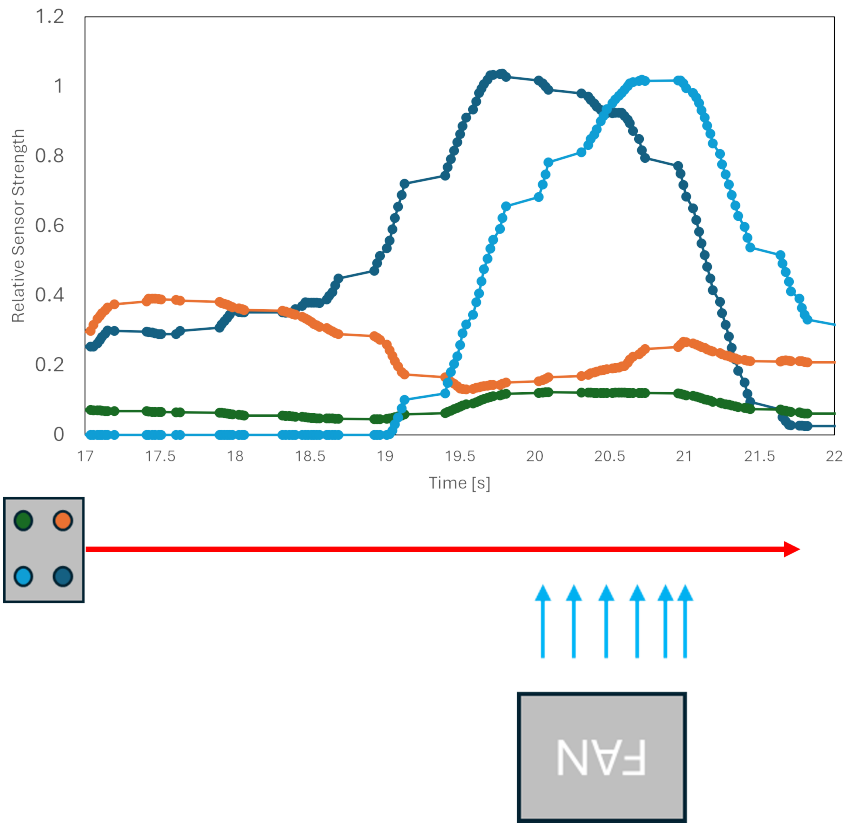

Figure 6.11: a) A DJI Tello drone performs casting motion in front of a fan flow source, so the flow shadowing array is subject to moments of single and dual flow. b) One instance of the wind flow field is shown where the whiskers in the configuration are shown on the x-axis as they pass in front of a fan flow source.

6.7 Discussion and Conclusion

Here we advance our understanding of the flow shadowing phenomenon from the methodology seen in [99] to a system of equations that can be generalized to/ verified on a larger variety of arrays. The improved model allowed us to consider both the strength and direction of signals in our new solver, improving the flow heading estimations on the same data set used in [99].

As part of this work, we discovered the pitfalls of simulating flow shadowing on a benchtop with two flow sources. Subsequently, we demonstrate the flow shadowing phenomenon on a drone, the first work demonstrating a mechanical sensor approach for dual-flow detection. The benefit of mechanical sensors is that they are more generalizable than models trained on specific drones or that incorporate the physics of specific drone drag. The adaptability is demonstrated by the whisker array that works both on the benchtop and on the quadrotor. Working without knowledge of the specific quadrotor to which it is attached decreases the labor in new system integration.

We expect this work can be pushed further by better models of the flowshadowing phenomenon and larger arrays. There are similarities between the flowshadowing we demonstrate here and work modeling flow through dense arrays of cricket hairs [128]. Using our models and others to improve the complexity strategically could potentially push the abilities of the array of whiskers, possibly sensing flow shadowing in 3D or elucidating the causal flows more accurately.

The work we have done here begins to enter into the complex aerodynamics surrounding drone flight. As evidenced by the testing quadrotor slowing down to stabilize in wind flow, wind flow is a challenge for drone stability. As research progresses on the mitigation of steady / semi-steday flows, more unstable flows will be one of the next challenges [129, 130]. The more improvements we can make to drone environment awareness, the better-equipped control algorithms will be to achieve their objective despite adverse environmental conditions.

Chapter 7

Conclusions

7.1 Summary of contributions

Whisker-inspired sensors can fill gaps in robotic systems' perception, making the robot more aware of, and safer in, its environment. However, for the whisker-inspired sensors to achieve their perception potential, they must function well outside of the controlled lab environment. In this work, we develop whisker-inspired sensors that maintain or improve upon prior whisker-inspired sensor perception ability while also being better equipped to interpret the variety of stimuli that occur in unstructured environments.

First, I demonstrate a mitigation strategy to overcome imprecise mapping during whisker contact with compliant surfaces or during slip. Most radial contact algorithms make assumptions about the type of contact the whisker is undergoing (e.g., small bend, rigid surface, no slipping). If these assumptions are not verified during the application, the user risks making imprecise mappings or having overconfidence in the wrong estimates. In Chapter 2, I demonstrate the benefit of using two radial contact distance estimation algorithms to quantify confidence in a contact point estimation. As long as the two algorithms do not make the same assumptions about contact, one algorithm should be able to identify the radial contact distance successfully. I demonstrate the usefulness of this methodology using a novel sensor I developed by mapping surfaces despite the whisker slipping during contact.

Second, I improved sensor robustness to multiple stimuli which caused whisker response. In Chapter 3, we talked about three types of mechanical stimuli: contact, airflow, and robot body motion. These three stimuli can occur in most terrestrial whisker applications. Through experimental tests, I demonstrated that each stimulus had characteristically different sensor responses on a whisker sensor. For example, whisker bodies undergoing airflow tend to oscillate around a set deflection magnitude, whereas contact tends to have no oscillations. These results also agree with other published papers which measure flow [35, 107] and contact [52]. However, our sensor was the first to apply these characteristic differences to an algorithm to differentiate the three stimuli. The final contribution was to show that applying this method does not require the assumption of a single stimulus. Simultaneously identifying two stimuli is possible when considering the sensor response of the entire array. Because airflow and robot motion are global stimuli, they should affect the whole array uniformly; this fact can make it simpler to identify contact through large deviations from the array response.

Third, I show how whiskers with an asymmetric whiskers cross-section can improve the detection of the flow heading and flow velocity. In Chapter 4 we talk about how whiskers with asymmetric cross-sections are asymmetrically sensitive to airflow from different headings. We further show that specific offsets of whiskers can illuminate the causal flow and/or indicate that there are two flow sources present like drag from drone motion and wind.

My last contribution takes the identification of two flow sources further by quantifying the two flow sources. In the sensor arrays discussed in Chapter 5 and 6, the whiskers are densely packed, creating a phenomenon called flow shadowing. The dense packing prevents air from traveling freely through the array, creating a heading-dependent symmetric sensitivity similar to that of asymmetric whiskers. This dense packing allows us to separate the effect of two flow sources for the first time on a drone.

7.1.1 Completed Publications

1. Imamura, T.*, **Kent, T. A.***, Taylor B., Bergbreiter, S. (2025) Measuring DNA Microswimmer Locomotion in Complex Flow Environments. IEEE International Conference on Robotics and Automation (ICRA) **(Under Review)**

2. **Kent, T. A.**, & Bergbreiter, S. (2024). Flow Shadowing: A Method to Detect Multiple Flow Headings using an Array of Densely Packed Whisker-inspired Sensors. IEEE International Conference on Robotics and Automation (ICRA)

3. **Kent, T. A.**, Emnett, H., Babaei, M., Hartmann, M. J., & Bergbreiter, S. (2023). Identifying Contact Distance Uncertainty in Whisker Sensing with Tapered, Flexible Whiskers IEEE International Conference on Robotics and Automation (ICRA)

4. **Kent, T. A.**, Kim, S., Kornilowicz, G., Yuan, W., Hartmann, M. J., & Bergbreiter, S. (2021). Whisksight: A reconfigurable, vision-based, optical whisker sensing array for simultaneous contact, airflow, and inertia stimulus detection. IEEE Robotics and Automation Letters, 6(2), 3357-3364.

7.1.2 Workshop Presentations

1. **Kent, T. A.**, Kim, S., Babaei, M., Emnett, H., Hartmann, M. J., & Bergbreiter, S. Asymmetric Mechanosensing for Uncertainty Reduction in Bio-Inspired Flight Workshop at ICRA 2024

2. **Kent, T. A.**, Kim, S., Babaei, M., Emnett, H., Hartmann, M. J., & Bergbreiter, S. Designing Whisker Sensors for Noisy Environments. Workshop at Robotics System and Sciences 2022

7.1.3 Future Publications

1. Kent, T. A., Thomas, L., & Bergbreiter, S. Asymmetric Whisker Cross Sections: A Method to Enhance Wind Sensing on Drones **(In preparation for Advanced Intelligent Systems)**

2. Kent, T. A., Thomas, L., & Bergbreiter, S. Flow Shadowing: Detecting Wind on a Moving Drone using a densely packed array of Whisker-Sensors **(In preparation for the Robotics Systems and Sciences Conference)**

3. Wang, T*., **Kent, T. A.***, & Bergbreiter, S. (2023). Design of whisker-inspired sensors for multi-directional hydrodynamic sensing. arXiv preprint arXiv:2307.09569 **(In preparation for Frontiers in Robotics)**

7.2 Take Aways

Given the substantial difference between biological creatures and robots, it is unsurprising that the engineered whiskers we developed deviate significantly from the source of their biological inspiration. Even with engineered whiskers that are far from biomimetic, our systems benefited from ideas inspired by biology: comparative signals, asymmetry, and array synergy were key to the success of the work in my thesis.

There is significant evidence that comparative signals are advantageous biologically and in engineering. For one, they are often faster than signal filtering and noise [131]. Here, too, we found that when two signals were expected to be the same, significant differences told us about the environment. In Chapter 2, deviations in signal predicted compliant surfaces or whisker slip. In Chapter 3, they allowed us to differentiate contact from an array of whiskers experiencing airflow. In Chapter 4, deviations in signal predicted a second flow source.

Asymmetry was also a key asset to our work. For many robotic platforms, especially aerial ones, general sensors capable of sensing many things at once are preferred because fewer sensors can result in lower weight and lower cost. However,

more general sensors often come with a trade-off in computation; if an IMU can sense signals caused by 6+ sources, there now needs to be an algorithm to estimate the source of an IMU signal. Cameras are another general sensor that requires extensive computation to interpret correctly. By contrast, specialized mechanosensors can have specific mechanical properties that allow them to respond strongly to specific stimuli while rejecting similar stimuli. We found the benefits of asymmetry particularly interesting in our work on flow sensing in Chapters 4, 5 and 6.

Array synergy, the idea that an array of whisker sensors can outperform a group of individual whiskers, was the confluence of asymmetry and comparative signals. In Chapter 3, comparing a single whisker response to the average sensor response allowed us to identify contact during airflow. In that chapter, the different stimuli caused the different responses. In Chapters 4, 5 and 6, we designed the array so that different whiskers would have their signal response to illuminate the causal flow or flow(s).

7.3 Future Outlook

The gap between whisker-inspired and natural whisker-sensing abilities is still quite large. Future research will need to continue to improve the sensors. One of the best ways to find the gaps engineered sensors will need to fill is to consider potential applications. In the following sections, I briefly discuss a few areas for sensor improvement and interesting application areas.

7.3.1 Contact whiskers

With a single whisker, we identified algorithm failure caused by whisker contact with a compliant surface. An array of whiskers, potentially with different compliances would be more similar to rat whiskers [6]. A larger array with variations in whisker sensors has the potential to map not only the environment but compliance in the environment. In outdoor scene mapping this could help distinguish a branch that a

terrestrial robot could push past from a tree trunk which could damage the robot structure if it tried to push it aside. Compliance mapping has been done with rigid tactile structures, but the whisker is the best robotic tactile sensor I have seen thus far for non-damaging contact with an environment.

This aspect of whisker tactile mapping translates well to commercial interests. As robots are brought into the home and trusted around more vulnerable creatures (children, pets), safety is increasingly important. Contact between whiskers and the environment represents a method for robots to do brush-by contact [132] or emergency proximity sensing in a much safer way than many other sensing methods. Whiskers are especially advantageous because they are a cheaper sensor than other tactile sensors.

7.3.2 Multi-stimuli mapping

Simultaneous sensing of airflow and contact on a drone is a challenge that is just starting to gain interest [38, 60, 133]. One challenge for a contact whisker on the drone is the considerable amount of signal noise from drone motion and drone hovering on the whisker [134]. If this challenge can be overcome on a moving drone, contact mapping without applying large forces on the drone would be beneficial. Surface mapping can provide information for control researchers toward perching and payload retrieval. Another key application area could be environmental monitoring and exploration by drones of low-light areas such as caves.

7.3.3 Airflow Sensing

The work we put forward in Chapters 4, 5 and 6 provides foundational methodologies for improved flow sensing. Although asymmetry is useful, the whiskers chosen had sharp corners; airfoils could create the same asymmetry with considerably less vortex shedding. We also demonstrated only two whiskers paired together. There is evidence that more whiskers creates an interesting design challenge with the potential to further improve whisker-based flow sensing in flight.

Appendix A

Appendix 1

A.1 Introduction

The serpentine springs are an asset to several of the whisker sensors we present because of their predefined models, which convert deflections/ rotations into forces/ moments. The origional system of equations was presented in [53] and [52] was the first work to show the benefit of the springs for whisker sensors. The work is presented here to provide a more complete background on my implementation of the serpentine springs, not because I made any major advancements to the spring design.

In chapter 2, I implement acrylic serpentine springs to convert downward deflections and rotations into moments and forces at the whisker's base. I also benefit from the linear relationship between rotation and moments and deflections and axial force. In chapters 4 and 5, we use steel serpentine springs to convert the sensed rotations from the hall effect sensor into the drag force.

A.2 Theory

In Barillo et al.[53] they demonstrate that a serpentine spring is modelable as a series of cantilever beams. The system of equations that describes the set of cantilever beams compactly converts the rotation and deflection at the unconstrained end of the

serpentine spring into moments and forces at that same point (Figure Reference). When an object is suspended by multiple springs they forces at the end of each spring come together to calculate the forces on the object.

A.3 Equations

The sensors from chapter 2, 4 and 5 can all calculate the ϕ and θ rotations at the spring's center. For the spring math, ϕ and θ have to be converted into the rotations about the spring's axes, ϕ_x and ϕ_y (Eqns. A.1 and A.2). Rotations ϕ_x and ϕ_y cause equal but opposite deflections in the z-direction at opposing spring joints (Figure). In chapter 2 we also measure δ_z which is the total deflection of the system, therefore we represent the z deflection caused by rotation about the x and y axis as δ_x and δ_y respectively (equations A.3,A.4). The δ_x / δ_y are dependent on the distance the springs are from the center of rotation (p_w, p_t). Adding δ_z to δ_x and δ_y gives the total deflection at each joint. With the deflections and rotations, you can solve for the moments (m_n) and forces (f_n) at the end of each spring (Eqn. A.5, A.6). C is a matrix made up of the spring parameters in table 2.1 which describes the resistance to moments and forces at different points in the beam.

$$\phi_x = \arctan(\frac{sin(\phi)cos(\theta)}{cos(\phi)} \tag{A.1}$$

$$\phi_y = \arctan(\frac{sin(\phi)sin(\theta)}{cos(\phi)}) \tag{A.2}$$

$$\delta_x = p_w \tan(\phi_x) \tag{A.3}$$

$$\delta_y = p_t \tan(\phi_y)) \tag{A.4}$$

$$d = \begin{bmatrix} \phi_y & \phi_x & -\phi_y & -\phi_x \\ \phi_x & \phi_y & -\phi_x & -\phi_y \\ \delta_z - \delta_x & \delta_z - \delta_y & \delta_z + \delta_x & \delta_z + \delta_y \end{bmatrix} \tag{A.5}$$

$$\begin{bmatrix} m_{x1} & m_{y2} & -m_{x3} & -m_{y4} \\ m_{y1} & m_{x2} & -m_{y3} & -m_{x4} \\ f_{z1} & f_{z2} & f_{z3} & f_{z4} \end{bmatrix} = C^{-1} * d \tag{A.6}$$

The forces and moments can be recombinded into Moments about the x and y axis ($M-x$, M_y) and a downward force F_z. For some works the summation moment is more important than the component moment so the L2 norm can be taken of M_x and M_y.

$$M_x = \sum_{i=1}^{n} m_{xn} + b_h/2 * f_{z1} - b_h/2 * f_{z3} \tag{A.7}$$

$$M_y = \sum_{i=1}^{n} m_{yn} + b_w/2 * f_{z2} - b_w/2 * f_{z4} \tag{A.8}$$

$$F_z = \sum_{i=1}^{n} f_{zn} \tag{A.9}$$

$$M_b = \sqrt{M_x^2 + M_y^2} \tag{A.10}$$

$$M_d = \theta \tag{A.11}$$

Appendix B

Appendix 2

B.1 Defining Asymmetry

Here, we define asymmetry as the similarity between the applied flow signal (φ) and the sensed flow signal θ as measured by a root mean square error calculation.

Table B.1: Root Mean Square Error Between φ and θ

	Circle	Cross	Square	Triangle	Chevron
RMSE	11.4 °	9.1 °	20.3 °	38.4 °	31.7 °

More symmetric whiskers have almost linear θ vs φ curves Fig. B.1.

B.2 Sensor Characterization Curves

Each of the three whiskers tested per asymmetric cross-section have slightly different response curves (Fig. B.1. We expect this is due to differences in the manufacturing, especially inconsistencies in the spring manufacturing methodology.

However, the sensor itself remains consistent over five trials where each trial occurs at a different airflow (Fig. B.2). The F_u and F_v curves contain more directional information than the strength curve, so it is these curves that are used in the algorithms to predict flow heading.

B.3 Mixing Whiskers

One idea we had was that by having the signals of two different whisker shapes at various offsets, it might lead to better performance than matching two of the same whiskers. This prediction turned out to be false, as the best performance was still paired square whiskers.

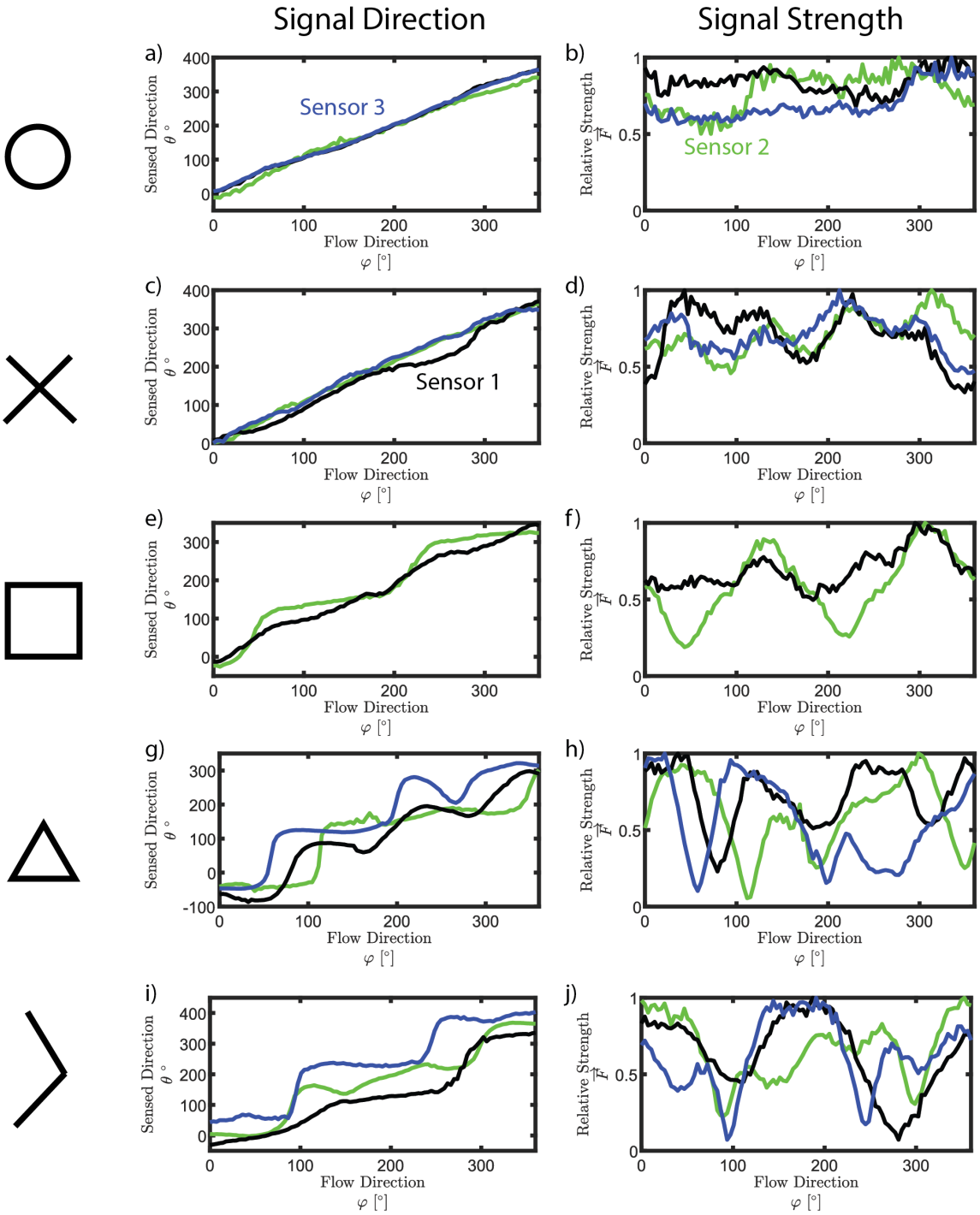

Figure B.1: For each of the three whiskers tested for each cross-section, there are small variations in their φ vs. θ and φ vs. $||B_2||$ curve.

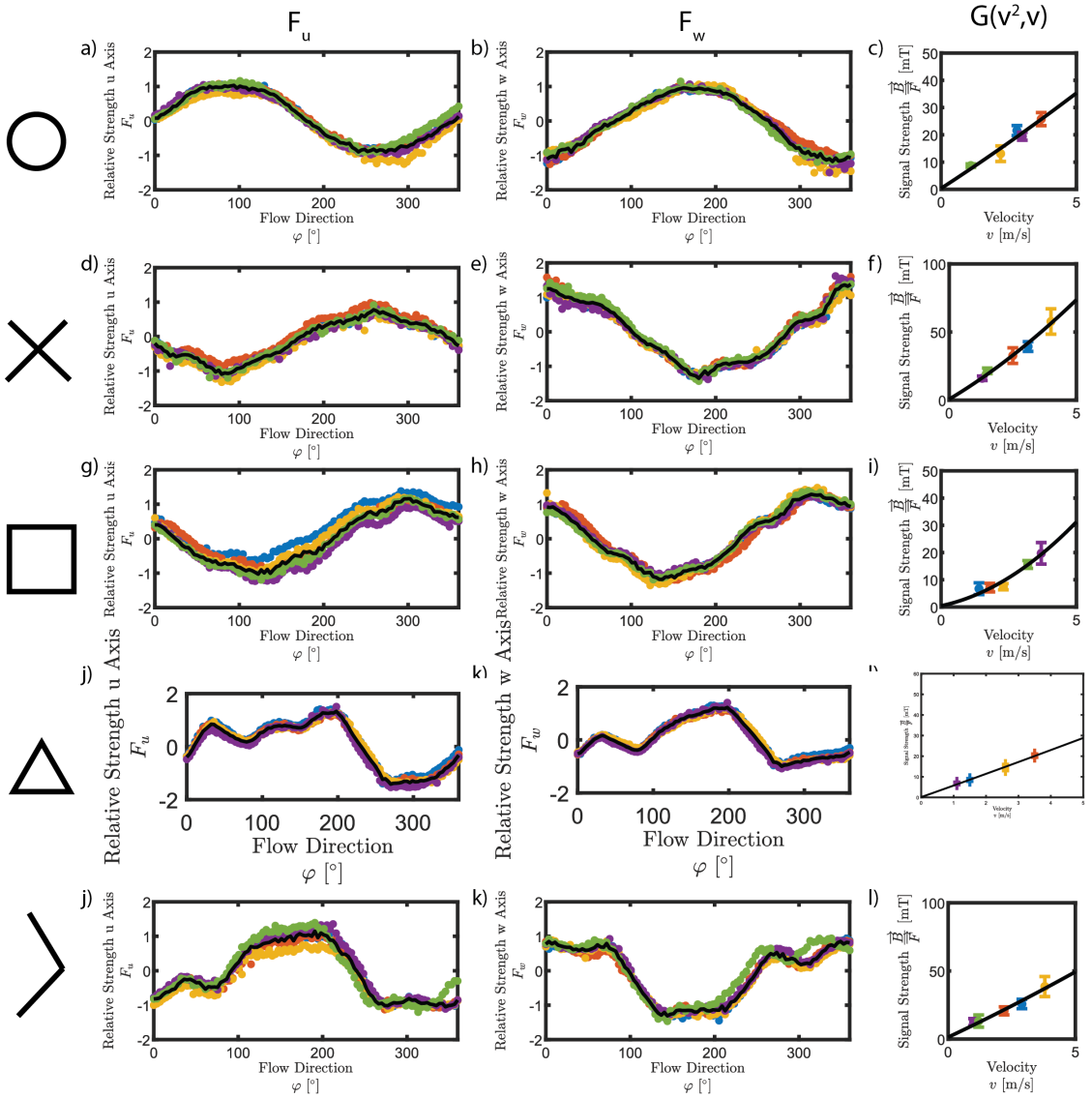

Figure B.2: Curves for one whisker of each sensor cross-section representing the models F_u and F_w and G curves.

Bibliography

[1] Alwynelle S Ahl. "The role of vibrissae in behavior: a status review". In: *Veterinary research communications* 10.1 (1986), pp. 245–268.

[2] Guido Dehnhardt et al. "Hydrodynamic trail-following in harbor seals (Phoca vitulina)". In: *Science* 293.5527 (2001), pp. 102–104.

[3] Susanne Sterbing-D'Angelo et al. "Bat wing sensors support flight control". In: *Proceedings of the National Academy of Sciences* 108.27 (2011), pp. 11291–11296.

[4] Brian W Quist and Mitra JZ Hartmann. "Mechanical signals at the base of a rat vibrissa: the effect of intrinsic vibrissa curvature and implications for tactile exploration". In: *Journal of neurophysiology* 107.9 (2012), pp. 2298–2312.

[5] Jonathan Cheung et al. "The sensorimotor basis of whisker-guided anteroposterior object localization in head-fixed mice". In: *Current Biology* 29.18 (2019), pp. 3029–3040.

[6] RA Kastelein and MA Van Gaalen. "The sensitivity of the vibrissae of a Pacific walrus (Odobenus rosmarus divergens) Part 1". In: *Aquatic Mammals* 14.3 (1988), pp. 123–133.

[7] H Hyvärinen et al. "Aquatic environment and differentiation of vibrissae: comparison of sinus hair systems of ringed seal, otter and pole cat". In: *Brain, behavior and evolution* 74.4 (2009), pp. 268–279.

[8] Yan SW Yu et al. “Whiskers aid anemotaxis in rats”. In: *Science advances* 2.8 (2016), e1600716.

[9] Alyxandra O Milne et al. “Pinnipeds orient and control their whiskers: a study on Pacific walrus, California sea lion and Harbor seal”. In: *Journal of Comparative Physiology A* 206 (2020), pp. 441–451.

[10] Xingwen Zheng et al. “Wavy Whiskers in Wakes: Explaining the Trail-Tracking Capabilities of Whisker Arrays on Seal Muzzles”. In: *Advanced Science* 10.2 (2023), p. 2203062.

[11] Wolf Hanke et al. “Harbor seal vibrissa morphology suppresses vortex-induced vibrations”. In: *Journal of Experimental Biology* 213.15 (2010), pp. 2665–2672.

[12] Yves Boubenec, Daniel E Shulz, and Georges Debrégeas. “Whisker encoding of mechanical events during active tactile exploration”. In: *Frontiers in behavioral neuroscience* 6 (2012), p. 74.

[13] Maysam Oladazimi et al. “Conveyance of texture signals along a rat whisker”. In: *Scientific reports* 11.1 (2021), pp. 1–16.

[14] Gongchao Liu et al. “Artificial Whisker Sensor with Undulated Morphology and Self-Spread Piezoresistors for Diverse Flow Analyses”. In: *Soft Robotics* 10.1 (2023), pp. 97–105.

[15] Heather Beem, Matthew Hildner, and Michael Triantafyllou. “Calibration and validation of a harbor seal whisker-inspired flow sensor”. In: *Smart Materials and Structures* 22.1 (2012), p. 014012.

[16] R Andrew Russell. “Using tactile whiskers to measure surface contours”. In: *Proceedings 1992 IEEE International Conference on Robotics and Automation*. IEEE Computer Society. 1992, pp. 1295–1296.

[17] Charles W Fox and Tony J Prescott. “Mapping with sparse local sensors and strong hierarchical priors”. In: *Conference Towards Autonomous Robotic Systems*. Springer. 2011, pp. 183–194.

[18] Joseph H Solomon and Mitra JZ Hartmann. "Radial distance determination in the rat vibrissal system and the effects of Weber's law". In: *Philosophical Transactions of the Royal Society B: Biological Sciences* 366.1581 (2011), pp. 3049–3057.

[19] Nhan Huu Nguyen, Trung Dung Ngo, Dinh Quang Nguyen, et al. "Contact distance estimation by a soft active whisker sensor based on morphological computation". In: *2020 8th IEEE RAS/EMBS International Conference for Biomedical Robotics and Biomechatronics (BioRob)*. IEEE. 2020, pp. 322–327.

[20] DaeEun Kim and Ralf Möller. "Biomimetic whiskers for shape recognition". In: *Robotics and Autonomous Systems* 55.3 (2007), pp. 229–243.

[21] Mathew H Evans et al. "Tactile discrimination using template classifiers: Towards a model of feature extraction in mammalian vibrissal systems". In: *International Conference on Simulation of Adaptive Behavior*. Springer. 2010, pp. 178–187.

[22] Mohammed Salman and Martin J Pearson. "Advancing whisker based navigation through the implementation of Bio-Inspired whisking strategies". In: *2016 IEEE International Conference on Robotics and Biomimetics (ROBIO)*. IEEE. 2016, pp. 767–773.

[23] Zihou Wei et al. "Development of an MEMS based biomimetic whisker sensor for tactile sensing". In: *2019 IEEE International Conference on Cyborg and Bionic Systems (CBS)*. IEEE. 2019, pp. 222–227.

[24] Chenlu Zhao, Qi Jiang, and Yibin Li. "A novel biomimetic whisker technology based on fiber Bragg grating and its application". In: *Measurement Science and Technology* 28.9 (2017), p. 095104.

[25] James F Wilson and Zhenhai Chen. "A whisker probe system for shape perception of solids". In: (1995).

[26] Lucie A Huet, John W Rudnicki, and Mitra JZ Hartmann. "Tactile sensing with whiskers of various shapes: Determining the three-dimensional location of object contact based on mechanical signals at the whisker base". In: *Soft robotics* 4.2 (2017), pp. 88–102.

[27] Makoto Kaneko, Naoki Kanayama, and Toshio Tsuji. "Active antenna for contact sensing". In: *IEEE Transactions on robotics and automation* 14.2 (1998), pp. 278–291.

[28] Charles W Fox et al. "Towards hierarchical blackboard mapping on a whiskered robot". In: *Robotics and Autonomous Systems* 60.11 (2012), pp. 1356–1366.

[29] Gregory R Scholz and Christopher D Rahn. "Profile sensing with an actuated whisker". In: *IEEE Transactions on Robotics and Automation* 20.1 (2004), pp. 124–127.

[30] Chenxi Xiao et al. "Active Multi-Object Exploration and Recognition via Tactile Whiskers". In: *arXiv preprint arXiv:2109.03976* (2021).

[31] Joseph H Solomon and Mitra J Hartmann. "Robotic whiskers used to sense features". In: *Nature* 443.7111 (2006), pp. 525–525.

[32] Mohammed Salman and Martin J Pearson. "Whisker-ratslam applied to 6d object identification and spatial localisation". In: *Conference on Biomimetic and Biohybrid Systems*. Springer. 2018, pp. 403–414.

[33] A.M.K. Dagamseh et al. "Engineering of biomimetic hair-flow sensor arrays dedicated to high-resolution flow field measurements". In: *SENSORS, 2010 IEEE*. 2010, pp. 2251–2254. DOI: 10.1109/ICSENS.2010.5690705.

[34] Junliang Tao and Xiong Bill Yu. "Hair flow sensors: from bio-inspiration to bio-mimicking—a review". In: *Smart Materials and Structures* 21.11 (2012), p. 113001.

[35] Suhan Kim et al. "A Whisker-inspired Fin Sensor for Multi-directional Air-flow Sensing". In: *IROS* (2020).

[36] Andrea Tagliabue et al. "Touch the Wind: Simultaneous Airflow, Drag and Interaction Sensing on a Multirotor". In: *arXiv preprint arXiv:2003.02305* (2020).

[37] Nathaniel Simon et al. "FlowDrone: wind estimation and gust rejection on UAVs using fast-response hot-wire flow sensors". In: *arXiv preprint arXiv:2210.05857* (2022).

[38] Teresa A Kent et al. "WhiskSight: A Reconfigurable, Vision-Based, Optical Whisker Sensing Array for Simultaneous Contact, Airflow, and Inertia Stimulus Detection". In: *IEEE Robotics and Automation Letters* 6.2 (2021), pp. 3357–3364.

[39] Joseph H Solomon and Mitra JZ Hartmann. "Extracting object contours with the sweep of a robotic whisker using torque information". In: *The International Journal of Robotics Research* 29.9 (2010), pp. 1233–1245.

[40] Hannah M Emnett, Matthew M Graff, and Mitra JZ Hartmann. "A novel whisker sensor used for 3d contact point determination and contour extraction". In: *Robotics: science and systems*. 2018.

[41] Nathan F Lepora, Martin Pearson, and Luke Cramphorn. "TacWhiskers: Biomimetic optical tactile whiskered robots". In: *2018 IEEE/RSJ International Conference on Intelligent Robots and Systems (IROS)*. IEEE. 2018, pp. 7628–7634.

[42] Martin J Pearson et al. "Simultaneous localisation and mapping on a multi-degree of freedom biomimetic whiskered robot". In: *2013 IEEE International Conference on Robotics and Automation*. IEEE. 2013, pp. 586–592.

[43] Peng Xu et al. "A triboelectric-based artificial whisker for reactive obstacle avoidance and local mapping". In: *Research* 2021 (2021).

[44] Charles Fox et al. "Tactile SLAM with a biomimetic whiskered robot". In: *2012 IEEE International Conference on Robotics and Automation*. IEEE. 2012, pp. 4925–4930.

[45] Mat Evans et al. "Whisker-object contact speed affects radial distance estimation". In: *2010 IEEE International Conference on Robotics and Biomimetics*. IEEE. 2010, pp. 720–725.

[46] Sven Hellbach, André Frank Krause, and Volker Dürr. "Feel like an insect: a bio-inspired tactile sensor system". In: *International Conference on Neural Information Processing*. Springer. 2010, pp. 676–683.

[47] Naohiro Ueno, Mikhail M Svinin, and Makoto Kaneko. "Dynamic contact sensing by flexible beam". In: *IEEE/ASME transactions on mechatronics* 3.4 (1998), pp. 254–264.

[48] Luis Mérida-Calvo, Daniel Feliu-Talegón, and Vicente Feliu-Batlle. "Improving the detection of the contact point in active sensing antennae by processing combined static and dynamic information". In: *Sensors* 21.5 (2021), p. 1808.

[49] David W Collinson et al. "Tapered polymer whiskers to enable three-dimensional tactile feature extraction". In: *Soft Robotics* 8.1 (2021), pp. 44–58.

[50] T.A. Kent. *Identifying-Contact-Distance-Uncertainty-in-Whisker-Sensing-with-Tapered-Flexible-Whiskers*. `https://github.com/TeresaAKent/Identifying-Contact-Distance-Uncertainty-in-Whisker-Sensing-with-Tapered-Flexible-Whiskers.git`. 2022.

[51] Simon Baker and Iain Matthews. "Lucas-kanade 20 years on: A unifying framework". In: *International journal of computer vision* 56.3 (2004), pp. 221–255.

[52] Suhan Kim et al. "A Magnetically Transduced Whisker for Angular Displacement and Moment Sensing". In: *2019 IEEE/RSJ International Conference on Intelligent Robots and Systems (IROS)*. IEEE. 2019, pp. 665–671.

[53] Giuseppe Barillaro et al. "Analysis, simulation and relative performances of two kinds of serpentine springs". In: *Journal of Micromechanics and Microengineering* 15.4 (2005), p. 736.

[54] Magdalena N Muchlinski et al. "Good vibrations: the evolution of whisking in small mammals". In: *The Anatomical Record* 303.1 (2020), pp. 89–99.

[55] Satomi Ebara et al. "Similarities and differences in the innervation of mystacial vibrissal follicle–sinus complexes in the rat and cat: a confocal microscopic study". In: *Journal of Comparative Neurology* 449.2 (2002), pp. 103–119.

[56] Mathew H Evans et al. "The effect of whisker movement on radial distance estimation: a case study in comparative robotics". In: *Frontiers in neurorobotics* 6 (2013), p. 12.

[57] Tony J Prescott, Mathew E Diamond, and Alan M Wing. *Active touch sensing*. 2011.

[58] Tareq Assaf et al. "Visual-tactile sensory map calibration of a biomimetic whiskered robot". In: *2016 IEEE International Conference on Robotics and Automation (ICRA)*. IEEE. 2016, pp. 967–972.

[59] Martin J Pearson et al. "Biomimetic vibrissal sensing for robots". In: *Philosophical Transactions of the Royal Society B: Biological Sciences* 366.1581 (2011), pp. 3085–3096.

[60] William Deer and Pauline EI Pounds. "Lightweight whiskers for contact, pre-contact, and fluid velocity sensing". In: *IEEE Robotics and Automation Letters* 4.2 (2019), pp. 1978–1984.

[61] Kuniharu Takei et al. "Highly sensitive electronic whiskers based on patterned carbon nanotube and silver nanoparticle composite films". In: *Proceedings of the National Academy of Sciences* 111.5 (2014), pp. 1703–1707.

[62] Benjamin Ward-Cherrier et al. "The tactip family: Soft optical tactile sensors with 3d-printed biomimetic morphologies". In: *Soft robotics* 5.2 (2018), pp. 216–227.

[63] Wenzhen Yuan, Siyuan Dong, and Edward H Adelson. "Gelsight: High-resolution robot tactile sensors for estimating geometry and force". In: *Sensors* 17.12 (2017), p. 2762.

[64] Thomas Feix, Ian M Bullock, and Aaron M Dollar. "Analysis of human grasping behavior: Object characteristics and grasp type". In: *IEEE transactions on haptics* 7.3 (2014), pp. 311–323.

[65] Anne En-Tzu Yang, Mitra JZ Hartmann, and Sarah Bergbreiter. "Contact-Resistive Sensing of Touch and Airflow Using A Rat Whisker". In: *2018 7th IEEE International Conference on Biomedical Robotics and Biomechatronics (Biorob)*. IEEE. 2018, pp. 1187–1192.

[66] Sean R Anderson et al. "Adaptive cancelation of self-generated sensory signals in a whisking robot". In: *IEEE Transactions on Robotics* 26.6 (2010), pp. 1065–1076.

[67] Akihiko Yamaguchi and Christopher G Atkeson. "Combining finger vision and optical tactile sensing: Reducing and handling errors while cutting vegetables". In: *2016 IEEE-RAS 16th International Conference on Humanoid Robots (Humanoids)*. IEEE. 2016, pp. 1045–1051.

[68] Kevin Vlack et al. "GelForce: a vision-based traction field computer interface". In: *CHI'05 extended abstracts on Human factors in computing systems*. 2005, pp. 1154–1155.

[69] David S Bolme et al. "Visual object tracking using adaptive correlation filters". In: *2010 IEEE computer society conference on computer vision and pattern recognition*. IEEE. 2010, pp. 2544–2550.

[70] Alan Lukezic et al. "Discriminative correlation filter with channel and spatial reliability". In: *Proceedings of the IEEE Conference on Computer Vision and Pattern Recognition*. 2017, pp. 6309–6318.

[71] Simon JD Prince. *Computer vision: models, learning, and inference*. Cambridge University Press, 2012.

[72] Kyle S. Severson et al. "Active Touch and Self-Motion Encoding by Merkel Cell-Associated Afferents". en. In: *Neuron* 94.3 (May 2017), 666–676.e9. ISSN:

08966273. DOI: 10.1016/j.neuron.2017.03.045. URL: https://linkinghub.elsevier.com/retrieve/pii/S0896627317302891 (visited on 10/16/2020).

[73] Avner Wallach, Knarik Bagdasarian, and Ehud Ahissar. "On-going computation of whisking phase by mechanoreceptors". en. In: *Nature Neuroscience* 19.3 (Mar. 2016), pp. 487–493. ISSN: 1097-6256, 1546-1726. DOI: 10.1038/nn.4221. URL: http://www.nature.com/articles/nn.4221 (visited on 10/16/2020).

[74] Yan S. W. Yu, Matthew M. Graff, and Mitra J. Z. Hartmann. "Mechanical responses of rat vibrissae to airflow". en. In: *The Journal of Experimental Biology* 219.7 (Apr. 2016), pp. 937–948. ISSN: 0022-0949, 1477-9145. DOI: 10.1242/jeb.126896. URL: http://jeb.biologists.org/lookup/doi/10.1242/jeb.126896 (visited on 10/16/2020).

[75] T.A. Kent. *WhiskSight*. https://github.com/TeresaAKent/WhiskSight. 2020.

[76] Samuel Ubellacker et al. "High-speed aerial grasping using a soft drone with onboard perception". In: *npj Robotics* 2.1 (2024), p. 5.

[77] Jiawei Meng et al. "On aerial robots with grasping and perching capabilities: A comprehensive review". In: *Frontiers in Robotics and AI* 8 (2022), p. 739173.

[78] Steffen Kirchgeorg and Stefano Mintchev. "HEDGEHOG: Drone perching on tree branches with high-friction origami spines". In: *IEEE Robotics and Automation Letters* 7.1 (2021), pp. 602–609.

[79] Ryan Kitchen et al. "Design and evaluation of a perching hexacopter drone for energy harvesting from power lines". In: *2020 IEEE/RSJ International Conference on Intelligent Robots and Systems (IROS)*. IEEE. 2020, pp. 1192–1198.

[80] Melanie J Anderson et al. "The "Smellicopter," a bio-hybrid odor localizing nano air vehicle". In: *2019 IEEE/RSJ International Conference on Intelligent Robots and Systems (IROS)*. IEEE. 2019, pp. 6077–6082.

[81] Benjamin Koger et al. "Multi-animal behavioral tracking and environmental reconstruction using drones and computer vision in the wild". In: *bioRxiv* (2022).

[82] Basaran Bahadir Kocer et al. "Forest drones for environmental sensing and nature conservation". In: *2021 Aerial Robotic Systems Physically Interacting with the Environment (AIRPHARO)*. IEEE. 2021, pp. 1–8.

[83] Aleix Paris, Andrea Tagliabue, and Jonathan P How. "Autonomous MAV landing on a moving platform with estimation of unknown turbulent wind conditions". In: *AIAA Scitech 2021 Forum*. 2021, p. 0378.

[84] Andrea Tagliabue. "Efficient Imitation Learning for Robust, Adaptive, Vision-based Agile Flight Under Uncertainty". PhD thesis. Massachusetts Institute of Technology, 2024.

[85] Teodor Tomić. *Model-based control of flying robots for robust interaction under wind influence*. Vol. 151. Springer Nature, 2022.

[86] Patrick P Neumann and Matthias Bartholmai. "Real-time wind estimation on a micro unmanned aerial vehicle using its inertial measurement unit". In: *Sensors and Actuators A: Physical* 235 (2015), pp. 300–310.

[87] Andrea Tagliabue and Jonathan P How. "Airflow-Inertial Odometry for Resilient State Estimation on Multirotors". In: *2021 IEEE International Conference on Robotics and Automation (ICRA)*. IEEE. 2021, pp. 5736–5743.

[88] Prasanna K Routray et al. "Separating Intrinsic and Extrinsic Responses of Whisker Sensors Using Accelerometer". In: *IEEE Sensors Journal* (2024).

[89] Alex C Hollenbeck et al. "Bioinspired artificial hair sensors for flight-by-feel of unmanned aerial vehicles: a review". In: *AIAA Journal* 61.12 (2023), pp. 5206–5231.

[90] Susanne J Sterbing-D'Angelo et al. "Functional role of airflow-sensing hairs on the bat wing". In: *Journal of neurophysiology* 117.2 (2017), pp. 705–712.

[91] Christoph Brücker, Daniel Schlegel, and Michael Triep. "Feather vibration as a stimulus for sensing incipient separation in falcon diving flight". In: *Natural Resources* 7.07 (2016), pp. 411–422.

[92] Toshiyuki Nakata et al. "Aerodynamic imaging by mosquitoes inspires a surface detector for autonomous flying vehicles". In: *Science* 368.6491 (2020), pp. 634–637.

[93] Jeffrey M Camhi. "Yaw-correcting postural changes in locusts". In: *Journal of Experimental Biology* 52.3 (1970), pp. 519–531.

[94] Kotaro Haneda et al. "Compact Sphere-Shaped Airflow Vector Sensor Based on MEMS Differential Pressure Sensors". In: *Sensors* 22.3 (2022), p. 1087.

[95] Zhengnong Li et al. "A Study on Measuring the Wind Field in the Air Using a multi-rotor UAV Mounted with an Anemometer". In: *Boundary-Layer Meteorology* 188.1 (2023), pp. 1–27.

[96] Paolo Bruschi et al. "Wind speed and direction detection by means of solid-state anemometers embedded on small quadcopters". In: *Procedia Engineering* 168 (2016), pp. 802–805.

[97] Junhao Yu, Wusheng Chou, and Yongfeng Rong. "Wind Estimation for Multirotor UAV Control based on Surface Pressure Distribution". In: *2024 5th International Conference on Electronic Communication and Artificial Intelligence (ICECAI)*. IEEE. 2024, pp. 494–499.

[98] Haowen Yu, Xianqi Liang, and Ximin Lyu. "DOB-based Wind Estimation of A UAV Using Its Onboard Sensor". In: *arXiv preprint arXiv:2409.01549* (2024).

[99] Teresa A Kent and Sarah Bergbreiter. "Flow Shadowing: A Method to Detect Multiple Flow Headings using an Array of Densely Packed Whisker-inspired

Sensors". In: *2024 IEEE International Conference on Robotics and Automation (ICRA)*. IEEE. 2024.

[100] Tuo Wang, Teresa A Kent, and Sarah Bergbreiter. "Design of whisker-inspired sensors for multi-directional hydrodynamic sensing". In: *arXiv preprint arXiv:2307.09569* (2023).

[101] Jeffrey M Camhi. "Sensory control of abdomen posture in flying locusts". In: *Journal of Experimental Biology* 52.3 (1970), pp. 533–537.

[102] Chenyao Wang et al. "Embodied airflow sensing for improved in-gust flight of flapping wing MAVs". In: *Frontiers in Robotics and AI* (2022), p. 338.

[103] Sawyer B Fuller et al. "Controlling free flight of a robotic fly using an onboard vision sensor inspired by insect ocelli". In: *Journal of The Royal Society Interface* 11.97 (2014), p. 20140281.

[104] Sawyer Fuller, Zhitao Yu, and Yash P Talwekar. "A gyroscope-free visual-inertial flight control and wind sensing system for 10-mg robots". In: *Science Robotics* 7.72 (2022), eabq8184.

[105] Brittney L Boublil, Clarice Anna Diebold, and Cynthia F Moss. "Mechanosensory hairs and hair-like structures in the animal kingdom: specializations and shared functions serve to inspire technology applications". In: *Sensors* 21.19 (2021), p. 6375.

[106] Jeffrey M Camhi. "Locust wind receptors: I. Transducer mechanics and sensory response". In: *Journal of Experimental Biology* 50.2 (1969), pp. 335–348.

[107] Tuo Wang, Teresa A. Kent, and Sarah Bergbreiter. "Design of Whisker-Inspired Sensors for Multi-Directional Hydrodynamic Sensing". 2023.

[108] N Nguyen Minh-Dung et al. "3D airflow velocity vector sensor". In: *2011 IEEE 24th International Conference on Micro Electro Mechanical Systems*. IEEE. 2011, pp. 513–516.

[109] Cheng Liu et al. “A directional anemometer based on MEMS differential pressure sensors”. In: *The 9th IEEE International Conference on Nano/Micro Engineered and Molecular Systems (NEMS)*. IEEE. 2014, pp. 517–520.

[110] Edward Arens et al. “Measuring 3D indoor air velocity via an inexpensive low-power ultrasonic anemometer”. In: *Energy and Buildings* 211 (2020), p. 109805.

[111] Massimo Piotto, G Pennelli, and P Bruschi. “Fabrication and characterization of a directional anemometer based on a single chip MEMS flow sensor”. In: *Microelectronic Engineering* 88.8 (2011), pp. 2214–2217.

[112] Paolo Bruschi, Michele Dei, and Massimo Piotto. “A low-power 2-D wind sensor based on integrated flow meters”. In: *IEEE Sensors Journal* 9.12 (2009), pp. 1688–1696.

[113] Jack A Defay, Jacob M Peters, and Kirstin H Petersen. “A customizable, low-cost alternative for distributed 2D flow sensing in swarms”. In: *Artificial Life and Robotics* 27.2 (2022), pp. 272–277.

[114] Yizhou Ye et al. “Octagon-shaped 2-D micromachined thermal wind sensor for high-accurate applications”. In: *Journal of Microelectromechanical Systems* 27.4 (2018), pp. 739–747.

[115] Shixuan Gao et al. “Configuration of a self-heated double Wheatstone bridge for 2-D wind sensors”. In: *Journal of Microelectromechanical Systems* 28.1 (2018), pp. 125–130.

[116] Jindou Jia et al. “Accurate high-maneuvering trajectory tracking for quadrotors: A drag utilization method”. In: *IEEE Robotics and Automation Letters* 7.3 (2022), pp. 6966–6973.

[117] Weidong Ding et al. “Adding optical flow into the GPS/INS integration for UAV navigation”. In: *Proc. of International Global Navigation Satellite Systems Society Symposium*. Citeseer. 2009, pp. 1–13.

[118] Haiyang Chao, Yu Gu, and Marcello Napolitano. "A survey of optical flow techniques for robotics navigation applications". In: *Journal of Intelligent & Robotic Systems* 73 (2014), pp. 361–372.

[119] Mohammad Fattahi Sani and Ghader Karimian. "Automatic navigation and landing of an indoor AR. drone quadrotor using ArUco marker and inertial sensors". In: *2017 international conference on computer and drone applications (IConDA)*. IEEE. 2017, pp. 102–107.

[120] Pierre-Jean Bristeau et al. "The navigation and control technology inside the ar. drone micro uav". In: *IFAC Proceedings Volumes* 44.1 (2011), pp. 1477–1484.

[121] Jakob Engel, Jürgen Sturm, and Daniel Cremers. "Accurate figure flying with a quadrocopter using onboard visual and inertial sensing". In: *Imu* 320.240 (2012).

[122] Cong Yang et al. "BladeView: Toward Automatic Wind Turbine Inspection With Unmanned Aerial Vehicle". In: *IEEE Transactions on Automation Science and Engineering* (2024).

[123] Pramod Abichandani et al. "Wind measurement and simulation techniques in multi-rotor small unmanned aerial vehicles". In: *IEEE Access* 8 (2020), pp. 54910–54927.

[124] Matthew Marino et al. "An evaluation of multi-rotor unmanned aircraft as flying wind sensors". In: *International Journal of Micro Air Vehicles* 7.3 (2015), pp. 285–299.

[125] Ze Wang, Jingang Qu, and Pascal Morin. "Deep Learning-based Flight Speed Estimation using Thermal Anemometers". In: *International Micro Air Vehicle Conference*. 2022.

[126] Nathaniel Simon et al. "FlowDrone: wind estimation and gust rejection on UAVs using fast-response hot-wire flow sensors". In: *2023 IEEE International Conference on Robotics and Automation (ICRA)*. IEEE. 2023, pp. 5393–5399.

[127] Hui-Min Chou, Meng-Ju Lin, and Rongshun Chen. "Fabrication and analysis of awl-shaped serpentine microsprings for large out-of-plane displacement". In: *Journal of Micromechanics and Microengineering* 25.9 (2015), p. 095018.

[128] Jérôme Casas, Thomas Steinmann, and Gijs Krijnen. "Why do insects have such a high density of flow-sensing hairs? Insights from the hydromechanics of biomimetic MEMS sensors". In: *Journal of the Royal Society interface* 7.51 (2010), pp. 1487–1495.

[129] David Crowe et al. "Two supervised machine learning approaches for wind velocity estimation using multi-rotor copter attitude measurements". In: *Sensors* 20.19 (2020), p. 5638.

[130] Michael O'Connell et al. "Neural-fly enables rapid learning for agile flight in strong winds". In: *Science Robotics* 7.66 (2022), eabm6597.

[131] Regan Kubicek et al. "A new sensation: Digital strain sensing for disturbance detection in flapping wing micro aerial vehicles". In: *2023 IEEE International Conference on Robotics and Automation (ICRA)*. IEEE. 2023, pp. 3390–3396.

[132] Michael A Lin et al. "Navigation and 3D Surface Reconstruction from Passive Whisker Sensing". In: *arXiv preprint arXiv:2406.06038* (2024).

[133] Chaoxiang Ye, Guido De Croon, and Salua Hamaza. "A Biomorphic Whisker Sensor for Aerial Tactile Applications". In: *2024 IEEE International Conference on Robotics and Automation (ICRA)*. IEEE. 2024, pp. 5257–5263.

[134] Prasanna Kumar Routray et al. "Novel Techniques for Separating Intrinsic and Extrinsic Responses of Whisker Sensors". In: *Authorea Preprints* (2024).